Star Formation in Low Mass Galaxies Across Cosmic Time: Connecting the Near and Far Fields

by

Tom Oriyan Zick

A dissertation submitted in partial satisfaction of the

requirements for the degree of

Doctor of Philosophy

in

Astrophysics

in the

Graduate Division

of the

University of California, Berkeley

Committee in charge:

Professor Daniel R. Weisz, Chair
Professor Mariska Kriek
Professor Martin White

Spring 2020

Star Formation in Low Mass Galaxies Across Cosmic Time: Connecting the Near and Far Fields

Abstract

Star Formation in Low Mass Galaxies Across Cosmic Time: Connecting the Near and Far Fields

by

Tom Oriyan Zick

Doctor of Philosophy in Astrophysics

University of California, Berkeley

Professor Daniel R. Weisz, Chair

Over the past decade, large photometric surveys, and more recently spectroscopic follow up, have elucidated a clearer picture of galaxy evolution since the epoch of peak star formation at z = 1-3. However, despite these advancements, low mass galaxies, which exhibit much higher number densities than their $LogM_{\star} > 9.5$M$\odot$ counterparts, have remained challenging to follow up observationally with current instruments given their faintness and sizes. Despite challenging systematics, gravitational lensing induced magnification and flux amplification is one path towards studying the faint high redshift Universe. Another complimentary approach lies in utilizing the stellar fossil record to turn back the clock on local resolved stars and place constraints on their progenitors. Advances in magnification maps and deep photometry from the Hubble Frontier Fields (HFF) survey, as well as improvement in stellar models and distance measurements, enable us to bridge between the near and far fields to study star formation in low mass galaxies across cosmic time.

In this dissertation, I use rest-frame optical spectroscopy from the MOSFIRE Deep Evolution Field (MOSDEF) survey to investigate the star formation histories (SFHs) of different galaxy types, ranging from actively star-forming to quiescent at $1.4 \leq z \leq 2.6$. SFHs are constrained using stellar continuum spectroscopy, specifically through a combination of Balmer absorption lines, the 4000 Å break, and the equivalent width of the Hα emission line. I use Spectral Energy Distribution (SED) modeling to constrain the average SFHs for five galaxy types including quiescent, green valley, and post-starburst galaxies (transitional galaxies). I find that quiescent and transitional galaxies in the MOSDEF sample are dominated by an SFH with an average star-formation timescale of $\tau \sim 0.1 - 0.2$ Gyr, in contrast to galaxies in the low-redshift Universe which form their stars over a more extended time period ($\tau > 1$ Gyr) on average. Finally, I compare the average properties of the galaxies in the transitional bins to investigate possible paths to quiescence, and speculate on the viability of a dusty post-starburst phase.

I then utilize the the stellar fossil record and stellar population synthesis modeling to reconstruct the evolution of rest-frame ultra-violet (UV) luminosities of the most massive Milky Way dwarf

spheroidal satellite galaxy, Fornax, and its five globular clusters (GCs) across redshift. I find that (1) Fornax's (proto-)GCs can generate $10-100$ times more UV flux than the field population, despite comprising $<\sim 5\%$ of the stellar mass at the relevant redshifts; (2) due to their respective surface brightnesses, it is more likely that faint, compact sources in the HFF are GCs hosted by faint galaxies, than faint galaxies themselves. This may significantly complicate the construction of a galaxy UV luminosity function at $z > 3$. (3) GC formation can introduce order-of-magnitude errors in abundance matching. I also find that some compact HFF objects are consistent with the reconstructed properties of Fornax's GCs at the same redshifts (e.g., surface brightness, star formation rate), suggesting we may already have detected proto-GCs in the early Universe.

Finally, I present results from a Keck/MOSFIRE survey of 39 low mass galaxies in the HFF. I first discuss the sub-structure around the progenitor of a Milky Way-mass galaxy in the Hubble Frontier Fields (HFF). Specifically, I study an $r_e = 40^{+70}_{-30}$pc, $M_\star \sim 10^{8.2} M_\odot$ rest-frame UV luminous "clump" at a projected distance of ~100 pc from a $M_\star \sim 10^{9.8}\mathrm{M}_\odot$ galaxy at $z = 2.36$ with a magnification $\mu = 5.21$. I measure the star formation history of the clump and galaxy by jointly modeling the broadband SED from HFF photometry and Hα from MOSFIRE spectroscopy, and explore methodology to constrain whether it formed $in-situ$ or presents a $1:40$ stellar mass ratio accretion event.

I then explore the recent star formation histories and kinematics of the rest of the sample which consists of: $7 \leq \log M_\star/M_\odot \leq 10.2$ moderately gravitationally lensed ($\mu < 20$), star-forming galaxies at $1.8 \leq z \leq 3.2$. I find that $L_{H\alpha}$ star formation rates (SFRs) exceed UV SFRs by factors of $\sim 3-10$, indicative of highly bursty star formation. Galaxy size (r_e) is a strong function of decreasing $\mathrm{SFR}_{\mathrm{H}\alpha}/\mathrm{SFR}_{UV}$ and $\Sigma_{SFR,\,H\alpha}$ (but not $\Sigma_{SFR,\,UV}$). This suggests that r_e is likely set by the ratio of instantaneous (< 10Myr) to recent star (< 100Myr) formation in these low-mass galaxies. I compare integrated velocity dispersions (σ) with specific SFRs and find a strong correlation at fixed stellar mass. This is consistent with scenarios in which stellar feedback is driving changes to the potential of low-mass galaxies. Finally, I compare the dynamical masses of my galaxy sample with their inferred total baryonic masses using the Kennicutt-Schmidt (KS) relation and find that my inferred baryonic mass is un-physical, even when size underestimates are considered, suggesting that the galaxies in my sample are gas poor compared to local ones.

To my mother, Natti Zick, who has always encouraged my curiosity and inspired me to wonder.

Contents

List of Figures

List of Tables

Acknowledgments

I would like to thank my thesis advisor Dan Weisz. Without his mentorship, patience, and encouragement, this dissertation would not have been possible. Dan has generously provided me with the resources to thrive throughout my graduate career, sending me to interesting conferences, setting me up with new collaborators, and always leaving his door open to me. I have truly benefited and grown as a researcher through our collaboration.

The work included in this dissertation relied upon instruments, surveys, and analysis pipelines that required years of effort to develop. I would like to acknowledge the observing team at Keck Observatory and the MOSFIRE instrument team, for making my observing runs throughout graduate school so seamless. I would further like to thank Mariska Kriek for use of her MOSFIRE reduction pipeline and for her guidance in proposal writing and observation planning. I am also grateful to Ben Johnson and Joel Leja for their development of and support in using `PROSPECTOR`. Finally, the work in this dissertation would not have been possible without the HFF DeepSpace team and the public catalogs they curate.

The graduate student community at Berkeley made my time in the program rewarding, intellectually stimulating, and fun. I would like to thank Sedona Price for her mentorship throughout my graduate career, from answering my silly bash scripting questions, to jumping on zoom at 10pm her time to talk through interesting plots with me. I would also like to thank Lauren Weisz and Lea Hirsch for acting as my live-in orientation committee and making it so I never felt like a confused, helpless, first-year grad, Casey Lam, for giving me the chance to partially return the favor, and finally Ben Horowitz and Abi Polin for helping me push through the final years of grad school. My time in Berkeley would not have been the same without office-mates like Wren Suess, Jennifer Barnes, Katherine de Kleer and the rest of the 'cube-zone' (past and present), who made Campbell hall an exciting place to do science, where random totoros spontaneously appeared. Also brightening my time in Campbell was Nina Ruynmaker who processed countless reimbursements for me and, throughout it all, handled my complete ineptitude at form filling with unparalleled graciousness.

Finally, I would like to thank my mother whose advice and support got me through graduate school, especially once she stopped asking me to drop out and go travel with her instead.

Chapter 1

Introduction

1.1 Star formation across cosmic time

Understanding how galaxies grow and evolve is a key open question in Astronomy which demands self consistent results across billions of years of cosmic time. In principle, any prescription that applies to galaxies forming 3.8 billion years after the Big Bang, should be able to explain 10 billion year old stellar populations we observe in the local volume, and vice versa.

On large scales ($\geq$ 1 Mpc), the Λ cold dark matter (ΛCDM) paradigm has been immensely successful at bridging across cosmic time. It has provided a framework capable of connecting order 10^{-4} baryon density perturbations measured from the Cosmic Microwave Background (CMB), to the large scale structure observed in the local Universe (Peebles 1980; Davis & Peebles 1983; Planck Collaboration et al. 2016; Guo et al. 2016a). In this hierarchical structure formation model, early density perturbations collapse into dark matter halos, which then merge and accrete across cosmic time to form structure on increasingly larger scales, from galaxies, to galaxy groups and clusters (Springel et al. 2005; Boylan-Kolchin et al. 2009, e.g.,). ΛCDM based galaxy simulations and models are increasingly predicting galaxy properties such as number counts, clustering, and even to some extent colors and morphologies, that agree with our observational picture (Behroozi et al. 2013; Vogelsberger et al. 2014; Schaye et al. 2015).

However on small scales, there begin to be issues with basic ΛCDM (see Bullock & Boylan-Kolchin 2017, and references therein). The overprediction of low mass satellite galaxies (in the local volume) (Kuhlen et al. 2009; Garrison-Kimmel et al. 2014, e.g.,), dubbed the “missing satellites" problem, persists despite ever lower surface brightness surveys (Drlica-Wagner et al. 2015). The cores of dark matter dominated galaxies galaxies are less ‘cuspy” and denser than they ought to be (Walker & Peñarrubia 2011; Navarro et al. 2010). Meanwhile the most massive satellite halos predicted by ΛCDM are *too* dense to host even the most massive milky way satellites (Boylan-Kolchin et al. 2011, 2012). The most promising theoretical avenues towards resolving this small scale tensions lay in incorporation of baryonic feedback (Madau et al. 2014; Oñorbe et al. 2015b; El-Badry et al. 2016; Wetzel et al. 2016; Garrison-Kimmel et al. 2017), yet the mass scales and redshifts involved makes direct observational constraints challenging to obtain.

Furthermore, despite a handful of scaling relations that are remarkably durable across redshift (e.g., Tully & Fisher 1977; Bezanson et al. 2013; Daddi et al. 2007; Whitaker et al. 2012), galaxies exhibit an immense diversity that eludes simple characterization. Baryonic processes such as star formation, supernovae driven stellar feedback, chemical enrichment and active galactic nuclei (AGN), are related to dark matter halo growth in a non-trivial, complex manner that has yet to be fully elucidated. For example, galaxy quenching, the process by which galaxies cease their star formation and become quiescent, can be related to environment, mass, and morphology, but is not uniquely described by either (e.g., Kauffmann et al. 2004; Baldry et al. 2006). In many cases, these parameters do not even correlate with each other, highlighting the challenging nature of disentangling baryonic physics and gravity in the context of galaxy evolution.

1.2 Observing the Peak of Cosmic Star Formation

An ideal cosmic laboratory for theories of galaxy evolution is the period of cosmic history dubbed 'cosmic high noon'. Spanning $z = 1 - 3$, this epoch represents the peak of average cosmic SFR density (Madau & Dickinson 2014) and black hole accretion (Hopkins & Beacom 2006) across cosmic time. Over the past decade, a concerted effort by the high redshift community towards characterizing star formation, ISM properties, and galaxy morphology in the high redshift Universe has greatly expanded our picture beyond the local volume. Photometric surveys such as NMBS (Whitaker et al. 2011), CANDELS (Grogin et al. 2011; Koekemoer et al. 2011) and 3D-HST (van Dokkum et al. 2011; Brammer et al. 2012) brought into focus a statistical picture of galaxy evolution over cosmic times. For example, these studies revealed: a bimodal color distribution of galaxies (Kriek et al. 2008; Williams et al. 2009), with a red (quiescent) sequence already set at $z = 2.5$ (Whitaker et al. 2011, 2012); a tight, nearly linear, relation between star formation and mass spanning 12.5 billion years of cosmic time (Daddi et al. 2007; Whitaker et al. 2012; Speagle et al. 2014); as well as a mass-size relation in which galaxies at fixed mass were more compact in early times (van der Wel et al. 2014).

Upon these large photometric samples, spectroscopic follow up enabled a still more granular picture of galaxy evolution to emerge. Spectroscopic surveys like MOSDEF (Kriek et al. 2015) KMOS-3D (Wisnioski et al. 2015, VLT), and KROSS (Stott et al. 2016) have collectively amassed moderate resolution spectra of over 3000 galaxies. Together, these have enabled direct measurements of metalicities and ionization parameters (Sanders et al. 2016; Wuyts et al. 2016; Sanders et al. 2020), calibration of star formation rate indicators (Shivaei et al. 2015; Shivaei et al. 2017), measurement of dust attenuation (Reddy et al. 2015), baryon fraction and kinematics (Price et al. 2015; Wuyts et al. 2016). Despite these impressive strides, low mass galaxies, which are far more ubiqioutous, are generally too faint and elude statistical consideration at $z > 1$.

Gravitational lensing represents the clearest path towards pushing these results to lower masses and fainter galxies. The Hubble Frontier Fields (HFF) survey (Lotz et al. 2017), which leverages magnification of background sources due to massive galaxy clusters in the foreground, to study galaxies well beyond the detection limit of the Hubble Ultra Deep Field, may enable the study of high-redshift star formation at comparable scales to local observations (Cava et al. 2018). The

majority of work utilizing the HFF has harnessed it to study the faint end of the UV luminosity function and in the process uncovered extremely compact ($r_e < 100pc$) sources (Kawamata et al. 2017; Bouwens et al. 2017b). Further size comparison of faint ($M_{\rm UV}$~-15) using sources in low vs. high shear lensed regions to account for surface brightness limits, has shown them to be substantially more compact than their brighter counterparts, with Re<240-160pc for z ~2-8 (Bouwens et al. 2017a).

Despite these intriguing results, the true nature of objects in the faint, low mass region of parameter space remains unclear. Whether these objects are ancestors of Local Group-like dwarf galaxies (Weisz et al. 2014; Boylan-Kolchin et al. 2015; Finlator et al. 2017), bright star-forming regions of more spatially extended faint galaxies (Ma et al. 2017), super star clusters (Vanzella et al. 2017), or proto-globular clusters caught in the act of formation (Kim et al. 2017; Vanzella et al. 2016) is not yet known, as theoretical investigations are in very early stages and follow up observations are lacking. High resolution cosmological zoom-in simulations from the Feedback In Realistic Environments (FIRE) project, which have effectively reproduced L_* (Hopkins et al. 2014), quiescent (Feldmann et al. 2016), and dwarf galaxy properties (Wetzel et al. 2016) at various redshifts, have begun to examine the nature of faint compact sources at higher redshifts (El-Badry et al. 2016; Kim et al. 2017; Ma et al. 2017), but have little data for comparison.

1.3 Galactic Archaeology

An alternative path towards studying faint low mass galaxies in the early Universe is to utilize their descendants. Precision color magnitude modeling (Dolphin 2002; de Boer et al. 2012c) provides a time resolved star formation history for a given resolved stellar population. Local group galaxies can then be used to turn back the clock on their star formation histories and constrain their high redshift progenitors (Freeman & Bland-Hawthorn 2002; Ricotti 2002; Madau et al. 2008; Brown et al. 2012)

Galactic archaeology has recently yielded important constraints on the turnover of the UV Luminosity functions during the epoch of reionization (Weisz et al. 2014; Boylan-Kolchin et al. 2015; Weisz & Boylan-Kolchin 2017). Yet direct comparisons to high redshift observations remain challenging. For example, metal-poor globular clusters in the Milky Way can be approximated as simple stellar populations and are fairly straightforward to age-date using CMD modeling (de Boer et al. 2012a). Yet, though they are 12 Gyr old on average, the typical uncertainties associated with their age are on the order of a Gyr (McConnachie 2012), which can place their formation anywhere between $z = 2.5 - 7$. These uncertainties are usually dominated by varying distance estimates (Choi et al. 2018), yet there remain additional systematic uncertainties that arise from accuracy in stellar modeling (e.g., VandenBerg et al. 2013; Chaboyer et al. 2017; Tayar et al. 2017).

The GAIA survey, which has measured galactic paralax based distances for billions of stars (Lindegren et al. 2016a) out to 2 kpc, promises precision distance, and therefore age measurements for an increasing fraction of resolved stars. These observational advancements, combined with more robust stellar modeling (Choi et al. 2016), positions us to not only better connect near and far

field observations, but also to use local observations to guide our interpretation of the high redshift Universe.

1.4 Connecting the Near and Far Fields

The aim of galaxy evolution is to connect galaxy formation across cosmic time, with local volume observations as a natural end point. In this dissertation, I capitalize on the self consistent nature of galaxy formation to not only bridge between near and far field observations, but to harness the former to interpret the latter. I leverage the gains in precision age-dating of resolved stars, the wealth of $z = 2 - 3$ spectroscopy, as well as the flux amplification and magnification of the HFF, to constrain star formation in low mass galaxies across cosmic time. This dissertation is organized as follows:

Using the MOSDEF rest-frame optical spectroscopic survey, I investigate the star-formation histories (SFHs) of different galaxy types, ranging from actively star forming to quiescent at $1.4 \leq z \leq 2.6$. Absorption and continuum features encode information about star formation histories (SFH) that is robust to the age-metallicity degeneracies that typically plague photometric studies, yet can typically only be studied in the most massive quiescent galaxies at $z \sim 2$. In this chapter I outline a technique that combines spectroscopy and photometry to measure robust SFHs for a representative sample, spanning star forming to quiescent galaxies. I use this to constrain galaxy formation scenarios and evolutionary paths towards quenching.

In chapter 3 I look to resolved stellar populations to inform observations of still lower mass galaxies at high redshift. I use CMD modeling derived star formation histories along with stellar population synthesis modeling to reconstruct the evolution of rest frame ultra-violet (UV) luminosities of the most massive Milky Way satellite galaxy, Fornax, and its five globular clusters (GCs). With these mock observations, I explore observational signatures of GC formation as well as potential systematics in current measurements of the faint end of the UV Luminosity function at $z > 2$.

In chapter 4 and chapter 5 I present a rest-frame optical spectroscopic survey of 38 low mass galaxies in the HFF, motivated by the mock observations in the previous chapter. I introduce techniques to incorporate spectroscopy to improve upon SED fitting using a non-parametric star formation history and explore how this methodology could be used to study hierarchical star formation in real time in chapter 4. In chapter 5, I compare UV and and Hα star formation rates to gauge the recent star formation histories of low mass galaxies at $z = 2$ and combine this with measurements of integrated velocity dispersion to constrain stellar feedback. Additionally, I comment on the half light radii of these sources and explore potential systematics in faint HFF observations.

Finally, in chapter 6 I summarize the results in this dissertation and enumerate their implications for observations in the era of the James Webb Space Telescope.

Chapter 2

Stellar Continuum Spectra and Star Formation Histories of Active, Transitional, and Quiescent Galaxies at $1.4 < z < 2.6$

2.1 Introduction

A bimodal distribution of galaxy properties (e.g., color, age, morphology) has been observed both in the local universe (e.g., Kauffmann et al. 2003) and up to high redshift (e.g., Williams et al. 2009; Whitaker et al. 2011), defining a red quiescent sequence and a star-forming sequence in color-mass or color-color space. Though a red sequence has been observed out to $z = 3$, the relative abundances of quiescent and star-forming galaxies changes across cosmic time; at low redshifts higher mass galaxies are predominantly quiescent, whereas at $z \geq 2.5$ star-forming galaxies dominate at all masses (e.g., Muzzin et al. 2013; Tomczak et al. 2014). However, the process by which these star-forming galaxies quench and join the quiescent sequence remains poorly understood.

Understanding the evolution of galaxies from star forming to quiescent requires detailed knowledge of star-formation histories (SFHs) for a large, representative population of galaxies. While these measurements are readily available at $z \leq 0.1$ (Kauffmann et al. 2003) and have recently been extended to $z \sim 0.8$ (Wu et al. 2018), the vast majority of quiescent galaxies quench at $z > 1$ (e.g., Muzzin et al. 2013). Therefore, understanding quenching requires pushing studies to even higher redshifts.

Past work around this peak quenching epoch has relied heavily on deep multi-wavelength photometry, which yields poor constraints on SFHs due to model degeneracy, lack of spectroscopic detail, and imprecise redshifts. More robust SFHs can be obtained from the stellar continuum by comparing features sensitive to recent star formation, like the Balmer absorption-line index, $H\delta_A$, with features sensitive to age, like the 4000 Å break (D_n4000). Such measurements require high S/N spectroscopy which has in the past only been attained for the brightest, most massive high-redshift sources (e.g., Kriek et al. 2009, 2016; van de Sande et al. 2013; Belli et al. 2015; Barro et al. 2016). Alternatively one can stack multiple like galaxies to reach a S/N sufficient to

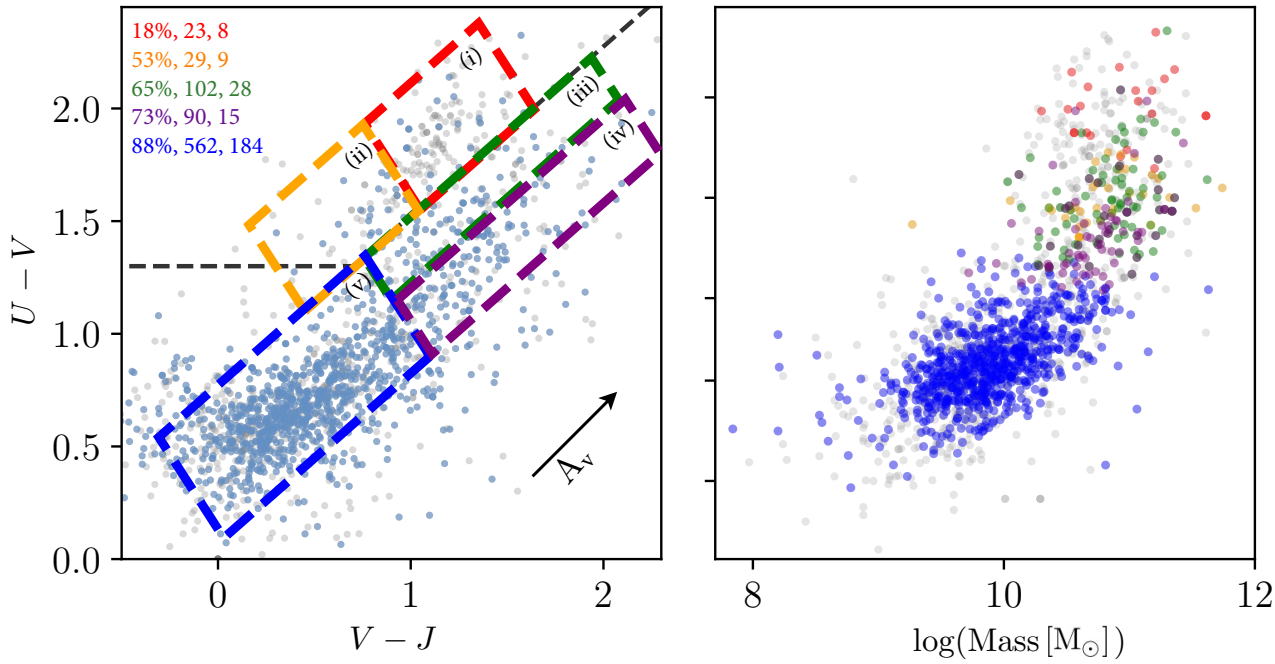

Figure 2.1: Left: The full MOSDEF sample (grey) and our selected sample (blue) in *UVJ* space, where each box color corresponds to a distinct typical SED shape. On the top left we detail the percent of targets with MOSDEF redshift measurements, the number of spectra with a MOSDEF redshift, and the average number of galaxies per pixel in our composite spectra, colored by corresponding bin. Right: $U - V$ color vs. stellar mass for galaxies (colored by bin) that comprise each stack.

characterize absorption features (Onodera et al. 2012; Mendel et al. 2015), however such studies have also been conducted primarily for massive quiescent galaxies.

With the recently completed MOSFIRE Deep Evolution Field (MOSDEF) survey (Kriek et al. 2015), in which MOSFIRE spectroscopy was collected for $\sim$ 1500 galaxies at $1.37 \leq z \leq 3.80$, it is now possible to spectroscopically probe the SFHs of a representative high-redshift galaxy population for the first time. In this Letter we present a technique for constructing composite spectra that conserves stellar continuum, enabling us to measure absorption features sensitive to age and short-term variation in star formation at $z \sim 2$. With this methodology, we characterize SFHs for stacks of galaxies across rest-frame $U - V$ vs. $V - J$ color-color space.

Throughout this work we utilize a Chabrier (2003) initial mass function and a ΛCDM cosmology with $\Omega_M = 0.3$, $\Omega_\Lambda = 0.7$ and $H_0 = 70\,\mathrm{kms^{-1}Mpc^{-1}}$.

2.2 Data and Galaxy Sample

This work leverages the full MOSDEF sample, consisting of rest-frame optical (flux-calibrated) spectra for 1493 H-band selected galaxies between $1.37 \leq z \leq 3.80$, with masses and star formation rates (SFRs) ranging from $\sim 10^9 - 10^{11.5}$ $M_\odot$ and $\sim 10^0 - 10^3$ $M_\odot$ yr^{-1}, respectively. All MOSDEF galaxies are covered by deep *Hubble Space Telescope*/WFC3 imaging from CANDELS (Koekemoer et al. 2011; Grogin et al. 2011). For information about target selection, data reduction, and sample parameters see Kriek et al. (2015). For the current work we have selected galaxies with a MOSDEF redshift $1.37 \leq z \leq 2.61$, as higher redshift galaxies do not typically have sufficient S/N for stacking continuum spectra. We also require at least 400 pixels of coverage within the 3700 Å$\leq \lambda \leq$6600 Åbandpass, which ensures the validity of our stacking method.

For all 806 spectra in our sample we have measured stellar masses and rest-frame colors using the photometric catalogs constructed by the 3D-HST collaboration (Skelton et al. 2014; Momcheva et al. 2016) in conjunction with MOSDEF redshifts. Masses are obtained by fitting a galaxy's spectral energy distribution (SED) with stellar population synthesis (SPS) models, utilizing the SPS fitting code `FAST` (Kriek et al. 2009) along with flexible SPS models (FSPS) (Conroy et al. 2009a), and the Calzetti et al. (2000) attenuation curve. We derive rest-frame colors using `EAzY` (Brammer et al. 2008) and adopt sizes as measured by van der Wel et al. (2012, 2014) from the CANDELS/F160W photometric band using `GalFit` and `Galapagos` (Peng et al. 2002; Barden et al. 2012). We use the circularized r_e from these size measurements to derive the mass surface density (Σ) for each of our galaxies.

2.3 Stacking MOSDEF Spectra

In this work we bin galaxies by similarity in spectral type as determined by their rest-frame $U - V$ vs. $V - J$ colors to attain sufficient S/N per stack to measure SFHs. In the UVJ diagram, dust extinction (A_v) increases linearly with increasing $U - V$ and $V - J$, while specific star formation (sSFR) decreases in an almost perpendicular direction for star-forming galaxies. Once a galaxy has stopped forming stars, it will move along the red sequence as it ages (e.g., Wuyts et al. 2009; Whitaker et al. 2012; Fumagalli et al. 2014; Yano et al. 2016). Though galaxies on the quiescent sequence can also be reddened due to increased metallicity, this effect is sub dominant to age (Whitaker et al. 2013). We take advantage of these trends in sSFR, age, and dust to bin galaxies as shown in panel (a) of Figure 2.1. We use the age gradient in the red sequence to separate our post-starburst (ii) from our quiescent bin (i), and split our star-forming sequence into non-dusty star-forming (v), dusty star-forming (iv) and dusty galaxies with lower sSFRs (iii). We show the bin break down of our selected galaxies in color-mass space in Figure 2.1.

For each bin in UVJ space we generate a composite spectrum from individual spectra with varying wavelength coverage. First, we calculate the average best-fit SPS model in luminosity density units for each UVJ bin by averaging the best-fit SPS model per member galaxy.

Next, for each individual spectrum, we create a skyline mask ($m_{i,x}$) using a S/N cutoff and interpolate the reduced rest-frame spectrum and mask onto a 0.5 Å separated grid to approximate

the spectral sampling of MOSFIRE. We derive a scaling parameter (s_x) for each individual spectrum using the average best-fit model corresponding to its *UVJ* bin according to:

$$s_x = \frac{\sum_{i=0}^{P} \omega_{i,x} r_{i,x} m_{i,x}}{\sum_{i=0}^{P} \omega_{i,x} f_{i,x}, m_{i,x}} \tag{2.1}$$

where P is the total number of pixels in the spectrum, $f_{i,x}$ is the flux of the ith pixel of a given spectrum x, $\omega_{i,x}$ is its corresponding inverse variance, $r_{i,x}$ is the corresponding luminosity density of the average best-fit SPS model for each bin.

Finally, we stack each spectrum in a given *UVJ* bin according to a S/N weighted mean stacking method described by:

$$t_i = \frac{\sum_{x=0}^{N} w_x s_x f_{i,x} m_{i,x}}{\sum_{x=0}^{N} w_x m_{i,x}} \tag{2.2}$$

where t_i is the final stacked value at each pixel and w_x is the average S/N per spectrum.

By scaling spectra to the average best-fit model for their bin, we correct for flux variations due to redshift differences in our sample and mitigate relative calibration issues between bands for a given galaxy.

In Figure 2.2, we show the resulting composite spectrum and SED for each bin in *UVJ* space arranged by increasing UV emission relative to the flux at rest-frame 5000 Å. In Figure 2.3 we zoom in on the region around Hα and Hδ for each of the stacks.

2.4 Measuring Spectral Features

To measure spectral features for each type, we first mask emission lines from the stacked spectra, then fit them using `FAST` with high-resolution Bruzual & Charlot (2003) models. In order to determine the Hα emission equivalent width (EW(Hα)), we fit with a triple Gaussian to account for potential contamination by the neighboring [N *ii*] lines, while correcting for underlying stellar absorption using the best-fit SPS model to the spectrum. We do not apply an additional dust correction to the EW(Hα) measurements to account for the possibility of increased extinction towards HII regions, thus they may be underestimated. We remove active galactic nuclei from our sample for measurements of Hα (see Azadi et al. 2017). Next, we simultaneously fit the other Balmer lines in the raw stacks for absorption and emission, fixing the latter to our measured Hα linewidths. As can be seen in panel (v) of Figure 2.2, the emission line widths are considerably narrower than the (pressure broadened) underlying Balmer absorption lines. Given these differing linewidths, we can robustly disentangle the emission from the absorption lines. Finally, we use our emission line fit to subtract the emission lines from the spectrum and re-fit our stacks to measure best-fit star formation timescales.

We measure continuum features from the emission-line subtracted stacked spectra, adopting the bandpasses for H$\delta_{\rm A}$ and D_n4000 described in Worthey & Ottaviani (1997) and Balogh et al. (1999), respectively (see Table 2.1). The one exception is the post-starburst stack (ii), where the

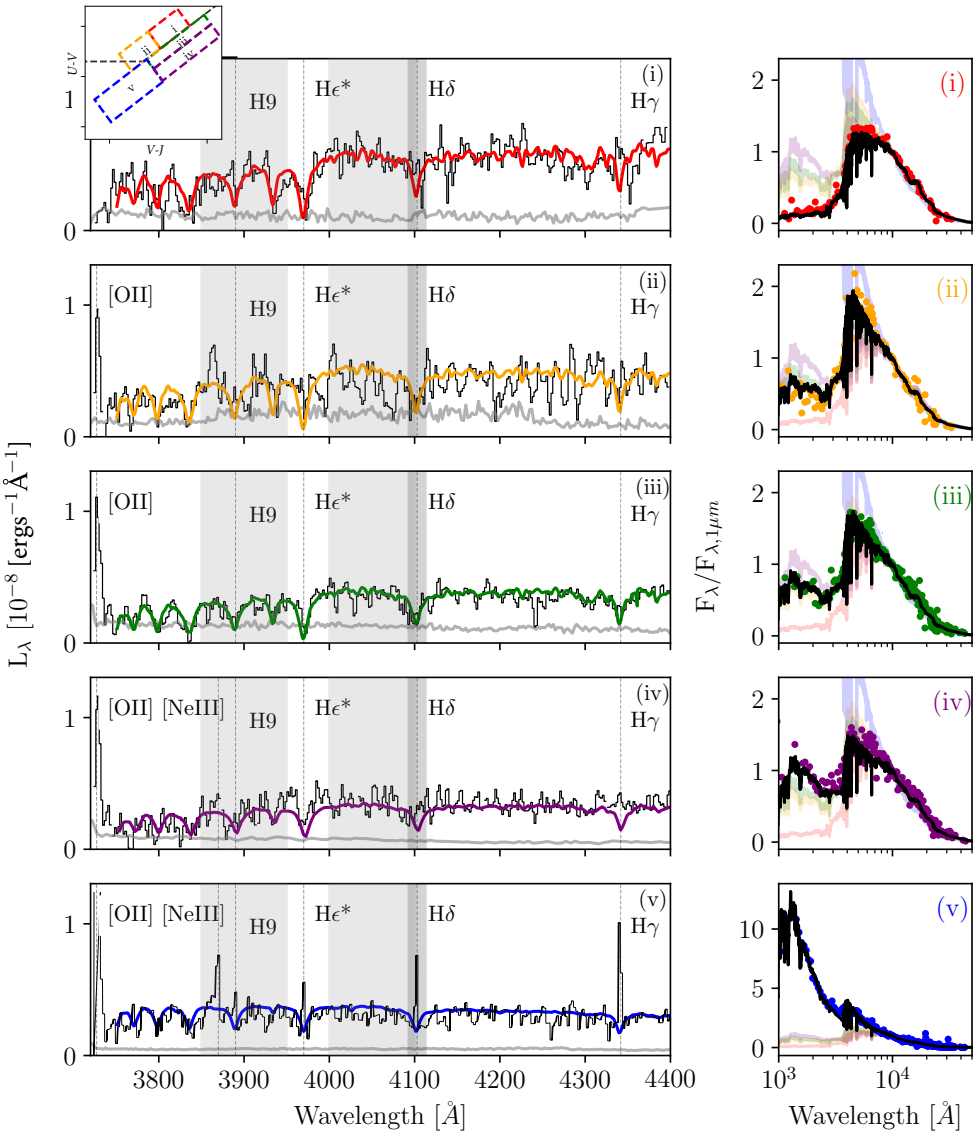

Figure 2.2: Left: Stacked spectra for galaxies binned in *UVJ* space and ordered by rest-frame UV emission relative to 1 μm. Each stack (black) and composite noise spectrum (grey) is shown median binned by 2.5 Å. The colored lines are the FAST fits to the stacked spectra. The bandpasses from which we measure D_n4000 and $H\delta_A$ are shown in grey and dark grey respectively. Right: Composite SEDs for each *UVJ* bin. The colored circles correspond to binned photometric measurements, the black line shows the best fit to the composite SED, while the best fits for the other bins are plotted according to their respective bin color.

blue continuum bandpass does not consist of sufficient galaxies to reliably measure $H\delta_A$ and we instead measure continuum from the best-fit SPS model to the spectrum.

Bin	Log τ [yr]	Hδ_A [Å]	D_n4000	EW(Hα) [Å]
i	8.2	4.9 ± 1.1	1.44 ± 0.05	1 ± 15
ii	8.4	6.2 ± 3.0	1.35 ± 0.1	8 ± 25
iii	8.2	8.4 ± 0.4	1.29 ± 0.09	33 ± 15
iv	9.3	6.3 ± 0.2	1.24 ± 0.09	56 ± 10
v	9.5	7.5 ± 1.3	1.14 ± 0.04	186 ± 19

Table 2.1: Spectral index measurements for each of our stacks along with the best-fit τ from our FAST fit (SFH of the form: SFR(t) $\propto te^{-t/\tau}$). Each bin number corresponds to UVJ box as shown in Figure 2.1.

We derive measurement errors by randomly generating a spectrum, drawing from the noise spectrum of each stack, and repeating our measurements 10000 times. We take the standard deviation of these measurements as our error. We also test for the sensitivity of each bin to its components by repeating our continuum measurements for stacks with a random $\sim$ 10% of each bin removed. Our measurement errors exceed the resulting variation for all but the quiescent stack, which is dominated by two especially massive galaxies. We therefore adopt the standard deviation of the bootstrapped ensemble for the quiescent bin measurements.

2.5 SFH of z $\sim$ 2 Galaxies across UVJ Space

We use the spectral features measured in the previous section to infer SFHs for a diverse galaxy population and provide unique insights into galaxy evolution at $z \sim 2$. In both Figures 2.2 and 2.3 we see clear trends in spectroscopic properties with increasing UV emission relative to rest-frame optical. To asses these trends, we compare Hδ_A, D_n4000, and EW(Hα) measured from our stacks in Figure 2.4. In panel (a) we compare Hδ_A with D_n4000. The former peaks when A-type stars dominate the spectrum, which only occurs when a relatively short star-formation period is followed by rapid quenching. The latter is sensitive to the opacity of stellar atmospheres and increases with age and metallicity. Comparing the two parameters allows us to assess the evolutionary phase and star-formation time scale of a given galaxy (Kauffmann et al. 2003).

Panel (b) compares Hδ_A to EW(Hα), another SFH probe that measures the relative importance of Hα emission to the underlying stellar continuum. As continuum emission is a proxy for mass and Hα arises from recombination around hot and massive O and early B type stars with short lifetimes, EW(Hα) relates star formation within the past 50 Myr to past star formation.

We find that our measurements for the transitional (ii and iii) and quiescent (i) bins form a sequence in both Hδ_A/D_n4000 space and EW(Hα)/Hδ_A space. These bins are most consistent with a rapid star formation model (τ = 0.1 − 0.2 Gyr) shown in panels (a) and (b) of Figure 2.4 and are therefore most compatible with a fast-quenching SFH. We find consistent results from

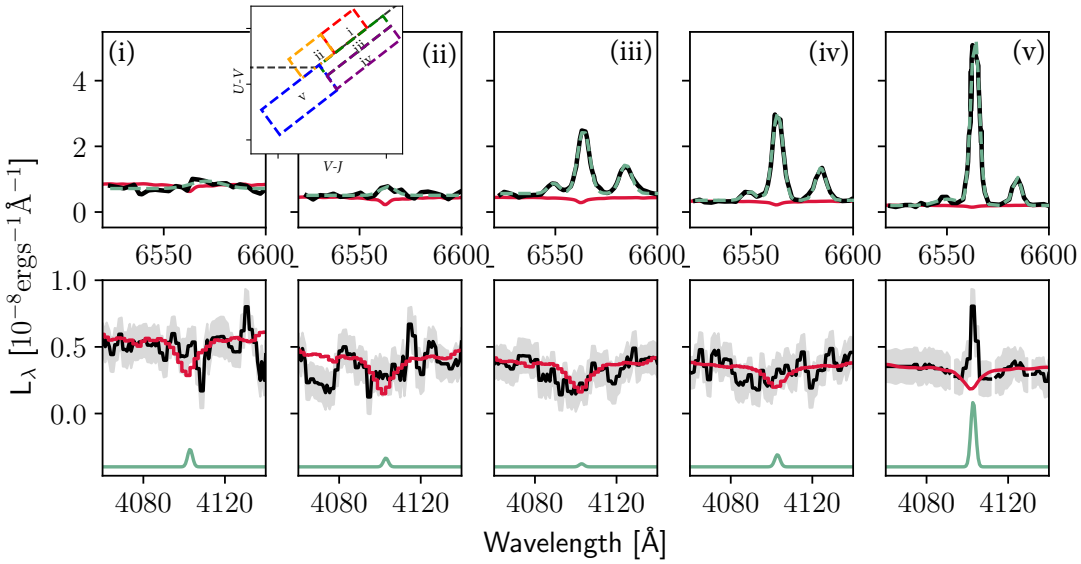

Figure 2.3: Top: The Hα region for each stacked spectrum (black). The triple Gaussian fit for the spectra is shown in the dashed teal lines, the best fit FAST model is shown in red. Bottom: Zoom in of the Hδ_A region, with the best fit for the absorption shown in red and the best fit for the emission (fixed to the Hα width), shown in teal. The noise spectrum is also plotted (grey). The emission Hδ in (i) is most likely due to AGN activity, as we only remove AGN from our EW(Hα) measurements.

our best-fit SPS models (see Table 2.1). Additionally, one of our contributing quiescent galaxies has an independent measurement of $\tau \sim 200$ Myr from [α/Fe] (Kriek et al. 2016) supporting our measurement. The average SFHs of the galaxies in the dusty (iv) and less-obscured (v) star-forming bins are consistent with a more extended star-formation timescale (i.e., delayed τ model with $\tau \approx 0.2 - 1$ Gyr). This result supports past work finding constant or rising SFHs for star-forming galaxies at $z = 2$ (e.g. Maraston et al. 2010; Lee et al. 2010; Reddy et al. 2012b)
We compare our measurements to values from the MPA/JHU SDSS catalogs (Kauffmann et al. 2003; Brinchmann et al. 2004) and find an offset between our transitional and quiescent galaxy bins relative to the median sequence at low redshifts. The inferred star-formation timescales in these bins are shorter than for a typical SDSS galaxy ($\tau \geq 1$ Gyr) at the 4σ level, for all but bin (ii), which is significant to 2σ. This offset is expected, as galaxies in the $z \sim 0.1$ universe had a longer period over which stars could have been formed. Nonetheless, the timescales of the transitional galaxies at $z \sim 2$ are substantially shorter than the age of the universe at that time. The Lega-C survey also finds an offset at $z = 0.8$ for D_n4000 vs. Hδ_A measured from individual spectra (Wu et al. 2018). However, as shown in Figure 2.4, it is less pronounced than for our stacks, implying shorter star-formation timescales with increasing redshift.

Past work has shown that quiescent galaxies have a higher mass surface density (Σ) than star-forming ones (e.g., Barro et al. 2014; van Dokkum et al. 2015). Mass has also been found to

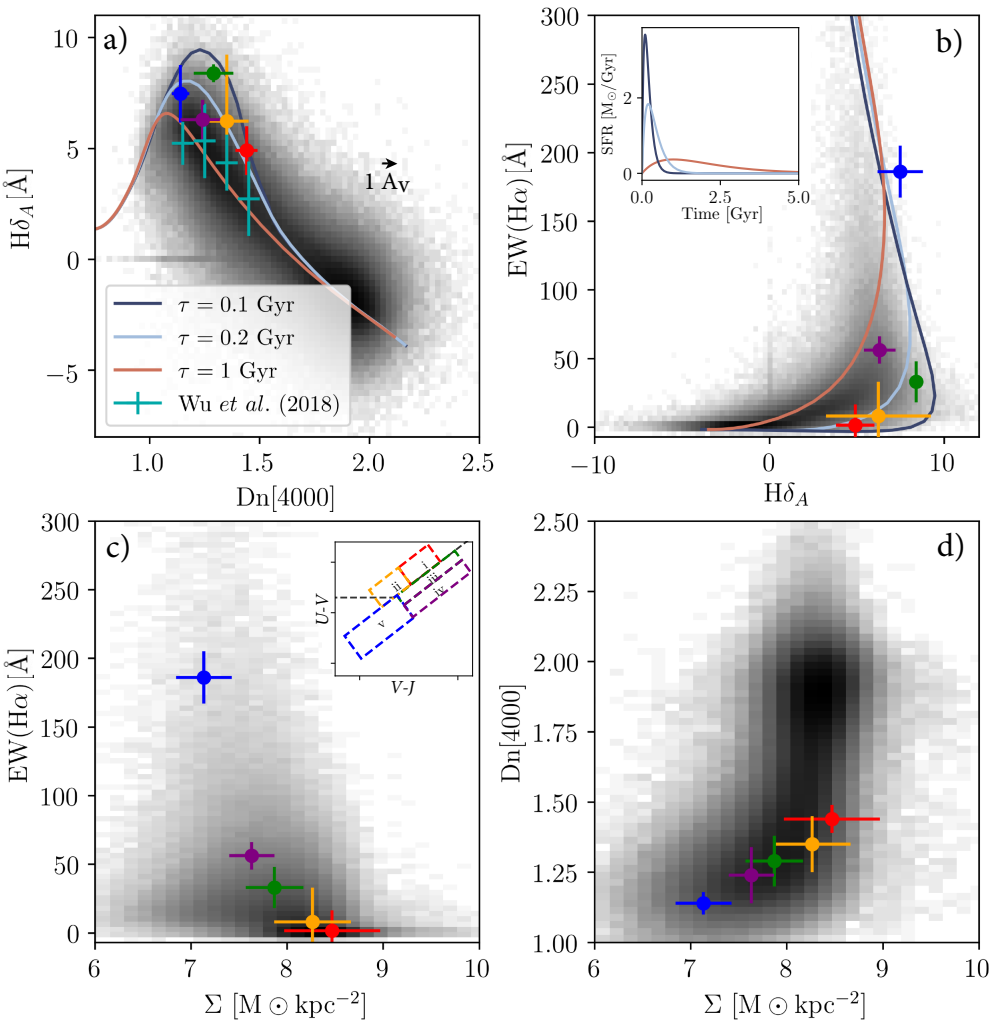

Figure 2.4: Hδ_A, D$_n$4000, EW(Hα), and Σ measurements for our stacks at $z \sim 2$ colored by their respective *UVJ* bin, compared to low-redshift values from SDSS, shown in greyscale. Where applicable, we overplot the FSPS model tracks for three delayed exponential SFHs with τ = 0.1, 0.2, 1.0 Gyr. Panel a: Hδ_A vs. D$_n$4000, finding higher Hδ_A than at low redshift for fixed values of D$_n$4000. We also show the $z = 0.8$ Wu et al. (2018) distribution where the error bars in D$_n$4000 and H$\delta_A$correspond to bin size and standard deviation of the distribution, respectively. As our D$_n$4000 measurements are not corrected for reddening, we illustrate the effect of 1 A_V of extinction with an arrow. Panel b: EW(Hα) vs. Hδ_A measurements confirming that the star formation timescales of transitional galaxies are most consistent with a short $\tau = 100 - 200$ Myr SFHs. Panels c-d: EW(Hα) and D$_n$4000 vs. Σ, illustrating a sequence in decreasing EW(Hα) and increasing D$_n$4000 as a function of Σ. Error bars in Σ correspond to the standard deviation of the galaxy ensemble in each bin.

correlate with D_n4000 but to a lesser extent (e.g., Kauffmann et al. 2003). As our sample is incomplete in mass in the quiescent region of *UVJ* space, but Σ is approximately constant within an SED type, we only examine the latter parameter in this work. Using our subdivided blue star-forming and red quiescent bins we assess how Σ varies with spectral type. In Figures 4c and 4d, we show EW(Hα) and D_n4000 as a function of Σ for each of our stacks. We find that EW(Hα) decreases with increasing Σ, which – due to the relative uniformity of mass in all galaxies but those in region (v) of Figure 2.1 – is likely primarily due to decreasing SFR with Σ and not increasing stellar continuum. We also find that D_n4000 increases as a function of Σ. Taken together, these trends motivate a correlation between decreasing sSFR, increasing age, and Σ. This relation may be causal as suggested in van Dokkum et al. (2015), or driven by some alternate physical mechanism with which both parameters are correlated (Lilly & Carollo 2016). Furthermore, as halos, and by extension star formation, were denser at early times, this sequence could simply be a consequence of the different times at which each of our bins formed their stellar populations with respect to the age of the Universe (e.g., Khochfar & Silk 2006; Abramson & Morishita 2018).

Interestingly, a comparison of our composite spectra and measurements for bins (ii) and (iii) in Figure 2.1 implies that these regions contain related stellar populations. Box (ii) corresponds to galaxies characterized by a recent rapid burst of star formation (e.g., Whitaker et al. 2012; Wild et al. 2016) while box (iii) corresponds to what are usually considered to be dusty star-forming galaxies (e.g., Spitler et al. 2014). However, the similarity in D_n4000 and Hδ_A indicates both regions are comparable in age and have stellar populations dominated by a recent burst of star formation. Comparing EW(Hα) to Hδ_A measurements for (iii), indicates suppressed SFR relative to the rapid past star formation that set Hδ_A. Additionally, galaxies in region (iii) are dusty, with $E(B-V) = 0.41$ derived from the Balmer decrement as described in Reddy et al. (2015). The characteristics of region (iii) galaxies described above, lead us to speculate that these may be dusty post-starburst galaxies that have not yet expelled or depleted their gas and dust reservoirs (Poggianti et al. 2009). In this picture, the galaxies in region (iii) could be the progenitors of galaxies found in region (ii) at later times.

The short star formation timescale we measure for typical galaxies in region (iii) is inconsistent with the picture of a gradual quenching route to quiescence for our redshift range. This result is in contrast with Belli et al. (2015), who examine spectral fitting derived ages and sizes within the quiescent box and suggest the galaxies found in our region (iii) may be progenitors of quiescent galaxies that formed their stellar population over an extended time period, skipping the post-starburst phase all together. It is unclear how to reconcile these results, but the tension may be primarily due to the differing redshift regimes probed in each work; the current study targets slightly higher redshifts. Further measurements may be necessary to understand these discrepancies.

2.6 Discussion

In this letter we constrain SFH as a function of spectral type for a sample of 806 galaxies from the MOSDEF survey at $1.4 \leq z \leq 2.6$. In order to attain the S/N necessary to constrain SFH from stellar continuum features, we bin galaxies based off of physical trends in $U-V$ vs. $V-J$ and utilize

a weighted composite stacking method. We find that transitional and quenched galaxies at $z \sim 2$ have a higher $H\delta_A$ for a given D_n4000 than $z \leq 0.8$ galaxies. Specifically, our $z \sim 2$ galaxies are consistent with shorter star-formation timescales (100-200 Myr) as compared to $z < 0.8$ ($\geq$ 1 Gyr). We find a sequence in (increasing) D_n4000 and (decreasing) EW($H\alpha$) with Σ, highlighting a relationship between evolutionary phase and Σ, whether it be causal or due to mutual correlation with some third physical parameter. Lastly similarities between the age and SFH of what is usually thought of as part of the dusty star-forming region of the *UVJ* diagram, to the post-starburst values, motivates that the former may be dusty post-starburst galaxies.

The unique MOSDEF dataset enabled several improvements compared to past studies. Most importantly, it increased the range of galaxy types for which we could constrain stellar populations and SFHs from stellar continuum spectroscopy, ranging from star forming to transitional to quiescent. Past studies at $z \sim 2$ encompassing the full range of galaxy types focused solely on photometric data, while spectroscopic studies based on stellar continuum at comparable redshifts focused on massive quiescent galaxies. Furthermore, stacking galaxies without subtracting a polynomial fit to the continuum as done in previous works, allows us to measure D_n4000 for a statistical sample of galaxies for the first time at $z \sim 2$.

Nonetheless, there are several caveats to the current work. First, the MOSDEF survey is slightly biased towards unobscured, star-forming galaxies. This bias, combined with lower success rates for the quiescent (i) and post-starburst (ii) galaxies in the MOSDEF survey, results in a small number of galaxies for these bins. Second, our weighting scheme biases our analysis slightly towards brighter galaxies, as these tend to have higher S/N. This bias primarily affects the bins in which there are few galaxies. Finally, we only consider galaxies with MOSDEF redshifts in this work, so we are biased towards post-starburst and quiescent galaxies with emission lines (from AGN) or bright continuum emission. Future work with NIRSpec on the *James Webb Space Telescope* may overcome these problems without relying on stacking, however such observations at $z \sim 2$ will remain challenging. Such larger and more complete samples would enable the use of number density to

Chapter 3

Globular Clusters in High-Redshift Dwarf Galaxies: A Case Study from the Local Group

3.1 Introduction

Given their ancient stellar populations and ubiquity, globular clusters (GCs) have long been used as signposts of star formation in the early universe (e.g., West et al. 2004; Brodie & Strader 2006; Peng et al. 2006). This is especially true of the metal-poor GC population for which the average age in the Milky Way is > 12 Gyr (VandenBerg et al. 2013; Forbes et al. 2015), corresponding to formation at a redshift of $z > 3$, primarily in low mass dwarf galaxies (e.g., Searle & Zinn 1978; Zinnecker et al. 1988; Elmegreen et al. 2012; Leaman et al. 2013). GCs are also uniquely tied to the dark matter (DM) halo masses of their host galaxy (Hudson et al. 2014; Harris et al. 2017) which has been used to infer their number densities at high-redshift (Ricotti 2002; Renzini 2017; Boylan-Kolchin 2017a). Leveraging this to calculate their relative contribution to the high-redshift ultra violet luminosity function (UVLF) has shown GCs may have a non-negligible contribution at absolute UV magnitudes as bright as $M_{\rm UV} = -17$ and could be easily detectable with the *James Webb Space Telescope (JWST)* under most cluster formation assumptions (Katz & Ricotti 2013; Boylan-Kolchin 2017b). These projected number densities at high-redshift make proto-GCs compelling in the context of reionization (Ricotti 2002; Schaerer & Charbonnel 2011; Katz & Ricotti 2013; Boylan-Kolchin 2017b).

To add to this picture, recent observations may be catching GCs in the act of formation. The Hubble Frontier Fields (HFF) program (Coe et al. 2015; Lotz et al. 2017) which leverages flux amplification due to gravitational lensing of source galaxies by massive foreground galaxy clusters, has allowed investigation of a new faint and compact region of parameter space. Emerging observational constraints on the sizes of faint ($-20 \gtrsim M_{\rm UV} \gtrsim -12$) galaxies in the HFF at $z \sim 2-8$, indicate half-light radii < 165 pc ranging as low as 14 pc. Sources fainter than $M_{\rm UV} = -16$ are found to be systematically more compact than originally assumed for completeness estimates in

the UVLF (Kawamata et al. 2015a; Laporte et al. 2016; Bouwens et al. 2017a,c; Kawamata et al. 2017). Recent spectroscopic follow up at $z \sim 6$ and $z \sim 7$, has tentatively classified some of these compact sources as proto-GCs (Vanzella et al. 2017, see also Elmegreen & Elmegreen 2017 for claims of possible proto-GCs at high-redshift)

While studies in the HFF have pushed measurements of the $z \sim 5-7$ UVLF to as faint as $M_{\rm UV} = -13$, it remains difficult to disentangle size, completeness and intrinsic magnitude below $M_{\rm UV} = -15$ (Bouwens et al. 2017b). Understanding the sources contributing at faint magnitudes is however necessary to constrain models of reionization, the vast majority of which rely on low mass galaxies (e.g., Kuhlen & Faucher-Giguère 2012; Robertson et al. 2013, 2015).

A complementary way to study the faint end of the luminosity function is stellar archaeology (Weisz et al. 2014; Boylan-Kolchin et al. 2015, 2016), using resolved stellar populations in the Local Group to reconstruct their star formation histories at high redshift. This has been used to constrain the slope and turnoff of the UVLF at high redshift (Boylan-Kolchin et al. 2014; Weisz & Boylan-Kolchin 2017). As there are multiple GC-hosting dwarf galaxies in the Local Group (LG) with progenitors relevant to reionization, using the LG as a time machine to study the relative detectability of dwarf host and GCs at high redshift is a viable avenue towards understanding the faint-end UVLF.

In this work we extend the fossil record approach to reconstruct the intrinsic and observational features of GCs in their dwarf hosts across redshift. To illustrate the potential of this technique we focus on the Fornax dwarf spheroidal and its five GCs (e.g., McConnachie 2012; de Boer et al. 2012b; Larsen et al. 2012; de Boer & Fraser 2016). Though Fornax has a high specific frequency of GCs, this allows us to do the following: 1) study the relative contribution of objects that could feasibly contribute to the faint end of the UVLF and compare their respective detectability; 2) As metal-poor GCs are postulated to form at $z > 3$ in low mass galaxies (Searle & Zinn 1978; Zinnecker et al. 1988; Bekki et al. 2008; Bekki & Yahagi 2009; Muratov & Gnedin 2010; Forbes et al. 2011; Leaman et al. 2013; Tonini 2013) and dynamical simulations motivate that Fornax's GCs likely formed *in-situ* (Arca-Sedda & Capuzzo-Dolcetta 2016), reconstructing their respective star formation histories allows us to study a common avenue for GC formation holding halo mass constant.

This paper is structured as follows: We divide our analysis into a fixed age and a probabilistic approach. In the former we derive the observational signatures of Fornax's GCs assuming complete knowledge of cluster age and in the latter, we investigate the effects of uncertainty in stellar dating by repeating our analysis using a probability distribution function of GC ages. We proceed to place our findings in the context of current high-redshift observations and their physical interpretation. Finally, we discuss the effect of varying the GC birth to present day mass ratio and prospects for connecting local and high-redshift observations. To convert from lookback time to redshift, we adopt a 2016 Plank cosmology (Planck Collaboration et al. 2016).

GC	Age [Gyr] (1)	Redshift (2)	$M_\star$ at Birth [10^5M$\odot$] (3)	[Fe/H] (4)
1	12.1 ± 0.8	$3.69^{+2.49}_{-1.07}$	0.42 ± 0.10	-2.5 ± 0.3
2	12.2 ± 1.0	$3.88^{+4.54}_{-1.07}$	1.54 ± 0.28	-2.5 ± 0.3
3	12.3 ± 1.4	$4.10^{+26.5}_{-1.83}$	4.98 ± 0.84	-2.5 ± 0.3
4	10.2 ± 1.2	$1.82^{+0.90}_{-0.51}$	0.76 ± 0.15	-1.2 ± 0.1
5	11.5 ± 1.5	$2.82^{+3.95}_{-1.11}$	1.86 ± 0.24	-1.8 ± 0.2

Table 3.1: Summary of GC properties from de Boer & Fraser (2016). For each GC, column (1) shows maximum likelihood ages and their respective standard deviation, column (2) shows these ages in redshift space, column (3) corresponds to inferred GC birth masses assuming a kroupa imf, and column (4) shows the present day metallicity.

3.2 Methodology

In this paper, we use the star formation history (SFH) and ages of globular cluster of Milky Way (MW) satellite galaxy Fornax, combined with stellar population synthesis modeling, to reconstruct their rest frame UV luminosity as a function of redshift. This technique closely follows that described in Weisz et al. (2014) and Boylan-Kolchin et al. (2015), and we refer the reader to those papers for complete details. Below we summarize this methodology and describe the data and modeling choices specific to our study of the field and globular cluster populations of Fornax.

3.2.1 Star Formation History of Fornax's Field Population

For our analysis of Fornax's field population, we use the SFH measured by de Boer et al. (2012b), which is shown as the solid black line in Figure 3.1. This SFH was derived from a deep color-magnitude diagram (CMD) that extends below the oldest main sequence turn-off (MSTO) over 0.8° (r = 1.9 kpc) of Fornax's optical body. As described in de Boer et al. (2012c), the SFH was measured with the `Talos` algorithm, a Kroupa IMF (Kroupa 2001), the Dartmouth stellar evolution models (Dotter et al. 2008) with and age and metallicity range of 0.25 to 15 Gyr and −2.5 to −0.3 dex, respectively. An extensive set of artificial stars was used to account for observational uncertainties and crowding.

3.2.2 The Ages, Masses, and Metallicities of Fornax's Globular Clusters

We use the ages, masses, and metallicities of Fornax's five GCs from de Boer & Fraser (2016), which are listed in Table 3.1. The marginalized age distributions for all five GCs are plotted in Figure 3.2.

The GC properties were measured using the same analysis techniques as for the field population, ensuring self-consistency. Whereas the field population SFH was measured from ground-based observations, properties of the GCs were derived from CMDs constructed from deep HST/WFPC2 archival imaging. HST imaging was necessary to overcome the high degree of crowding in the GCs and reach the MSTO, ensuring age and metallicity determinations comparable in quality to the field population.

In analyzing Fornax's GCs, de Boer & Fraser (2016) adopt a Kroupa IMF, as opposed to their present day mass function. As a result, the reported masses reprinted in column (3) of 3.1 are the *birth* masses of the GCs, assuming that they formed with that IMF. We discuss the role of birth masses in our analysis further in §3.4.4.1.

3.2.3 Reconstructing the ultra-violet fluxes of Fornax and its Globular Clusters

Following the methodology described in Weisz et al. (2014) and Boylan-Kolchin et al. (2015), we reconstruct the rest-frame UV and V-band fluxes of Fornax's field population as a function of redshift using the field SFH (i.e., SFR and metallicity evolution) from the stellar fossil record and the Flexible Stellar Population Synthesis (FSPS) code (Conroy et al. 2009b; Conroy & Gunn 2010). We adopt a Kroupa IMF over a range of .1M$\odot$ to 100M$\odot$, and the Padova stellar evolution models. Though this is a different stellar library than used for the SFH derivation, the Dartmouth models do not include stars younger than 250 Myr, and thus are not adequate for reconstructing the UV flux from massive, young stars.

SFHs derived from the stellar fossil record can typically resolve absolute ages to $\sim 10\%$ (e.g., Gallart et al. 2005, 1 Gyr resolution, 10 Gyr ago). However, both observations and simulations indicate that dwarf galaxies have fluctuating SFRs on timescales of < 100Myr (e.g., Stinson et al. 2007; Ricotti et al. 2008; Governato et al. 2012; Power et al. 2014; Domínguez et al. 2015; Oñorbe et al. 2015a), which affects the UV output from their massive stellar populations. To account for this effect, we insert a stochastic population of short period bursts into the SFH, following the approach described in Boylan-Kolchin et al. (2015). Specifically, we employ a model in which 80% of star formation occurs in 20 Myr bursts that are 20 times stronger than star formation during the intra-burst period. Figure 3.1 illustrates our adopted burst scheme (shown in blue) relative to the fiducial SFH of Fornax. Permutations of the burst parameters are explored in Boylan-Kolchin et al. (2015), and have minimal impact on the conclusions of this paper.

Finally, we account for the difference in the areal coverage of the CMD and the entire galaxy. To do this, we assume that the SFH is representative of the entire galaxy, and normalize the modeled present day V-band to the observed value of $M_V = -13.4$ (McConnachie 2012). Note that while this absolute magnitude includes the light from the GCs, their combined contribution at the present

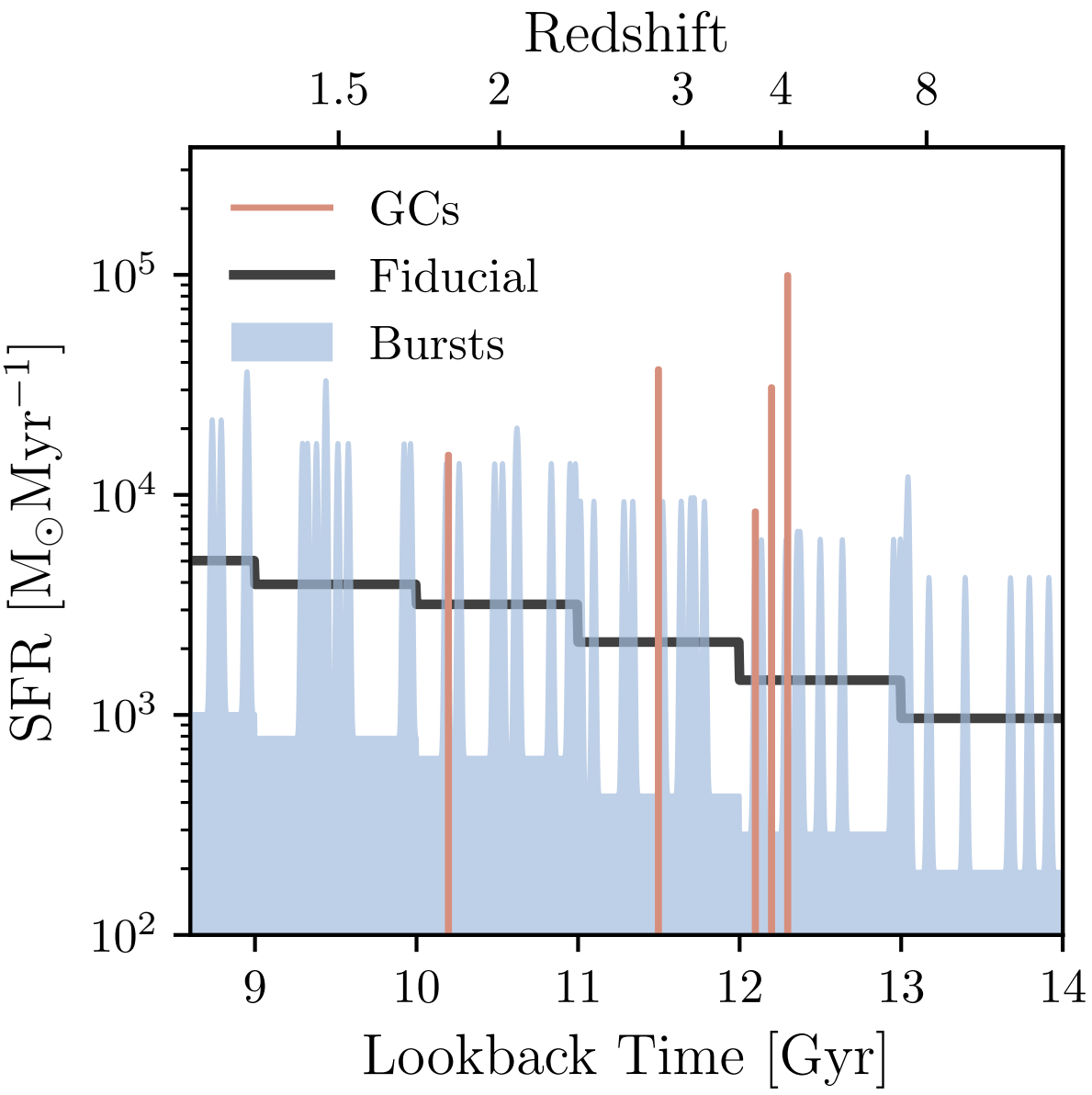

Figure 3.1: The combined SFH of Fornax across time. The fiducial tabulated SFH from de Boer & Fraser (2016) is shown in in black, our physically motivated stochastic burst field SFH is overplotted in blue, while GC formation according to the maximum likelihood cluster ages is shown in orange. The GCs essentially act as intense bursts of star formation, amplifying the burstiness of the field.

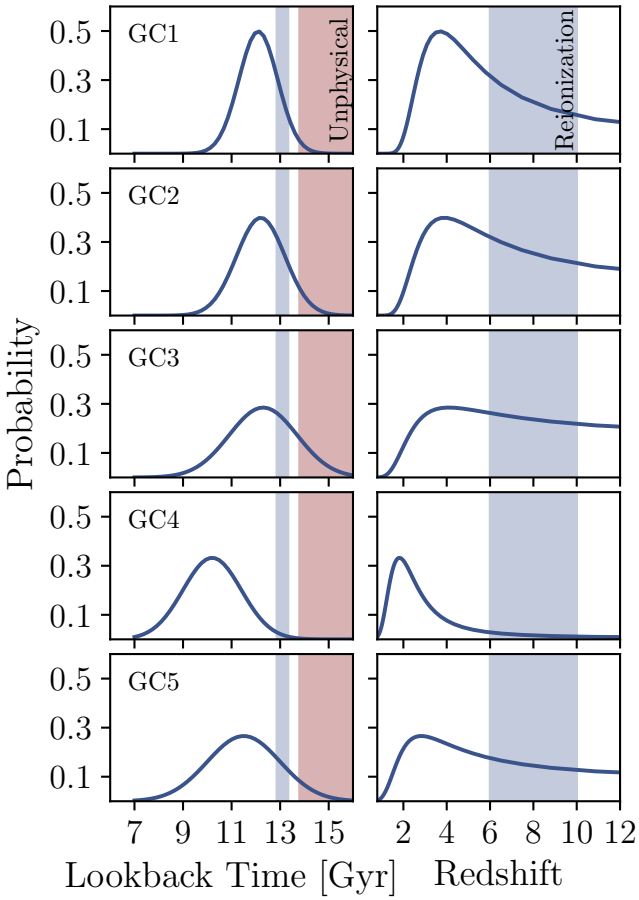

Figure 3.2: Age distribution of each Fornax Globular Clusters as a function of lookback time (left) and of redshift (right). The red shaded region denotes lookback times older than the age of the universe according to the latest Planck release. We use this constraint as a prior when deriving distributions in $M_{\rm UV}$ and $\mu_{\rm UV}$. The blue shaded region corresponds to the epoch of reionization at $6 < z < 10$, which notably corresponds to only 0.7 Gyr in lookback time as illustrated on the left panels.

day is negligibly small ($\sim 1\%$) compared to the luminosity of Fornax's field population. Finally, we omit the uncertainties on the fiducial SFH as their contribution to the UV flux profiles is negligible compared to the variation introduced by short timescale bursts (Weisz et al. 2014). We discuss the role of bursts in §3.3.1.

We reconstruct the UV and V-band fluxes of Fornax's GCs self-consistently with the field population (i.e., same IMF, stellar models, FSPS). We first compute a single flux evolution profile across redshift for each GC, using only the most likely combination of age, metallicity, and mass as listed in Table 3.1. For this reconstruction, we assume a constant SFH over a 5 Myr period, an approximate timescale for star cluster formation (e.g., Lada & Lada 2003; McKee & Ostriker 2007; Lada et al. 2010; Krumholz 2015). This most likely formation scenario is illustrated by the orange lines in Figure 3.1. Effectively, under these assumptions, the GCs appear as additional bursts of star formation on top of the field population, where we've assumed no correlation between star formation in the field and GC formation.

As shown in Figure 3.2, the age uncertainties on the GCs are considerable ($\sim$ 1 Gyr), particularly when plotted as a function of redshift rather than lookback time. Thus, it is important to also consider the effects of these age uncertainties in our reconstruction of UV fluxes.

We do this using a Monte Carlo process. Assuming that the stellar fossil record provides a Gaussian probability distribution function (PDF) in lookback time with mean and standard deviation as listed in Table 3.1. For each age PDF, we randomly draw a GC birth age, and compute its UV and V-band flux. We assume the maximum likelihood values for the mass and metallicity, as these are narrowly peaked and do not change considerably with age within the age pdf of a given cluster. We repeat this process 10^4 times to build up the distribution of $M_{\rm UV}(z)$. We also adopt a prior on age, such that ages allowed by the stellar fossil record, but that exceed the cosmologically derived age of the Universe (Planck Collaboration et al. 2016), are assigned a probability of zero. We discuss the results of this exercise in §3.4.4.2.

We generate an analogous $M_{\rm UV}(z)$ probability distribution function (PDF) for the field by running 10^4 realizations of the bursty SFH described above for the field population to account for the stochasticity of the short duration bursts. We compute the composite field and GC UV flux profiles by summing the two resulting flux distributions.

Finally, we also derive a PDF for surface brightness by using our $M_{\rm UV}(z)$ distributions and adopting sizes for the GC and field populations. For the GCs, we assume an average r_e of 10pc in concordance with sizes of dense bound clusters from simulations (Kim et al. 2017). For the field population, we adopted an r_e = 0.5 kpc corresponding to values from simulated Fornax-like progenitors Ma et al. (2017). We discuss the probabilistic interpretation of our results in §3.3.2.

3.3 The UV Luminosity of Fornax across cosmic time

In this section, we present the reconstructed $M_{\rm UV}$ properties of Fornax. We first consider the case of a bursty field SFH coupled with the most likely GC ages. We then factor in uncertainties in the GC ages measured from the stellar fossil record. This division first allows us to illustrate the substantial impact of GCs on Fornax's luminosity modulo complications from the stellar fossil

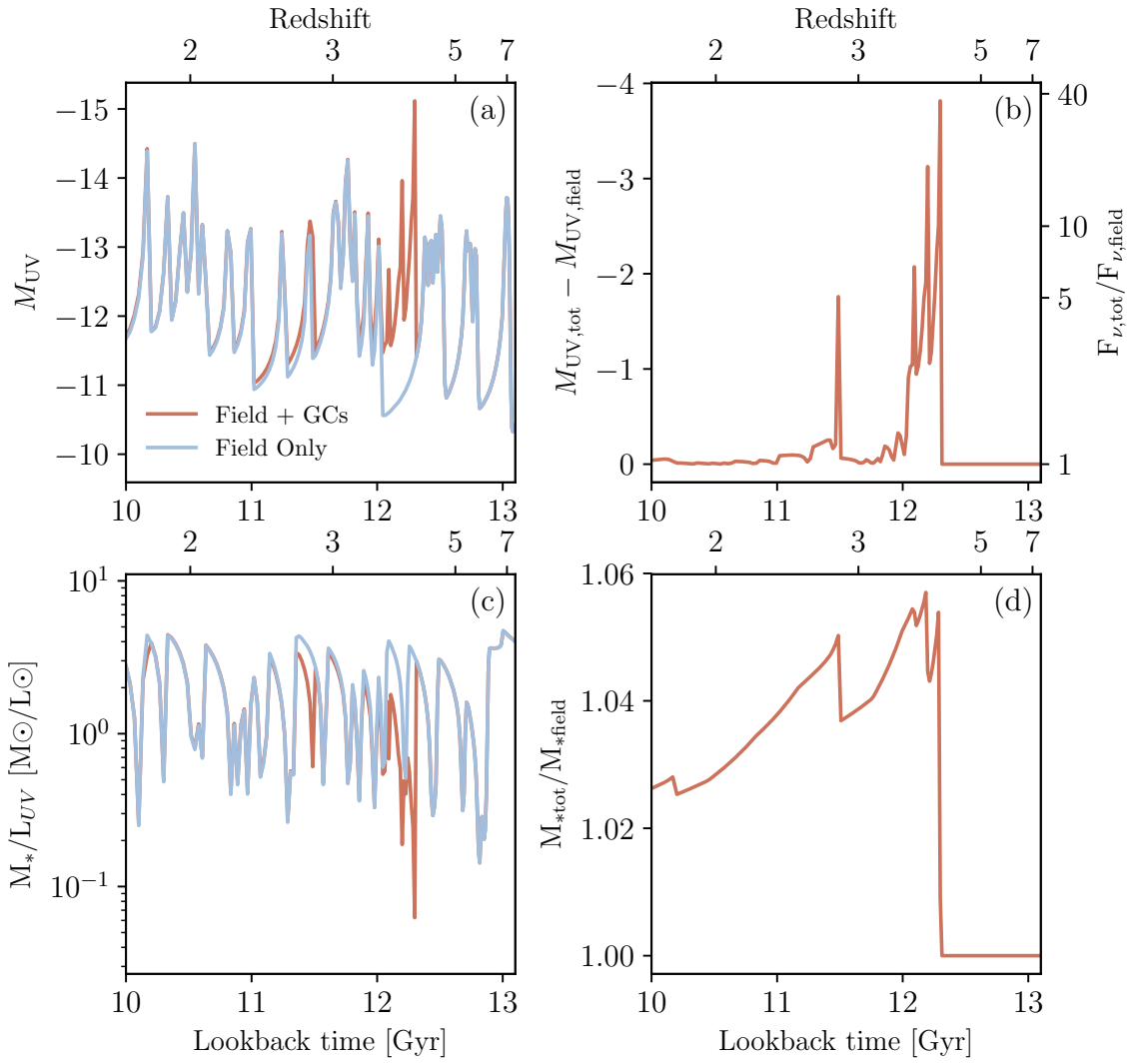

Figure 3.3: The reconstructed UV luminosity and stellar mass of Fornax across cosmic time for a standard field SFH. Panel (a): $M_{\rm UV}$ as a function of redshift and lookback time, where the blue line corresponds to the UV magnitude from solely the field and the orange line corresponds to the contribution of GCs assuming the most likely formation time for each of the 5 clusters. The combined field and GC population is at least one magnitude brighter than a typical burst of star formation in the field. This increase allows for substantially more robust measurements in the HFF. Panel (b): The difference in absolute magnitude between the field and the combined field and GC populations. This corresponds to a difference of ~ 4 mags for this example field SFH scenario. Panel (c): The mass to light (ML) ratio in the UV normalized to the mean field ML ratio, as a function of redshift and lookback time. Though the field ML ratio remains within a magnitude of the mean field ML ratio, proto-GCs can differ by over an order of magnitude. Panel (d): The relative mass of GCs to the field. GCs account for $< 5\%$ of the system's mass but can contribute fifty times the UV luminosity.

record. We then fold in the uncertainties to demonstrate how current limitations from the stellar fossil record affect our results.

3.3.1 Most Likely Globular Cluster Ages

Figure 3.3 shows the UV flux evolution of Fornax across cosmic time assuming the bursty SFH described in §3.2.3 and the maximum likelihood age of each GC. As illustrated in blue in panel (a), the short timescale bursts and lulls can change the UV flux of the field population by ~ 2 mag, which is identical to the findings in Weisz et al. (2014) and Boylan-Kolchin et al. (2015). Unlike these studies, we now also consider the impact of the formation of GCs, shown in orange. The short (5 Myr), intense periods of star formation that result in formation of proto-GCs, have the same effect on the UV flux as extremely strong bursts of star formation. More concretely, the formation of (proto-)GCs can increase the UV luminosity of Fornax by factors ranging between $\sim 10 - 100$ over periods of a few 10s of Myr depending on star formation in the field. In panel (b) of Figure 3.3, we show the UV flux ratio of proto-GC to field for an example at the center of this range. See §3.6 for limiting examples. This illustration has several implications for the interpretation of objects (nominally assumed to be galaxies) directly detected at high redshift.

Panel (c) of Figure 3.3 illustrates how the bursty field SFH and the formation of GCs affects the ratio of stellar mass to UV luminosity (M/L). The bursty SFH (blue) typically causes fluctuations in the M/L ratio that vary by less than an order of magnitude. In contrast the formation of GCs causes a drop in the M/L ratio that can be larger than an order of magnitude. We quantify this effect further in the next paragraph, and discuss the complications that GC formation may introduce into inferring stellar masses, and in turn halo masses, of high-redshift galaxies in §3.4.2.

Fornax's GC population accounts for $\lesssim 5\%$ of the total stellar mass of Fornax at an given time as shown in panel (d). Comparing this to panel (b) for the same time interval, GC formation produced up to 50 times more UV luminosity than the field population. In relative terms: despite comprising only 5% of Fornax's stellar mass at $z \sim 4$, the GCs account for 98% of total UV flux emitted.

Interestingly, the temporal clustering of GC formation in Fornax, means that the GCs dominated the UV output of Fornax between $\sim 12 - 12.3$ Gyr ($z = 3.51 - 4.10$) with the peak of $M_{\rm UV} = -15.3$ mag. The troughs in normalized UV flux seen in panel (a) of Figure 3.3 during this period correspond to dimming of the GCs (which happens on the order of 50 Myr) and to a lesser extent star formation in the field. Though the mass fraction of GCs does not vary substantially with each realization of stochastic star formation in the field, the fraction of luminosity contributed by GCs is dependant on the amount of star formation in the field. The values shown here correspond to an average field SFH.

3.3.2 Probabilistic Approach

In the limit of perfect knowledge of GC ages, the above analysis would fully capture the luminosity evolution of Fornax across time. However, uncertainties[1] in ages absolute ages derived from the fossil record are typically of order 10% of the lookback time, which can be substantial (e.g., Gallart et al. 2005, 1 Gyr at 10 Gyr $z = 2^{+1.388}_{-0.719}$).

To estimate the effects of these age uncertainties on our $M_{\rm UV}$ determinations, we use the Monte Carlo approach described in §3.2.3 to create a probability distribution for the field and GC UV luminosities. The resulting $M_{\rm UV}$ PDFs are shown in Figure 3.4 for redshifts $z = 3$ (panel (a)) and $z = 7$ (panel (c)), which were selected to illustrate the general picture of GC formation near the peak of star formation in the universe ($z \sim 2 - 3$) and during the epoch of reionization ($z \sim 7$).

The bimodal distribution seen in both redshift slices is due to the short and bursty star formation in the field. The more probable faint peak of the distribution (at $M_{\rm UV} \sim -11.1$ at $z = 3$ and $M_{\rm UV} \sim -10.5$ at $z = 7$) corresponds to periods between bursts and the less probable peak (at $M_{\rm UV} \sim -13.7$ at $z = 3$ and $M_{\rm UV} \sim -12.6$ at $z = 7$) corresponds to stochastic bursts falling within tens of Myr of the considered redshift slice.

At both redshifts, including GCs only shifts the PDF of the field incrementally towards brighter $M_{\rm UV}$. Their main contribution is to add a tail to the bright end of the distribution. At z = 3, this tail corresponds to a maximum $M_{\rm UV} = -15.5$, which is a magnitude brighter than the field maximum. At $z = 7$ the max $M_{\rm UV} = -15.3$ and is 3.5 mag brighter than the field. This smaller offset is due to the lower probability of formation for GCs by $z = 7$ than by $z = 3$. This offset corresponds to a roughly 2% probability that at a given instance, proto-GCs dominate their host's UV luminosity. This is a non-negligible percentage given the ubiquity of Fornax like halos in the Universe.

As shown in Figure 3.4, GCs are more likely to be detected at high redshift than their dwarf galaxies hosts. This is especially relevant for current photometric surveys at these faint magnitudes, as the selection efficiency in the HFF is largely predicated on source size near the surface brightness detection limit (Grazian et al. 2011). We therefore examine the surface brightness ($\mu_{\rm UV}$) probability distribution of the Fornax field compared to its GCs in panels (b) and (d) of Figure 3.4 for $z = 3$ and $z = 7$, respectively. At both redshift slices, the two distributions are completely distinct and are separated by $\sim 14\ mags/arcsec^2$. There is an 85% likelihood that at least one GC has formed by $z = 3$, whereas at $z = 7$ this is lower at 43%. The slightly higher GC surface brightness possible at $z = 3$ is due to this higher probability of formation and the corresponding increased likelihood of detecting a proto-GC at its most luminous. Finally, in Figure 3.4 we plot compact objects spectroscopically followed up by Vanzella et al. (2017) along with our PDFs. We comment on their remarkable similarities in §3.4.1.

[1]Here we consider uncertainties to be the precision in GC ages. The issue of absolute ages, i.e., the accuracy in mapping age to redshift, is an equally important, though a much more challenging problem. We discuss these challenges further in §3.4.4.2.

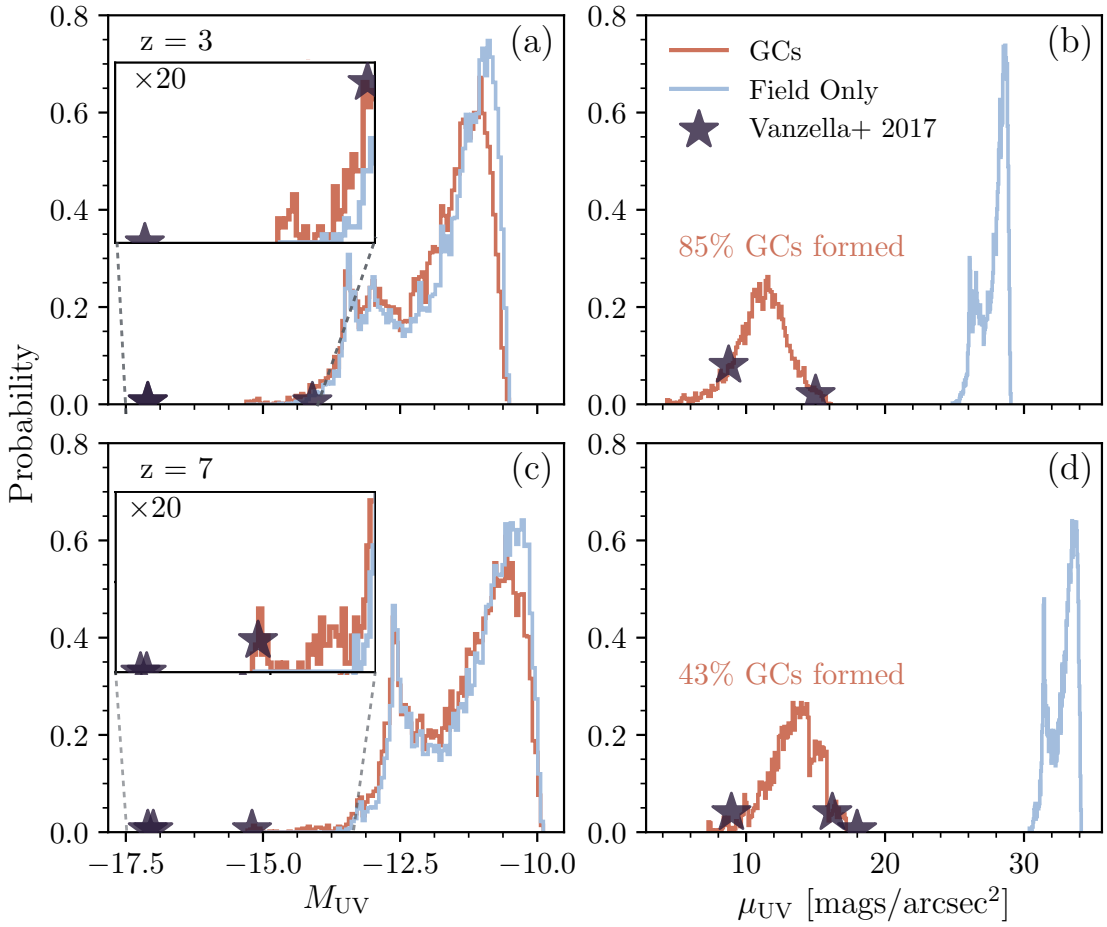

Figure 3.4: The probability distribution functions of Fornax and its GCs at select redshifts. Panels (a) and (c): Distribution of $M_{\rm UV}$ for z = 3 (panel (a)) and z = 7 (panel (c)), where the orange corresponds to the combined GCs+field while the blue corresponds to the field only distribution. In the subpanels of panels (a) and (c) We show a zoom-in (y-axis ×20) on the region of the field + GC PDF corresponding to 2% cumulative probability. At all redshifts the PDF of the combined population is shifted towards more negative magnitudes. This effect is maximized at z~ 3 when globular clusters are most likely to form. Panels (b) and (d): PDF of μ_{UV} where here the orange line corresponds to the GC only PDF and the blue still demarcates the field. The two distributions are completely distinct, with the GC PDF falling within the robust detection range of the HFF while the field distribution does not. For both the right and left panels, we overplot the spectroscopically confirmed objects from Vanzella et al. (2017) as purple stars. The objects that fall on the GC distribution in both the $M_{\rm UV}$ and $\mu_{\rm UV}$ PDFs are most likely to indeed be proto-GCs.

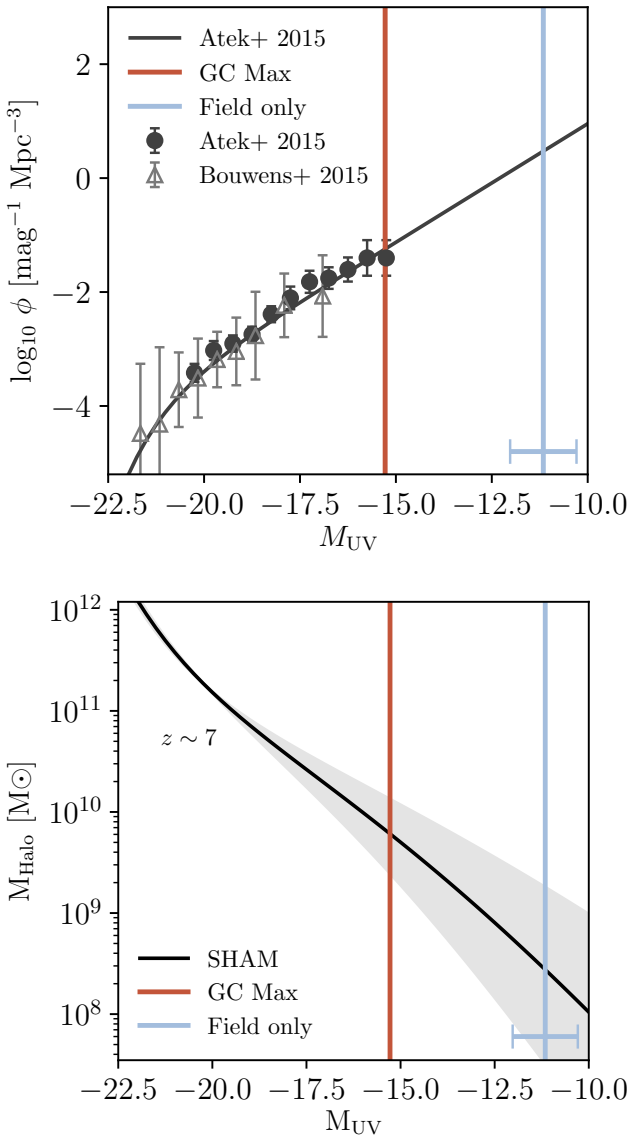

Figure 3.5: Illustration of the impact of GC formation on the UVLF and abundance matching at high redshift. On left: comparison of our modeled magnitudes with the luminosity function of $z \sim 7$. We show the best fit UVLF and measured points from Atek et al. (2015) in black, as well as the measurements from Bouwens et al. (2015) in grey. The maximum GC+Field magnitude, shown in orange falls within the detection range of Atek et al. (2015), while the Fornax field on its own, shown in blue, does not. On right: $M_{\rm Halo}$ as a function of $M_{\rm UV}$. In black, we show a SHAM relation derived from Sheth et al. (2001) and Finkelstein (2016), where the grey region corresponds to variations of ±0.3 in the faint end slope of the UVLF. In blue and orange we show where the Fornax field and its proto-GCs would respectively fall on this relation. Abundance matching using the $M_{\rm UV}$ from the field is consistent with the halo mass inferred for Fornax, whereas accounting for GCs can overestimate this by an order of magnitude.

3.4 Discussion

3.4.1 Proto-Globular Clusters in the Hubble Frontier Fields

Gravitational lensing is a powerful means of detecting faint objects in the high-redshift Universe (e.g., Atek et al. 2015; Alavi et al. 2016; Livermore et al. 2017; Bouwens et al. 2017a). However, the nature of shear and flux amplification from lensing, means that the HFF yields preferential detection of compact, rather than extended sources, for a given intrinsic magnitude and magnification parameter (e.g., Grazian et al. 2011; Wong et al. 2012; Oesch et al. 2015; Atek et al. 2015; Alavi et al. 2016; Bouwens et al. 2017a).

Figure 3.4 illustrates this effect for Fornax. Both the field and GCs are near the detection UV flux limit of the HFF (Grazian et al. 2011), but the PDF for GCs at a both $z = 7$ and $z = 3$ is centered at a substantially higher surface brightness than the field. This is simply due to their relative sizes. Thus, at faint magnitudes in the HFF, it is substantially more likely to detect a GC in Fornax, than Fornax itself. Based on this analysis, we caution that some of the faintest objects detected at high redshift (e.g., $M_{\rm UV} = -12.5$ at $z = 7$; Livermore et al. 2017) to date may in fact be GCs hosted by faint galaxies, and not faint galaxies themselves.

This conjecture is consistent with recent demonstrations that faint objects in the HFF are generally quite compact (e.g., Kawamata et al. 2015a; Laporte et al. 2016). For example, Bouwens et al. (2017a) show a large population of faint ($M_{\rm UV} \leq -16$) fall between 15 pc $< r_e <$ 55 pc at $z \sim 6$. While we find both the Fornax field and GCs to potentially have UV magnitudes on par with these objects, the surface brightness we infer for its GCs at $z = 3$ and $z = 7$ are more consistent with these results than the field population alone.

Figure 3.4 also compares the spectroscopically confirmed compact objects detailed in Vanzella et al. (2017) to our findings for Fornax. Interestingly, all of the high-redshift objects are consistent with the GC surface brightness distribution, but not the field population distribution. Notably, both the proto-GC candidates fall on the $M_{\rm UV}$ distribution for Fornax GCs as well.

Moreover, the high-redshift objects and Fornax GC have similar physical properties. For example, Fornax GC3 has a mass of $\sim 5 \times 10^5$ M$_\odot$, which corresponds to an SFR of $\sim 0.1 M_\odot yr^{-1}$ and a maximum $M_{\rm UV}$ of -15.2. The most comparable high-redshift object reported by Vanzella et al. (2017) is GC1 at $z = 6.145$, which has a stellar mass of $0.8 - 130 \times 10^6$ M$_\odot$, an SFR between $0.04 - 6.6 M_\odot yr^{-1}$, $M_{\rm UV} = -15.3$ mag. The similarity of these values suggests that GC1 ($r_e \sim 10$ pc), may be a proto-globular cluster, though the uncertainties in the SFR and mass are large. More generally, this type of comparison reinforces the conclusions of Vanzella et al. (2017), i.e., that they have observed star clusters, and strengthens the potential for connections between compact objects found in the local Universe and those at higher redshifts.

3.4.2 Globular Clusters, the UV Luminosity Function, and Abundance Matching

The left panel of Figure 3.5 illustrates how the GC formation can affect Fornax's position on the $z = 7$ UVLF. The broader implication of this GC-driven brightening is that, at least in part, GCs

could be counted as galaxies in current UVLF determinations. That is, if GCs from fainter, more numerous galaxies are being counted as more luminous galaxies on their own, it not only biases the UVLF, it also washes out potential structure at the faint end. This could inhibit surveys from detecting the turnover in the UVLF, which is expected from a number of detailed simulations of high-redshift galaxy populations (e.g., Jaacks et al. 2013; O'Shea et al. 2015; Gnedin 2016; Finlator et al. 2017), as well as consistency with the stellar fossil record and number counts of Local Group galaxies (e.g., Boylan-Kolchin et al. 2014, 2016; Weisz & Boylan-Kolchin 2017).

Intriguingly, Bouwens et al. (2017b) indicates that there may be a tension between the faint-end UVLF slope from the HFF versus HUDF. Given differences in the selection effects of lensed vs. blank fields (as discussed in §3.4.1), this may be a sign that proto-GCs are making non-negligible contributions to the UVLF. Broader implications of how GC-galaxy confusion at high-redshifts affects reionization and the UVLF have been discussed at several places in the literature (see Boylan-Kolchin 2017a,b; Bouwens et al. 2017c).

Proto-globular cluster formation may also affect abundance matching relationships. To investigate the implications of this, we calculate the stellar-halo abundance mass relation (SHAM) given the Sheth et al. (2001) halo mass function and the $z = 7$ UVLF from Finkelstein (2016), varying the fiducial faint end slope over $\Delta\alpha = \pm 0.3$ to encapsulate the proposed values in the literature (e.g, Stark 2016a).

The right panel of Figure 3.5 shows that for the case of Fornax at $z \sim 7$, if its UV luminosity is dominated by a proto-GC, then the assigned halo mass would be over-estimated by a factor of ~ 20 given our fiducial faint end slope. That is, the UV luminosity of the field population alone would correspond to a halo mass of 3×10^8 $M_\odot$, whereas including the luminosity boost from GC formation would imply a halo mass of 6×10^9 $M_\odot$. This increases to a factor of ~ 70 if we consider a steeper faint end slope as some studies suggest (Livermore et al. 2017; Ishigaki et al. 2017). Though the exact difference will depend on the adopted SHAM, the order-of-magnitude discrepancy for the fiducial case is approximately correct, as all SHAMs are similarly steep. Beyond revealing a shortcoming in abundance matching at high redshifts, this mis-assignment of halo masses has a range of implications ranging from incorrectly interpreting the astrophysics of faint UV sources to differentiating between dark matter models, which can predict different shapes to the faint end of the UVLF (e.g., Schultz et al. 2014; Bozek et al. 2015; Menci et al. 2017).

3.4.3 Globular Clusters in Other Local Group Dwarfs

As the Fornax field approaches the detection limit of the HFF, we can leverage our results to predict the high-redshift observability of fainter and brighter GC hosting dwarfs. In fainter hosts, GCs can act as tracers of galaxies that would be beyond the detection limits of present or future surveys. There are four local group dwarfs fainter than Fornax that host a star cluster: PegDIG ($M_V = -12.2$; Cole et al. 2017), AndI (M_V = -11.7; Cusano et al. 2016), AndXXV (M_V = -9.7; Cusano et al. 2016), and Eridanus II (M_V = -7.1; Crnojević et al. 2016). With the possible exception of PegDIG, the progenitors of these galaxies will not be observable at redshifts relevant to reionization, even with *JWST* (Boylan-Kolchin et al. 2015). By the surface brightness projections made in this paper, their

GCs may however be detected. This could be used to constrain the number density of extremely faint galaxies and inform models of reionization (e.g., Robertson et al. 2013, 2015).

The progenitors of GC-hosting LG dwarfs brighter than Fornax, like WLM ($M_{\rm V} = -14.2$ Leaman et al. 2012), NGC 6822 ($M_{\rm V} = -15.2$ Hwang et al. 2011; Huxor et al. 2013), the LMC and SMC (e.g., Forbes et al. 2015), could fall within the robust surface brightness detection limits of the HFF. This means one could simultaneously observe the host and its proto-GCs at high redshift, informing our picture of high-redshift star formation.

3.4.4 Next Steps: Building Connections Between Local Globular Clusters and High-Redshift Compact Objects

Up to this point, we have used LG dwarf galaxy Fornax and its GC population to illustrate a fundamental connection between the stellar fossil record of local systems with high-redshift observations. Given such studies are in nascent stages, we now highlight a few ways in which local and high-redshift studies of clusters can be strengthened.

3.4.4.1 The Impact of Globular Cluster Birth Mass

One challenge in connecting GCs observed in the local Universe with putative progenitor populations at high redshifts, lies with their stellar masses. It is well-established that low-mass stars have been ejected from GCs over their lifetimes due to dynamical interactions within the dense cluster environment (e.g., Ostriker et al. 1972; Chernoff et al. 1986; Gnedin et al. 1999; Fall & Zhang 2001).

The effect of this 'evaporation' is that GCs today are likely to be less massive that when they formed. In turn, the more massive a GC was when it formed, the brighter it would have been (assuming a Galactic-like stellar IMF). Furthermore, most theoretical explanations for the presence of multiple populations in MW GCs require that they formed with significantly larger stellar masses (factors of 10-100; e.g., Piotto et al. 2012; Renzini et al. 2015). However, see Bastian & Lardo (2017) for claims that these scenarios are not physically viable.

In the case of Fornax, there are indications that its GCs have lost no more than a factor of few in stellar mass over their lifetimes. Comparisons between the metal-poor star population in the field of Fornax and the GC metallicities suggest that cluster stellar mass loss is no more than a factor of 4-5 (Larsen et al. 2012; de Boer & Fraser 2016).

In this paper, we have used estimates of GC *birth* mass for our analysis. In modeling the CMDs of Fornax's GC population, de Boer & Fraser (2016) assumed a Kroupa IMF, which would correct for the mass loss affect, under the assumption that the GCs formed with that IMF. However, if the assumption of a Kroupa IMF is not correct (Zaritsky et al. 2012) and/or the birth masses of Fornax GCs were larger than we have assumed, Fornax's GC may have been even more UV-luminous than we find.

3.4.4.2 The Role of Absolute Age Uncertainties

In our analysis, we have assumed a specific mapping between lookback time and redshift. However, it is well-established that stellar and GC absolute ages are uncertain and depend on the detailed stellar physics (see Soderblom 2010, and references therein). This introduces challenges into translating ages from the fossil record into a cosmological reference frame (i.e., redshift).

Figure 3.2 illustrates this issue. Here, the inferred age distribution as a function of lookback time is Gaussian. However, in terms of redshift a significant portion of the PDF extends to ages older than allowed by cosmological models. Improving knowledge of absolute ages requires better observational (e.g. absolute distances; VandenBerg et al. 2013; Chaboyer et al. 2017; O'Malley et al. 2017) and theoretical underpinning (e.g. stellar physics; Bonaca et al. 2012; Tanner et al. 2014; Creevey et al. 2015).

A related issue is the precision to which GC ages can be measured. In the case of Fornax, de Boer & Fraser (2016) report GC ages to a precision of ±1 Gyr. As Figure 3.2 shows, this translates into considerable uncertainty on the redshift distribution. Even if absolute ages were not an issue, determining whether a given GC formed before/during/after the epoch of reionization is challenging simply owing to precision. As illustrated in Figure Figure 3.2, the epoch of reionization is ~ 0.7 Gyr in duration, and sets a requirement on the precision to which GC ages from the stellar fossil record must be known to determine their relationship to reionization.

There are several avenues that should improve the precision, and possibly accuracy, to which GC ages can be measured. First, *Gaia* (Lindegren et al. 2016b), will provide distance measurements to galactic GCs with a precision of $\approx 1\%$, a factor of > 10 improvement over most distance estimate to date. Such precise parallaxes should limit GC age precision to no less than 10% (Pancino et al. 2017). Second, the accessibility of the 'MS kink', a feature in the low-mass portion of the CMD caused by changes in atmospheric opacity, may improve age precision. The MS kink is metallicity sensitive, and could mitigate the age-metallicity degeneracy that affects measuring GC properties from the MSTO (Correnti et al. 2016). Determining absolute GC ages is a far more challenging problem as it requires an improved understanding of detailed stellar physics (e.g., VandenBerg et al. 2013; Chaboyer et al. 2017; Tayar et al. 2017).

3.4.4.3 Detecting proto-Globular Clusters at High Redshifts

Based on arguments advanced in this paper and elsewhere, it appears that proto-GC are likely already being detected at high redshifts in the HFF. Future spectroscopic follow up of these sources may help confirm their nature as proto-GC through determinations of stellar and dynamical mass, specific star formation rates, and secure redshifts, which can substantially improve size determinations (e.g., Treu et al. 2015, and references therein).

Unfortunately, ancient metal-poor GCs like four of the ones found in Fornax, should not have a detectable Ciii] doublet, which is the brightest spectral signature in the restframe UV after Lyα (Stark et al. 2014). Line emission from the Ciii] doublet peaks at a metallicity of $\log Z = -0.7$ (Erb et al. 2010) and becomes more difficult to detect for metallicities lower than $\log Z = -1.5$, even for sources with high ionization parameters (Jaskot & Ravindranath 2016).

One possible way to uniquely detect proto-GCs at high redshift may arise from the multiple chemically distinct populations found in Galactic clusters (e.g., Gratton et al. 2012; Piotto et al. 2012). The so-called 'second generation' of stars exhibits distinct abundance patterns such as Helium enhancement and anti-correlations between oxygen and sodium (e.g., Villanova et al. 2012; VandenBerg et al. 2013; Bastian & Lardo 2017). Presumably, such unusual chemical signatures could be seen in emission as the proto-GC were forming.

3.5 Summary

In this work, we reconstructed the UV luminosity of the Fornax field and its GCs using their respective stellar fossil records combined with stellar population synthesis modeling. We have shown that forming GCs can be substantially brighter than their dwarf galaxy hosts at high redshift. Specifically, we find:

(i) Proto-GCs can emit 50 times the UV luminosity of their dwarf galaxy hosts despite comprising $\leq 5\%$ of the total mass.

(ii) Forming GCs can be brighter than $M_{\rm UV} = -15$, which lies in the robust detection limit of the HFF at $z \gtrsim 6$.

(iii) GCs are described by a substantially higher surface brightness PDF than their dwarf galaxy hosts.

Given that both Fornax and its GCs are near the detection UV flux limit of the HFF, the higher surface brightness of GCs means they are more likely to be detected than a dwarf galaxy that hosts them. We further assess the implications of preferentially detecting clusters and find:

(i) Miscategorizing GCs as galaxies at high-redshift could bias the UVLF and wash out signatures of a turnover at the faint end.

(ii) Inferred halo masses from abundance matching relations could be more than an order of magnitude too massive if a proto-GC is mistaken for its host dwarf galaxy.

With improvements in age precision from *Gaia* and enhanced detection limits and spectroscopy from *JWST*, synthesizing low and high redshift observations is a promising avenue for understanding the formation of GCs and their role in the early universe.

3.6 GC Formation with Varying Field SFH

The UV flux ratio between proto-GCs and the field for the Fornax dwarf spheroidal ranges between $\sim 10 - 100$ depending on the relationship between star formation in the field and GC formation. We explicitly illustrate the effect of this relationship on the UV luminosity breakdown of Fornax in Figure 3.6. We show two limiting cases: panels (a) and (b) correspond to the limit were GC

formation is coincident with a lull in field star formation, while panels (c) and (d) show GCs forming at a peak of star formation in the field.

Hydrodynamical simulations show clusters are likely to form when there is an enhancement of cold gas reservoirs in the galaxy (Kravtsov & Gnedin 2005); however, this does not necessarily correspond to enhanced star formation in the field especially for metal-poor GCs (i.e.: four of the Fornax GCs). Generally these are thought to form either earlier than the primary epoch of star formation in the galaxy(e.g., Forbes et al. 1997), from dissipational collapse at the center of low-mass halos in assembly based models of GC formation (e.g., Tonini 2013), or in high-redshift merger events that require only enough cold gas to form a GC (i.e: $> 10^5 M_\odot$) (e.g., Li & Gnedin 2014). Depending on the GC formation mechanisms at play within Fornax, we would expect varying degrees of correlation between star formation in the field and GC formation. The case in which GC formation is highly correlated with star formation in the field is shown in panels (c) and (d) of Figure 3.6.

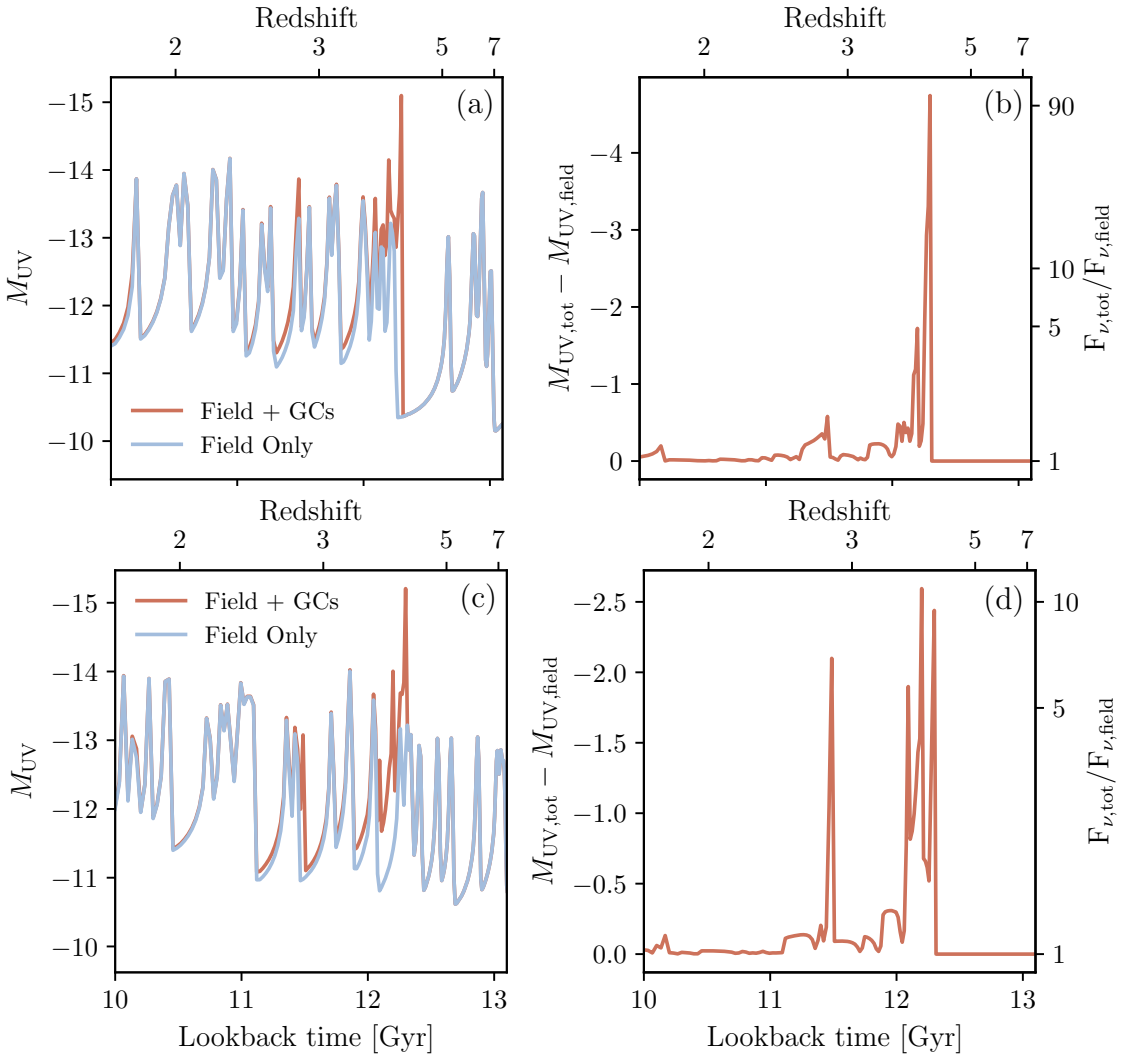

Figure 3.6: The reconstructed UV luminosity of Fornax across cosmic time for extreme cases of field star formation with respect to GC formation. Panel (a): $M_{\rm UV}$ as a function of redshift and lookback time, where the blue line corresponds to the UV magnitude from solely the field and the orange line corresponds to the contribution of GCs assuming the most likely formation time for each of the 5 clusters. The formation of GCs corresponds to a lull in star formation in the field. Panel (b): The difference in absolute magnitude between the field and the combined field and GC populations. This corresponds to a difference of ~ 5 mags for this low field star formation scenario. Panel (c): Shows the same quantities displayed in panel (a) but for a field SFH corresponding to a simultaneous burst in galaxy star formation and GC formation. Panel (d): For this case, the maximum difference in magnitude between proto-GCs and the field is 2.5 mags, this means forming GCs are still ten times more luminous in the UV than the burst in the field.

Chapter 4

Towards Studying Hierarchical Assembly in Real Time: A Milky Way Progenitor Galaxy at $z = 2.36$ under the Microscope

4.1 Introduction

Galactic archaeology of the Milky Way (MW) is among the primary testbeds for hierarchical galaxy assembly (e.g., Freeman & Bland-Hawthorn 2002; Madau et al. 2008; Brown et al. 2012; Bovy et al. 2012). The ages, abundances, and kinematics of individual stars and star clusters (globular and otherwise) encode the entire formation history of the MW back to the dawn of star formation. Increasingly detailed studies suggest that our MW had an active accretion and star formation history (SFH) in the early Universe, but has mainly undergone secular evolution in the last several Gyr (e.g., Belokurov et al. 2018; Haywood et al. 2018; Helmi et al. 2018).

A number of studies have extended such archaeological techniques beyond the MW. For example, results from the Pan-Andromeda Archaeological Survey (PAndAS) suggest that M31 has had a more active recent accretion history than the MW (McConnachie et al. 2009). Similarly, other ambitious efforts with observations of resolved stars and/or integrated light are in the process of revealing the formation histories of MW analogs throughout the Local Volume (e.g., Mouhcine et al. 2005; Monachesi et al. 2016; Merritt et al. 2016).

Ideally, it should be possible to connect this galactic archaeology approach directly to observations of accretion and star formation of MW-like ancestors at higher redshifts. Though indirect studies relying on galaxy number densities have shed light on hierarchical formation (Leja et al. 2013; van Dokkum et al. 2013), establishing direct links has proven challenging. This is primarily because even fairly substantial accretion events in the history of the MW (e.g., Gaia-Enceledus, Helmi et al. 2018) would amount to a 1:10 minor merger, which lies at the mass ratio limit of current high-redshift merger classification schemes (Lotz et al. 2008, 2011; Ribeiro et al. 2017).

At the same time, observations of the Hubble Frontier Fields (HFF; Lotz et al. 2017) are poised to transform our capacity to study sub-structure (e.g., minor accretion events, star cluster formation)

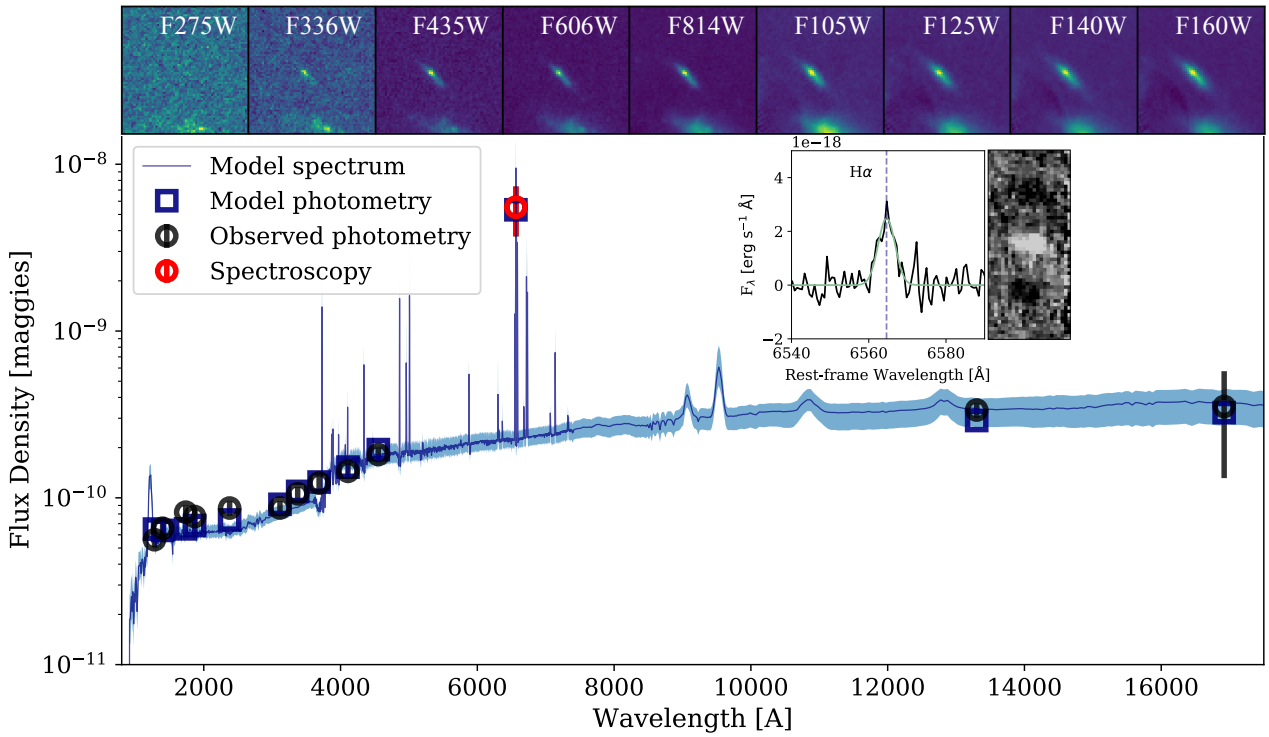

Figure 4.1: The HST images, SED, and MOSFIRE spectrum of the galaxy plus clump. **Main panel:** PROSPECTOR non-parametric SED fit including constraints from our MOSFIRE Hα measurement (shown in orange). The 16th and 84th percentile fits to the SED are shown in light blue. **Inset panel:** MOSFIRE Hα measurement, where the black line is our raw data, the grey is our error and the teal is our fit to the line. **Top panels:** non-psf matched photometry in each HST filter considered.

in and around the progenitors of MW-like galaxies at high-redshift. Compared to blank fields, the magnification power of gravitational lensing in the HFF provides both the spatial resolution and sensitivity to identify and characterize luminous features with sizes and luminosities comparable to star-forming regions and bright satellite galaxies in the local Universe over most of cosmic time (e.g., Swinbank et al. 2015; Kawamata et al. 2015b, 2018; Bouwens et al. 2017a,c).

Intermediate redshift galaxies (1 < z < 3) have long been known to have higher degrees of sub-structure (usually referred to as "clumps") than their lower-redshift counterparts in restframe optical wavelengths (e.g., Förster Schreiber et al. 2011; Elmegreen et al. 2012; Wuyts et al. 2012; Genzel et al. 2011; Shibuya et al. 2016). Pioneering studies in the rest-frame optical have even characterized the properties of these clumps as a function of spatial distribution within their host galaxies (e.g., Guo et al. 2018; Zanella et al. 2019). However, the higher spatial resolution afforded by lensing has shown ~1 kpc clumps to either be multiple more compact clumps, or simply smaller clumps with stellar masses overestimated by up to an order-of-magnitude (e.g., Dessauges-Zavadsky

et al. 2017; Cava et al. 2018). In principle, such observations can begin to reveal the degree of sub-structure around high-redshift galaxies, allowing us to directly explore hierarchical galaxy formation scenarios in the early Universe.

However, even with improvements in spatial resolution due to lensing, it remains challenging to discern the true nature of these clumps (i.e., *in-situ* star formation vs. accretion). For example, Zanella et al. (2015), identified an off-center clump in [O iii] Integral Field Unit spectroscopy data, that was not detected in broadband filter observations of a $z = 1.9$ galaxy. Though the [O iii] implied it was a young cluster, the spatial resolution of the line emission identified clump was ∼500 pc, which too coarse for even a star-forming complex (see Krumholz et al. 2019, and references therein). Additionally, Rujopakarn et al. (2019) used ALMA's 30 milliarcsec capabilities to study dust clumping on 200 pc scales in $L_\star$ galaxies identified in the Hubble Ultra Deep Field (UDF). However, the resolution of the UDF imaging courser than ALMA, meaning that ∼ 100pc counterparts in the restframe optical would likely be smoothed out to much larger effective sizes (Tamburello et al. 2017; Gullberg et al. 2018), creating a mismatch between the dust and galaxy scales. Finally, at $z \sim 6$, Vanzella et al. (2019) combined HFF photometry with MUSE spectroscopy to study Ly-alpha emission from a clump consistent with $r_e < 15$ pc within a 100 pc dwarf galaxy. However, due to intergalactic medium (IGM) absorption, Lyα is of limited use as a star formation rate (SFR) or kinematics indicator. Spectroscopic SFRs (e.g., from Hα) are necessary to probe star formation within tens of Myr (i.e., the formation timescales of star clusters), but such observations are largely lacking.

In this work, we undertake a joint HFF and Keck spectroscopic study of sub-structure around the progenitor of a MW mass galaxy. Specifically, we combine K band Keck 1/MOSFIRE spectroscopy with deep HFF photometry, to study an off center (∼100 pc from the galaxy center) $r_e = 40^{+70}_{-30}$ pc, $M_\star \sim 10^{8.2} M_\odot$ clump within a $r_e = 1.1^{+0.1}_{-0.3}$ kpc, MW progenitor mass ($M_\star \sim 10^{9.8} M_\odot$) galaxy at $z = 2.36$, with a magnification of $\mu = 5.21$. We jointly model the photometric SED and Hα to determine the SFH of the host galaxy and clump, assuming scenarios in which the 1:40 mass ratio clump is forming *in-situ* and in which it is being accreted. Our joint analysis of broadband photometry and near-IR spectroscopy illustrates the scientific promise of the data that *Hubble* and the *James Webb Space Telescope* (*JWST*) will provide at most redshifts for studying sub-structure, while also highlighting some of the outstanding challenges that must be addressed to increase our understanding of hierarchical galaxy formation at high-redshifts.

4.2 Methodology

We selected targets for spectroscopic follow-up from the HFF MACS J1149, MACS J0717 and Abel 370 clusters, using the foreground subtracted Shipley et al. (2018) catalogs with coverage in $F275W$, $F336W$, $F435W$, $F606W$, $F814W$, $F105W$, $F125W$, $F140W$, $F160W$, and IRAC/MIPS from *Sptizer*.

Initial sizes for our catalog were derived with an updated version of methodology described in Bouwens et al. (2017a). In short, we mask nearby sources and apply a lensed Sérsic fit for the intrinsic brightness of the source and its size simultaneously using a Markov chain Monte

Parameter	Prior Type	Prior Range
Mass/Metallicity	Gaussian	$7M_\odot$ <M< $12.5M_\odot$/−1.99 <Log(Z)< 0.0
Attenuation (A_v)	top-hat	$0 < A_v < 1.5$
dust index (δ)	top-hat	$-2.0 < \delta < .5$
Gas Log(Z)	top-hat	−1.99 <Gas Log(Z)< 0
Ionization	top-hat	−4 <Log(U)< −1

Table 4.1: Summary of priors used to fit the SED for the whole galaxy. We fit mass and metallicity using a joint prior, based off of the Gallazzi et al. (2005) mass/metallicity relation with artificially inflated scatter to account for redshift effects. We use the Kriek & Conroy (2013) dust parameterization and therefore fit for dust index and A_v. We also include gas parameters in our model. Though we do not expect our observations to constrain these, including them in our model allows us to treat them as nuisance parameters rather than fixing them to set values.

Carlo (MCMC) methodology. As de-lensing an image introduces error and bias depending on the magnification map used, we instead employ a forward modeling approach. Namely, we account for magnification in our models by distorting each pixel by the requisite shear and amplification factors necessary to mimic the effects of lensing. For this to be computationally tractable, we fix the total magnification for our models to the median value from the CATS (Jullo & Kneib 2009; Richard et al. 2014; Jauzac et al. 2015b,a), Bradač et al. (2009), GLAFIC (Oguri 2010; Ishigaki et al. 2015; Kawamata et al. 2016), and Johnson et al. (2014) lensing maps. We discuss the updated size measurement for this source in §4.3.

When possible, we further selected for sources with photometrically inferred high equivalent width in [OIII] or Hα, depending on redshift. This was done by running the spectral energy distribution (SED) fitting code, `FAST` (Kriek et al. 2009, 2018), on our sources and computing the line contamination to the continuum fit from [OIII] or Hα. Specifically, we fit the photometry excluding the band containing the relevant line to measure the stellar continuum. We then convolve the appropriate filter with the best fit SED and used the difference between this continuum value and the measured photometry to infer line contamination in the band. For sources outside the proper redshift range, we instead selected for high SFRs from the SED fit. This SED fit corresponds to the photometry of the full galaxy, and was only used for selecting sources. We discuss the improved SED fit for this source as well as the SED fits for the clump at the end of this section and in §4.4.

The galaxy we highlight in this work is faint by traditional spectroscopic targeting standards ($F160W = 25$, not correcting for magnification). However, it met our selection criteria for a potentially observable emission line. An early variation of our size measurement routine was biased towards detecting clumps rather than extended sources, which serendipitously resulted in this interesting source falling into our sample. We discuss the full spectroscopic sample in a follow up paper.

The spectroscopic Hα detection of this object shown in Figure 4.1 is the result of 6 hours of integration split over two half nights. The reduction was conducted with the `MOSFIRED` pipeline,

$\mu = 5.14$	Full Galaxy	Clump Only (ex-situ)	Clump only (in-situ)
Redshift	2.3695 ± 0.0005	—	—
log(M) [$M_\odot$]	$9.8^{+0.3}_{-0.2}$	$8.2^{+0.3}_{-0.2}$	$8.1^{+0.2}_{-0.1}$
A_v	$0.44^{+0.13}_{-0.12}$	$0.15^{+0.05}_{-0.08}$	$0.37^{+0.08}_{-0.02}$
log(Z)	$-0.22^{+0.30}_{-0.35}$	$-1.35^{+0.75}_{-0.43}$	$-0.18^{+0.16}_{-0.23}$

Table 4.2: Summary of source and clump properties form our PROSPECTOR fits to the photometry from the full galaxy and the clump with ex-situ and in-situ priors

an updated version of the reduction procedure described in Kriek et al. (2015). As the source is entirely unresolved, we use an aperture correction for a point source, using a star observed in one of our MOSFIRE slits. No differential aperture correction was required for flux calibration purposes. We then measure a spectroscopic redshift by fitting a Gaussian to the Hα line and taking the mean and standard deviation of 10,000 realizations perturbed within the noise as our measurement and error respectively.

We measure the velocity dispersion of this source by fitting a Gaussian to the Hα emission line and correcting for the instrument resolution using skylines in the 200Å redwards and bluewards of Hα. We again derive errors through a Monte Carlo method.

To measure a non-parametric SFH for our source, we simultaneously fit our MOSFIRE spectrum, and 12 bands of photometry using the Bayesian spectral fitting code `PROSPECTOR` (Leja et al. 2017; Johnson et al. 2019). To minimize the noise introduced by the lack of continuum detection in our spectrum, we incorporate it into the fit by creating a synthetic narrow band filter over solely Hα and including it as an additional band in our photometric fitting, correcting for magnification effects. For the non-parametric fit, we use 13 age bins which are uniformly logarithmically sampled at early times, with finer resolution in the most recent 1 Gyr. To avoid biasing our SFH with our choice of age bins, we include more bins than our projected resolution on SFH, and apply a continuity prior. Following Leja et al. (2019), we apply a stellar-mass stellar-metallicity prior using a version of the Gallazzi et al. (2005) relation where we have doubled the width of the confidence interval to accommodate any redshift evolution.

We then use the Bayesian nested sampling code `dynesty` to sample the posterior (Speagle 2019). Our most probable parameters are reported in Table 4.3, where errors reflect the 16th and 84th percentiles of the posterior for each parameter, with the uncertainty due to magnification added in quadrature. The magnification uncertainties are modest owing to the small magnification of this source and the geometric constraints afforded by the spectroscopy.

We show the SFH from our `PROSPECTOR` fit in Figure 4.2. We find the star formation is consistent with a rising τ over a period of a Gyr, with a potential underlying older stellar population at earlier times. However, the amplitude of the uncertainties preclude a more detailed interpretation of the older SFH.

We quantify the information added by the Hα measurement by modeling the SED without it. As expected, the net effect is that the inclusion of Hα provides a tighter constraint on star formation

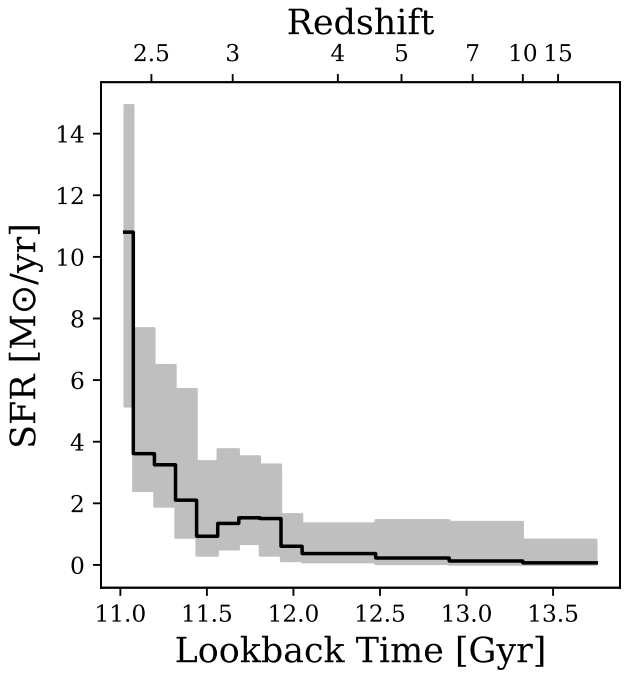

Figure 4.2: SFH from a non-parametric PROSPECTOR fit. We use 13 age bins in our fit with higher time resolution in the most recent 1 Gyr bins. To avoid biasing our SFH with our choice of age bins, we include more bins than our projected resolution on SFH and apply a continuity prior.

within the most recent 50 Myr, compared to an SED-only fit. Star formation at early times is also modestly more constrained (i.e, the probability distribution function corresponding to bins beyond 1.5 Gyr is narrower) when our Hα measurement is included.

4.3 Size Measurements

With a redshift in hand, we are able to improve our estimate of the clump's size. To do this, we fix our models to the spectroscopic redshift of the source. This constraint allows us to measure a more precise magnification, decreasing the original size measured for this object by 5% over the photometric redshift derived size.

To measure the size of the source we began with an unconstrained Sérsic profile and found that we could not simultaneously fit both the diffuse light component and the clump for any Sérsic index from 1-4. In an attempt to constrain both components simultaneously, we tested an exponential disk + Sérsic model, an Sérsic model + gaussian model, and an exponential disk with a flux-scaled PSF. We find that the latter results in the best residuals by far for all HFF bands, indicating that the clump is essentially unresolved. A conservative upper limit on the size of the clump is therefore

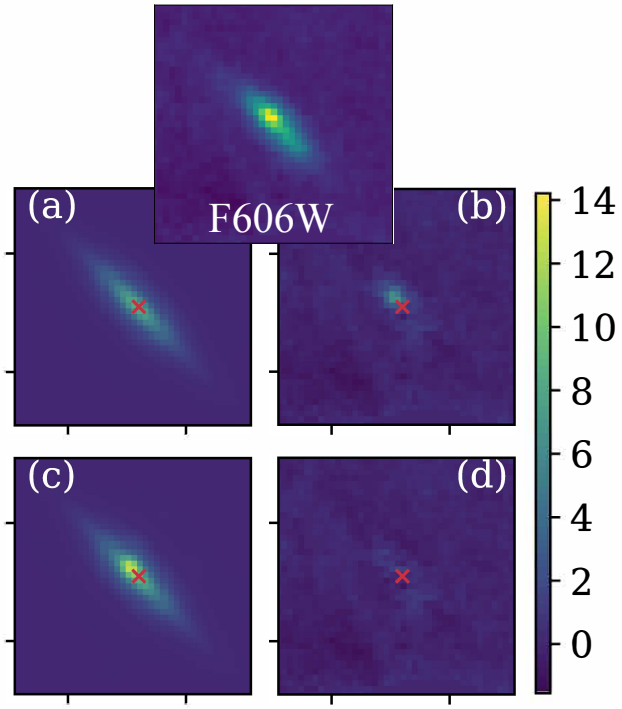

Figure 4.3: Example of size measurement procedure for $F606W$ image. **(a):** Best fit Sérsic $n = 1$ model. **(b):** The residual for the n=1 sérsic model with an x demarcating the center of the galaxy accounting for shear. The projected distance from the clump to the center of the source is $\sim$ 100pc. **(c):** Best fit Gaussian + Sérsic $n = 1$ model. **(d):** Residuals for the Gaussian + Sérsic $n = 1$ model. It is apparent from the last panel that there is an off center clump in the galaxy.

the size of the PSF itself, which is 108pc in F606W.

For a more detailed estimate of the clump size, we fix the Sérsic profile of the galaxy and simultaneously compute the residuals for a grid of model parameters for a Gaussian clump (size and brightness). We considered values of $r \approx 0.02$ pixels to $r = 0.5$ pixels for the radius of the Gaussian component. The resulting probability distribution allowed us to constrain the maximum likelihood size of the clump to $r_e = 40^{+70}_{-30}$pc in F606W.

Using these model derived parameters, we compare to the background subtracted image within $1''$ aperture, and find the 16 σ detection shown in panel (b) of Figure 4.3. We measure the projected distance of the clump from the center of the Sérsic fit to the diffuse component to be 100^{+70}_{-30} pc. As the center of the Sérsic fit to the diffuse component is well-constrained, magnification uncertainties dominate our reported uncertainties. This galaxy appears edge-on due to lensing shear, we therefore assume a typical inclination of 45° to estimate the true distance (d) of the clump to be 140 pc. Comparing this to the effective radius (R_e) of the galaxy results in a $d/R_e \sim 0.1$.

A caveat to measuring size in bluer bands is that they are biased towards more recent star

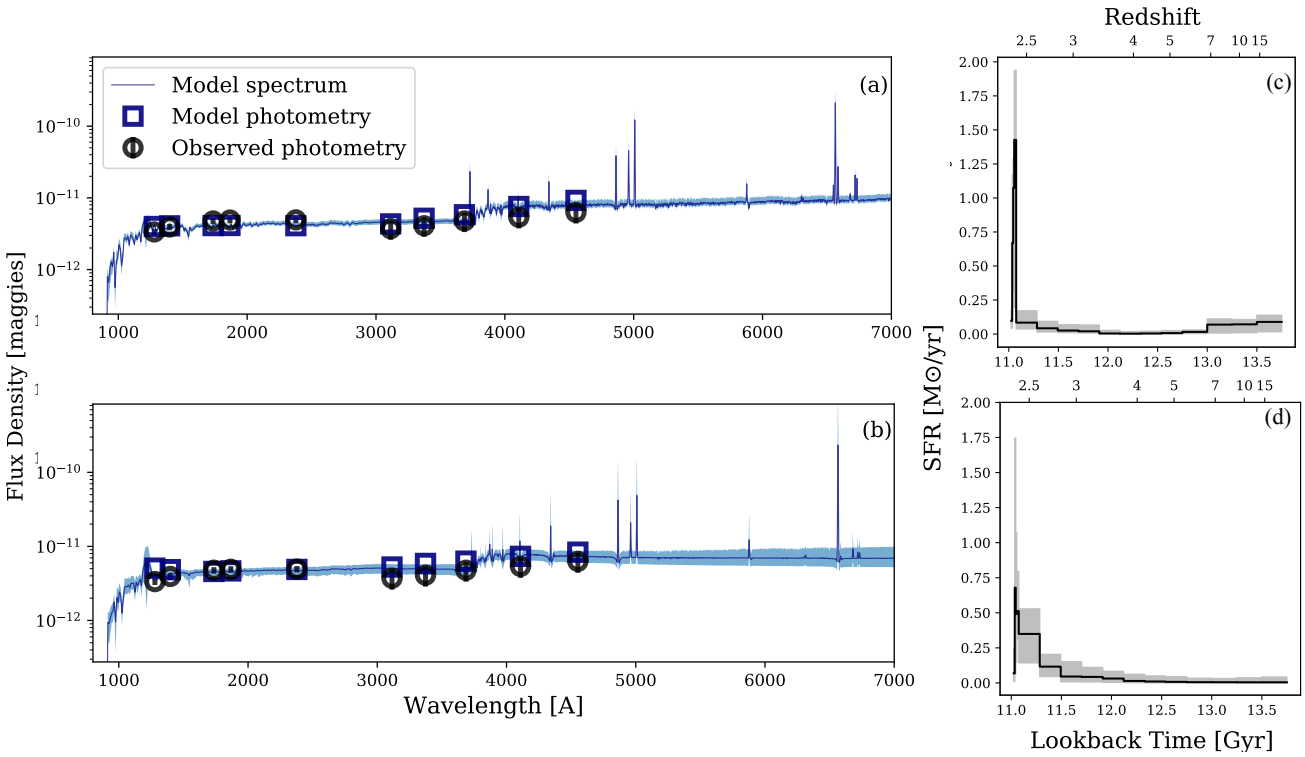

Figure 4.4: The SED fits and SFH for the model extracted clump photometry. **(a):** The SED fit corresponding to the *in-situ* event priors, with the 16th and 84th percentile models shown in light blue. **(b):** The SED fit to the accretion formation scenario priors, plotted with the same conventions as panel (a). **(c):** The SFH corresponding to the *in-situ* scenario. The grey show the 16th and 84th percentiles and the black line shown the median model. **(d):** The SFH corresponding to the accretion scenario plotted with the same conventions as panel (c). The accretion scenario is a slightly better fit to the data according to the smaller residuals and higher Bayesian evidence criteria. The SFHs resulting from both sets of priors indicate an extremely young stellar population. The burst of the accretion scenario seems to line up with the highest star formation rates in the host galaxy, however, as our first SFH bin corresponds to 50Myr (in concordance with the fit to the host-galaxy), the difference in this small time bin is likely not well constrained by either model.

formation (e.g., Stark 2016b). Though we do not expect substantial color gradients in a galaxy of this mass, we asses the robustness of our measured clump by comparing the *maximum a posteriori* value of the MCMC fit for the clump as measured from the $F160W$ to $F606W$ bands. For this clump, the size changes by the resolution difference between $F606W$ and $F160W$. Thus, this source appears more compact in bluer bands primarily due to its point source like nature, rather than bias towards younger populations. As higher redshift studies are limited to probing similarly blue restframe wavelengths in determining sizes, our measured clump size can be directly compared.

4.4 Modeling the SED for In-Situ vs. Accretion Scenarios

There are two primary mechanisms that can explain the presence of a 1:40 mass ratio for a clump in a proto-MW galaxy; 1: *in-situ* formation due to disk turbulence and gravitational collapse, 2: star formation triggered by an accretion event with a neighboring satellite, which may be analogous to the accretion of an Small Magellanic Cloud progenitor and a MW progenitor at $z \sim 2$ (Weisz et al. 2013). While the spatial resolution necessary to extract the dynamical information to distinguish these two scenarios will likely remain out of reach until the era of 30-meter telescopes, we can gain some insight as to the likelihood of each scenario by combining spectral and photometric fitting with informed priors.

In the case of *in-situ* disk fragmentation, we expect the metallicity parameters, stellar and nebular, to be similar to the host galaxy parameters. Though the SFH of the clump may differ (possibly dramatically) from the host galaxy, the fact that it is forming out of the galaxy's cold gas supply implies the metallicity of the clump should be similar to that of its host. To model this scenario, we take the metallicity prior on the clump to be within the 16-84th percentiles of the posterior distribution to the metallicity of the galaxy itself. We leave all other parameters as shown in § 4.2. We assume that though the metallicity of the clump and host galaxy may vary, the metallicity of an *in-situ* clump should not be outside the host galaxy's metallicity range. We then compare this to a 'free' fit to the clump, where the priors are described in § 4.2, with the exception of the mass-metallicity prior, which does not apply at such low masses. We therefore instead use separate flat mass and metallicity priors but leave their ranges as shown in § 4.2. The resulting SED fits for the two sets of priors are shown in panels (a) and (b) of Figure 4.4, where the former corresponds to an accretion event and the latter to $in-situ$ formation.

We find that the model with *ex-situ* priors yields smaller residuals than the *in-situ* priors. However, the Bayesian evidence criteria is of order unity which does not signify a robust difference between the two sets of priors. We further show the corresponding SFH for each set of priors in panels (c) and (d). Though these appear qualitatively different, they both essentially correspond to an extremely young stellar population. We discuss future prospects for this archaeological approach to characterizing sub-structure in §4.5.

4.5 Discussion

In this section, we explore several plausible clump formation scenarios given the analysis presented in the previous sections. We attempt to identify features that may allow us to discriminate between accretion and *in-situ* formation mechanisms and discuss how future observations and targeted theoretical studies will improve our ability to cleanly associate observed sub-structure with a formation scenario.

First, we consider the case that this clump formed *in-situ* via turbulence induced disk fragmentation (e.g., Dekel et al. 2009, 2013). Cosmological zoom-in simulations have characterized such clumps to have baryonic masses up to 10^9 $M_\odot$ and radii up to 1 kpc. Typical clumps with a baryonic mass corresponding to our measured stellar mass have characteristic radii of $\sim$ 250pc (Oklopčić et al. 2017; Mandelker et al. 2017). However, as we are limited to measuring stellar mass (we have no gas measurement), our observed clump likely corresponds to a larger baryonic mass in simulations and therefore a larger R_e ($\sim$ 500 pc). The mass surface density we measure for the clump is above 10^3 $M_\odot$ pc^{-2}, which is denser than simulated clumps. Non-cosmological, hydrodynamic simulations described in Tamburello et al. (2015, 2017) do examine the stellar mass and radii of clumps directly as a function of resolution. We find good agreement with our clump mass and radii when comparing to their high-resolution (100 pc) mock-observations.

We can also compare the mass fraction of the clump within the galaxy to simulations. Mandelker et al. (2014) find that *ex-situ* clumps have a characteristically higher mass fraction than *in-situ* ones. Comparing to their updated cosmological zoom-in simulations including feedback, we find that our 1:40 mass ratio is on the very massive end of their clump to host mass ratio distribution (Mandelker et al. 2017).

The location of our clump, so near the center of its host, remains atypical for clumps formed *in-situ*. Both theoretical (Oklopčić et al. 2017; Mandelker et al. 2017) and observational (Guo et al. 2012; Shibuya et al. 2016) studies of clump formation find clumps as blue and young as the one we observe further out than $d/R_e \sim 0.1$. The d/R_e value we infer is smaller than the bulk of simulated clumps, but approaches the distance ratio seen in simulations for clumps older than our measured age (e.g., 1 Gyr in Mandelker et al. 2017) Finally, disk fragmentation in simulations ubiquitously leads to the formation of multiple clumps (Mandelker et al. 2014, 2017) and though we have sub-kpc resolution for the entire galaxy, we only identify one. While, it is possible that there are other clumps that remain obscured due to projection effects, it would require an unlikely geometry to hide all of them from discovery in our data. Given that this clump is detected at 16σ, it is unlikely that we are missing similarly massive clumps due to surface brightness limits.

A second *in-situ* formation scenario is that this clump is not a single star-forming entity, but instead an unresolved blend of multiple smaller star clusters. We gain some insight into this possibility by comparing our clump to resolved extreme star-forming regions in the local Universe. For example, the central star-forming cluster of 30 Doradus, NGC 2070, is commonly referred to as an analog for high-redshift star cluster formation (Leroy et al. 2018; Ochsendorf et al. 2017). Integrating the mass of all clusters in a 200 pc region centered on NGC 2070 yields a total stellar mass of $M_\star \sim 10^5$ $M_\odot$ (Cignoni et al. 2015), which is 1000 times less massive than our clump. This is perhaps not surprising given the differences in the host galaxy properties and relative star-forming

conditions in the low- and high-redshift Universe. Nevertheless, it does illustrate just how massive a star-forming region our clump may be.

Perhaps a more apt comparison is to the the merging Antennae system. The Antennae yields gas pressures analogous to those expected in high-redshift star formation (e.g. Cabrera-Ziri et al. 2016). Integrating the stellar mass for the three most massive clusters in the Antennae yields a mass of $M_\star \sim 10^6$ $M_\odot$ (Johnson et al. 2015). Even assuming the 84th percentile radius for our clump, we would require a mass contamination from the host to be factor of 10 larger than inferred from high-resolution simulations (Tamburello et al. 2017) or nearby Young Molecular Clouds (Hollyhead et al. 2015). Given our high spatial resolution and model extracted photometry, we do not expect anywhere near as severe of a mass contamination. It is therefore unlikely that our clump is a set of very tightly packed massive star clusters.

A third possibility is that an off-center star forming clump may be an indication of an ongoing merger, or pristine-gas accretion event (e.g., Hopkins et al. 2012; D'Souza & Bell 2018). A comparison of the SFH we infer for the observed clump in Figure 4.3 to the SFH of the main galaxy in Figure 4.2, shows an extremely young stellar population whose formation corresponds to a peak in star formation in the main galaxy. This concurrence can be interpreted as consistent with an *in-situ* formation scenario or a gas accretion scenario over an accretion event.

However, though both sets of model priors we used for the clump result in a fit consistent with a single burst of star formation, our *ex-situ* priors yield a fit that allows for a more extended ($\sim$ 1 Gyr) clump SFH. Furthermore, it is difficult to compare our results to the literature on mergers as the redshift and mass range of our source has not been explored at similar resolutions. Morphological criteria, such as $Gini - M_{20}$ (Lotz et al. 2004) or concentration and asymmetry (Conselice et al. 2014) have primarily been used at lower redshifts (Lotz et al. 2011) or higher stellar masses (Man et al. 2016). Recent work by Nevin et al. (2019), uses linear decomposition of non-parametric morphological criteria in simulations to find an optimal merger identifying criteria. While work in this vein is promising, it is unclear how well these criteria hold up at higher redshift (Thompson et al. 2015). Current criteria for mergers are categorically less sensitive to minor mergers (1:4-1:10 stellar mass ratios) and are insensitive to mergers with larger mass disparity. This means that a MW-Large Magellanic Cloud merger, for example, would likely not be identified with current criteria and a MW-Sagittarius merger would be completely undetectable. With more work in lensed fields, where sub-structure resolution to sub $\sim$ 100 pc is possible, studying such minor mergers should be within reach.

Though we cannot conclusively determine the nature of this off-center star forming clump from our current data set, there are promising paths forward. For example, a larger sample of galaxies and wider spectral coverage with the *JWST*, could enable the modeling technique presented in this work. A statistical approach targeting similarly low magnification sources ($\mu < 10$) would allow us to disentangle line-of-site effects that limit our comparisons to simulations (i.e., number of clumps per source). Current explorations of clumps in the HFF generally require observations to approach surface brightness detection limits, with the sensitivity of NIRCAM, it should be possible to detect more clumps than observed in current HFF observations. Likewise, the spectral range, sensitivity and angular resolution of NIRSPEC will allow more efficient spectral analysis of clumps out to higher redshifts, than available with current ground based instruments.

Current estimates using the *JWST/NIRSPEC* exposure time calculator, show that Hα, Hβ, and [O iii] can be detected with $S/N > 5$, in under two hours for this galaxy, with faint lines like [O iii](4363 Å) detected in 5 hours. Such faint lines are easier to measure in more magnified and extreme star forming sources, such as the $z = 2.69$, $\mu \sim 8$, dwarf galaxy identified in Gburek et al. (2019), for which *JWST/NIRSPEC* would detect [O iii](4363Å) with $S/N > 5$ in under an hour of exposure time. These lines enable robust dust attenuation measurement and vastly improved constraints on metallicity. These can be used in conjunction with simulations to elucidate the origin of clumps. Furthermore, the multiplexing abilities of *JWST/NIRSPEC* combined with the resolving power afforded by even modestly lensed fields, enable a statistical approach to characterizing clumps in lower mass and higher redshift systems than currently feasible.

4.6 Conclusions

We are entering an era of increased sensitivity that enables us to study substructure at $z > 2$ on ever smaller spatial and mass scales. Our current MOSFIRE study previews the potential of spectroscopy to connect substructure and star formation history, as well as the challenges in interpreting even high spatial resolution photometry.

In this work, we present a combined spectral and photometric analysis of a lensed, $\mu = 5.14$, MW-mass progenitor galaxy at $z = 2.36$ with an off-center star forming clump. We have used precise redshifts to measure robust sizes for the clump and the main galaxy. Finally, we investigate the origin of the clump by leveraging our measurement of the main galaxy to inform priors on the fit to the clump. We find:

- A Log($M_\star$)= 8.2^{+3}_{-2} $M_\odot$ clump with $r_e = 40^{+70}_{-30}$ pc located $\sim$ 100pc away from the galaxy center. We find that the host galaxy has a mass of Log($M_\star$)= $9.8^{+0.3}_{0.2}$ $M_\odot$.
- Comparing our inferred clump/galaxy masses, SFRs and sizes to low-redshift analogs and simulations, we find that this clump is unlikely to be an aggregate of multiple less massive clumps. Given our measured stellar mass surface density of order 10^3 $M_\odot pc^{-2}$, we conclude that if this clump formed *in-situ*, it is one of the densest star forming regions confirmed to date. If the clump formed *ex-situ*, this system is undergoing a 1 : 40 mass ratio merger.
- With the advent of *JWST NIRCAM and NIRSPEC*, we find that this analysis can be reasonably undertaken statistically. The sensitivity and broadband capabilities of *NIRSPEC* will allow measurement of important dust and metallicity indicators. While its angular resolution will allow a more robust comparison between clump and galaxy properties that can be used to infer clump origins.

4.7 SED fits and inferred SFH with varying stellar models

There is currently no standard universally excepted stellar modeling framework in the galaxies literature, potentially leading to systematic offsets in inferred properties across different studies.

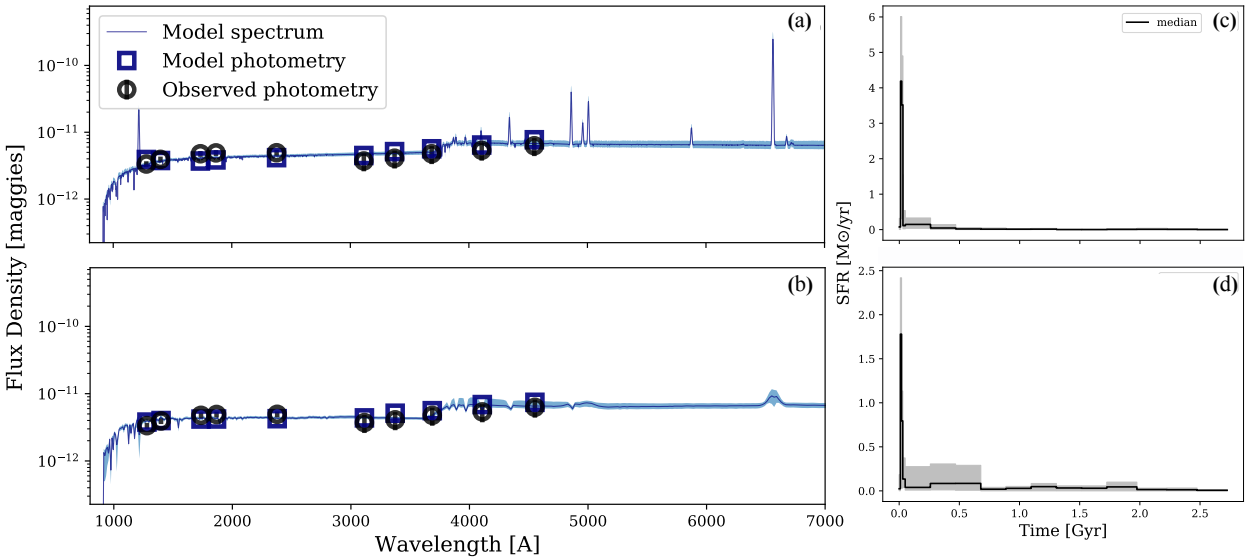

Figure 4.5: The SED fits and SFH for the model extracted clump photometry with alternate stellar libraries. In all plots the shaded regions correspond to the 16th and 84th percentiles. (a): SED fit using the BPASS models with binaries. (b): SED fit using BC03 models. (c) SFH corresponding to BPASS model fit. (d) SFH corresponding to the BC03 models. Both models show a more peaked median clump SFH, however all models are consistent with a young star forming burst.

We investigate alternate isochrone and spectral libraries and their impact on our analysis. We examine both the BPASS models with binaries, as well as the popular BC03 which we replicate by combining the BASEL spectral libraries with the Geneva isochrones. We show the results of our PROSPECTOR fits in Figure 4.5. We find that both BPASS and BC03 produce a more peaked median SFH than the MIST models (see Figure 4.4). However an extremely young burst of star formation is favored by all three models.

4.8 Intrinsic Magnitudes Measured for the Galaxy and Clump

Filter	Full Galaxy	Clump
F336w	$26.67^{+0.35}_{-0.14}$	$28.99^{+1.51}_{-2.50}$
F435w	$25.63^{+0.33}_{-0.05}$	$28.81^{+0.67}_{-1.65}$
F475w	$25.46^{+0.33}_{-0.05}$	$28.63^{+0.52}_{-1.50}$
F606w	$25.21^{+0.33}_{-0.04}$	$28.33^{+0.41}_{-1.39}$
F625w	$25.28^{+0.33}_{-0.08}$	$28.34^{+0.49}_{-2.78}$
F814w	$25.15^{+0.33}_{-0.04}$	$28.35^{+0.49}_{-1.45}$
F105w	$25.152^{+0.33}_{-0.04}$	$28.41^{+0.45}_{-1.48}$
F110w	$24.94^{+0.33}_{-0.05}$	$28.56^{0.40}_{-4.38}$
F125w	$24.78^{+0.33}_{-0.04}$	$28.05^{+0.41}_{-1.39}$
F140w	$24.60^{+0.33}_{-0.04}$	$27.98^{+0.38}_{1.36}$
F160w	$24.35^{+0.33}_{-0.04}$	$27.95^{+0.43}_{-1.41}$
irac2	$23.68^{+0.33}_{-0.06}$	—
irac3	$23.63^{+0.76}_{-0.68}$	—

Table 4.3: Measured intrinsic magnitude for the full galaxy and the clump. The uncertainties on the clump flux are from the model fit and represent the 16th and 84th percentiles of the posterior with the uncertainty in magnification added in quadrature. The uneven uncertainties are due to magnification uncertainties.

Chapter 5

Bursty Star Formation in Low Mass Galaxies at Cosmic High Noon

5.1 Introduction

Our picture of the relationship between star formation, mass, and morphology during the peak of cosmic star formation, implies an underlying quasi-static equilibrium in which star formation is regulated by feedback and accretion (Daddi et al. 2007; Whitaker et al. 2012; Shibuya et al. 2015; Tacchella et al. 2016). Though a galaxy may go into a starburst phase, such that its estimated depletion time given its measured SFR is <100Myr (Rodighiero et al. 2011; Atek et al. 2011, 2014), evidence from the scatter of the star forming main sequence indicates that on timescales of $\sim$ 100 Myr, star formation proceeds as a gradual, rather than bursty process out to at least $z = 3$ (Kurczynski et al. 2016).

Low mass galaxies, which are far more ubiquitous, yet challenging to observe past $z > 1$, have shallower potentials and are expected to exhibit star formation variability on shorter timescales than their $M_* > 10$ counterparts (El-Badry et al. 2016; Sparre et al. 2017; Faucher-Giguère 2018). One valuable way to probe stellar feedback and the recent star formation of these systems is to compare $L_{H\alpha}$, a near instantaneous star formation indicator and L_{UV}, a probe of average star formation rate over a $\sim$ 100Myr period. For a consistent star formation prescription, they should agree given constant star formation (Kennicutt 1998).

Locally, the ratio of these two SFR indicators has deviated from unity in low mass ($M_* < 10^7$) dwarf galaxies (Meurer et al. 2009; Lee et al. 2009; Weisz et al. 2012; Emami et al. 2019). This has generally been agreed upon as evidence for rapidly varying star formation. Evidence for bursty star formation in low mass galaxies has been found to extend out to slightly higher mass galaxies to $z \sim 1$ (Guo et al. 2016b; Broussard et al. 2019). Pioneering work at $z \sim 4$ motivates that yet higher mass $\sim 10^{9.7}$ galaxies, may exhibit star formation volatility on timescales comparable to low mass local dwarfs (Smit et al. 2016; Faisst et al. 2019). At cosmic noon however, studies probing this mass range have found results consistent with constant star formation (Erb et al. 2006a; Förster Schreiber et al. 2009; Wuyts et al. 2011; Shivaei et al. 2015). Though there is some observational

(Shivaei et al. 2015; Mehta et al. 2017) and theoretical (Sparre et al. 2017; Faucher-Giguère 2018; Tacchella et al. 2019) motivation for physical deviation below $M_\star = 10^{10} M_\odot$, the sensitivity of current instruments has thus far only allowed follow up of the most extreme star forming low mass galaxies past $z = 1.5$ (Maseda et al. 2014).

Gravitational lensing and the Hubble Ultra Deep Field (HFF) offers a promising way forward towards observing the faint, low mass Universe at cosmic high noon. HFF studies have uncovered sources with intrinsic luminosities as faint as $M_{\rm UV} = -14$ at z~3 and allowed spatial resolution down to 10pc at $z < 1$ (Kawamata et al. 2015b; Bouwens et al. 2017c; Kawamata et al. 2017; Vanzella et al. 2017). Interestingly, these faint galaxies seem to be systematically compact at $z = 2 - 8$ (Bouwens et al. 2017a) even accounting for surface brightness.

The OLAS survey has recently harnessed the power of gravitational lensing to gain insight into feedback in low mass galaxies at $z = 1.5 - 2$ (Hirtenstein et al. 2019). They used integral field unit (IFU) spectroscopy on OSIRIS/Keck with adaptive optics, to study the kinematics of these galaxies and found evidence to support stellar feedback driven fluctuation in their potential, which if confirmed would have important implications for dark matter profile in local dwarf galaxies. The combination of size, robust photometry, and spectroscopy derived SFR and kinematics is necessary to continue shedding light on this ubiqioutous yet poorly understood mass range at the peak of cosmic star formation.

In this work, we undertake a joint HFF and Keck spectroscopic study of low mass, compact, galaxies at intermediate redshift. Specifically, we combine deep HFF photometry with rest-frame optical spectroscopy obtained with the Keck 1/MOSFIRE near-infrared spectrometer, to elucidate the star formation histories and kinematics of 33 lensed galaxies at 1.8<z<3.3, with masses and sizes ranging from $7 \leq log(M) \leq 10.2$ and $0.04kpc \leq r_e \leq 1.2kpc$, respectively. We jointly model the photometric SED and rest-frame optical emission lines of our galaxies to infer robust masses and dust extinctions and combine these with measured L_{UV} and $L_{H\alpha}$ examine the recent SFHs of our sources. We further measure the velocity dispersion and dynamical masses for each object to constrain kinematics and test theoretical models of feedback in low mass galaxies. Our joint analysis of broadband photometry and near-IR spectroscopy illustrates the scientific promise of the data that *Hubble* and the *James Webb Space Telescope* (*JWST*) will provide at most redshifts for studying faint, compact sources, while also highlighting some of the outstanding challenges that must be addressed to increase our understanding of the faint high-redshift Universe.

5.2 Methodology

5.2.1 Target Selection

We selected targets for spectroscopic follow-up from the HFF MACS J1149, MACS J0717 and Abel 370 clusters, using the foreground subtracted Shipley et al. (2018) catalogs with coverage in $F275W$, $F336W$, $F435W$, $F606W$, $F814W$, $F105W$, $F125W$, $F140W$, $F160W$, and IRAC/MIPS from *Sptizer*. Of our 38 targeted galaxies, 23 were mass selected and and ten were size selected across our redshift range. For targeted Hα, 13 of our sources were mass selected and the remaining

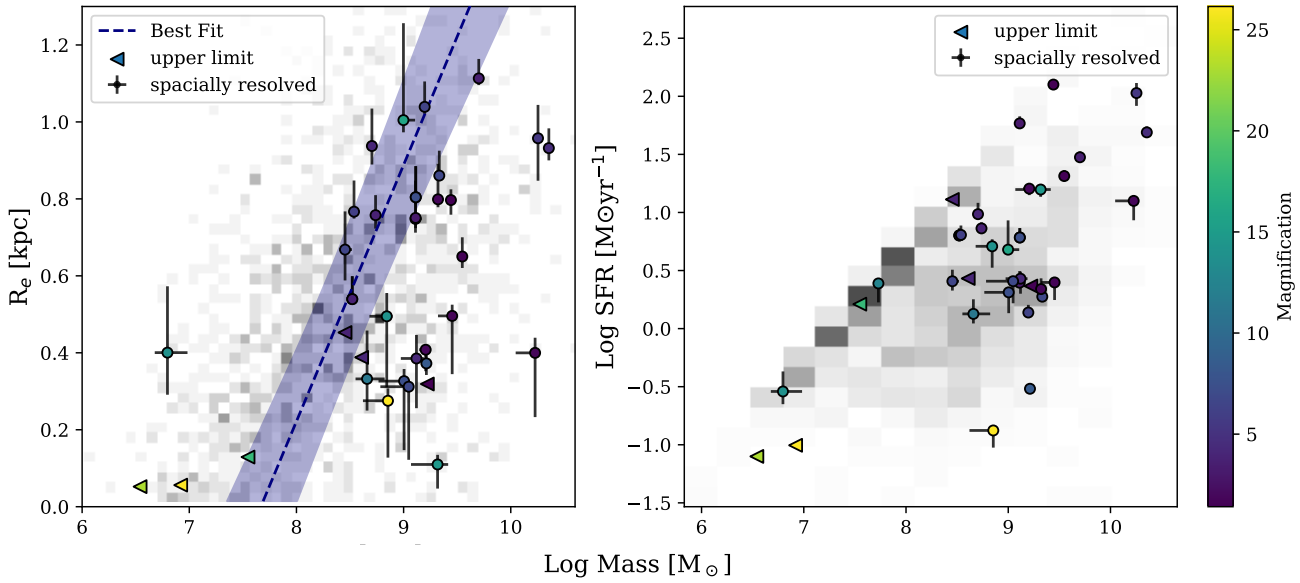

Figure 5.1: **Left:** The mass-size relation for lensed dwarf galaxies at $z = 1.8 - 3.2$. The grey points are from a larger analysis by Ribeiro et al. (*in-prep*). The spectroscopically confirmed galaxies are shown either as circles (spatially resolved) or triangles (upper limits) and color coded by magnification. The dotted-line is our best fit to the mass-size relation of the full photometric sample, while the shaded region corresponds to the respective 16^{th} and 84^{th} percentiles. **Right:** The stellar mass-SFR relation. The full photometric sample is shown in grey while the circles (spatially resolved) and triangles (upper limits), represent spectroscopically confirmed sources. Followed-up sources are color-coded by maginfication. Our spectroscopic sample tracks the broader photometric sample in both mass-size and mass-SFR, so is not obviously biased relative to the low-mass galaxies from the entire sample.

four were size and line width selected through the following procedure. The heterogeneous selection is the result of data scarcity in this low-mass regime at high-redshift. Accordingly, this study emphasizes what can be learned from the system at hand and does not explore broad population level effects.

Initial sizes for our catalog were derived with an updated version of methodology described in Bouwens et al. (2017a). In short, we mask nearby sources and apply a lensed Sérsic fit for the intrinsic brightness of the source and its size simultaneously using a Markov chain Monte Carlo (MCMC) methodology. As de-lensing an image introduces error and bias depending on the magnification map used, we instead employ a forward modeling approach. Namely, we account for magnification in our models by distorting each pixel by the requisite shear and amplification factors necessary to mimic the effects of lensing. For this to be computationally tractable, we fix the total magnification for our models to the median value from the CATS (Jullo & Kneib 2009; Richard et al. 2014; Jauzac et al. 2015b,a), Bradač et al. (2009), GLAFIC (Oguri 2010; Ishigaki

et al. 2015; Kawamata et al. 2016), and Johnson et al. (2014) lensing maps. With our measured redshift, we extract a more revised size measurement for each of our spectroscopically confirmed sources as described in subsubsection 5.2.2.3.

For the four sources that were not mass selected, we further selected for sources with photometrically inferred high equivalent width in [OIII] or Hα, depending on redshift. This was done by running the spectral energy distribution (SED) fitting code, `FAST` (Kriek et al. 2009, 2018), on our sources and computing the line contamination to the continuum fit from [OIII] or Hα. Specifically, we fit the photometry excluding the band containing the relevant line to measure the stellar continuum. We then convolve the appropriate filter with the best fit SED and used the difference between this continuum value and the measured photometry to infer line contamination in the band. For sources outside the requisite redshift range, we instead selected for high SFRs from the SED fit. This SED fit corresponds to the photometry of the full galaxy, and was only used for selecting sources.

With the spectroscopic redshifts in hand, we undertake SED fitting assuming non-parametric star formation histories (SFHs) using `PROSPECTOR` (Leja et al. 2017; Johnson et al. 2019), following the procedure described in Zick et al. (2020). For the current paper, we simply use the stellar masses and $E(B-V)$ excess measurements, and will discuss insights related to the SFHs in future work.

5.2.2 Deriving Spectroscopic Parameters

The spectroscopic reduction was conducted with the `MOSFIRED` pipeline, an updated version of the reduction procedure described in Kriek et al. (2015). We then measure a spectroscopic redshift by fitting Gaussians to a combination of the Hα, the [O iii] doublet, and Hβ lines (depending on which are present), assuming fixed widths where appropriate. We take the mean and standard deviation of 10,000 realizations perturbed within the spectroscopic noise as our redshift measurement and error respectively. We now describe how we measure other physical parameters from our spectroscopy.

5.2.2.1 Velocity Dispersion

We measure an integrated velocity dispersion (σ) from the extracted 1d spectra. We use either the Hα emission line ($z < 2.6$) or the [O iii] emission lines ($z > 2.6$) for galaxies with line detections greater than 3σ. These criteria provide for a total sample of 33 galaxies. We correct our σ measurements for line broadening due to instrumental resolution using skylines in the 200Å immediately to the red and blue of Hα([O iii]). We determine errors on σ through a Monte Carlo method, similar to that used for redshift measurements. As many of our sources are unresolved, we expect slit misalgnment to contribute to our measurement uncertainty, which may bias us towards artificially low velocity dispersion measurements for some sources. Because these are high redshift sources, most of which likely lack an established axis of rotation, we expect that slit-misalignment will, at most, only moderately affect our measurements.

5.2.2.2 Hα and UV Luminosities

For the 17 sources in our sample that have Hα detections, we measure the Hα luminosity ($L_{H\alpha}$) and Hβ luminosity (where possible), by perturbing each line according to its corresponding noise spectrum 10,000 times and fitting a Gaussian function to each line profile. We then take the mean and standard deviation as our measurement and uncertainty, respectively. We apply an aperture correction to flux calibrate our sources, by (i) using the spectrum from our MOSFIRE slitstar and (ii) comparing it to the total expected photometric flux in the relevant filter (Skelton et al. 2014). For our spectroscopically resolved sources, we apply an additional slit-loss correction as described in Kriek et al. (2015). We correct for dust attenuation as inferred from the Balmer decrement (Hβ/Hα), assuming a Calzetti et al. (2000) extinction curve.

For the 4 sources which have no Hβ, we use $E(B-V)$ from our SED modeling to correct for dust. One drawback of this correction is that our SED-based $E(B-V)$ show modest correlations with the model inferred stellar mass. To check whether this significantly biases the resulting star formation measurement, we compare the Hα derived SFRs for our Balmer decrement corrected sources to a SED derived $E(B-V)$ corrected measurements, and find negligible differences, particularly when compared to the magnification uncertainties. We further correct for underlying Balmer absorption features measured from our SED modeling. Finally, we account for the additional uncertainty due to magnification and spectroscopic slit-loss correction (for our spectroscopically resolved sources) by adding these to our final uncertainties in quadrature.

We correct L_{UV} for extinction using the SED derived $E(B-V)$ color excess, and assuming a Calzetti et al. (2000) relation, the prescription found to garner the best agreement between Hα and UV inferred SFRs as described in Shivaei et al. (2015).

5.2.2.3 Revised Size Measurements

We are able to improve our initial estimate of source size by fixing our models to the spectroscopic redshift of the source. The spectroscopic redshift allows for a more precise handle on magnification, especially for sources near a critical line, where small changes in distance can drastically change magnification. In turn, improved knowledge of the magnifications leads to more robust sizes.

To measure the size of each spectroscopically confirmed source, we first determine whether it is resolved. To do this we try two model fits, one is a Sérsic model with a free index (n), the other is a flux-scaled PSF. If the former results in the best fit, the source is photometrically resolved and we use the inferred size from the model fit. If the latter results in the best fit, the source is essentially unresolved. We therefore use the size of the PSF given the source magnification, as a conservative upper limit on the size.

For a more robust size estimate of an unresolved source, we assume they have Gaussian profiles (size and brightness) and compute the residuals over a grid of models. Specifically, we vary the radius of the Gaussian from $r \sim 0.02$ to 0.5 pixels. The resulting probability distribution allows us to estimate the size of the unresolved source, as well as infer a lower limit.

5.3 Results

We now explore several relationships between size, velocity dispersion, and Hα and UV luminosities for our sample of compact, low-mass galaxies at $z \sim 2$.

5.3.1 Bursty Star Formation across Cosmic Time

The Hα and UV luminosities are commonly used tracers of recent star formation in galaxies at virtually all redshifts (Kennicutt 1998; Madau & Dickinson 2014). Hα is produced through recombination in the ionization bubbles created by O-type stars over timescales of $\sim$ 10 Myr. Meanwhile non-ionizing UV photospheric emission from stars with $M \geq 3M\odot$, traces star formation over timescales of $\sim$ 100 Myr. When combined, these tracers can provide a handle on patterns of very recent star formation in a galaxy.

5.3.1.1 Comparison of Hα and UV SFRs

We begin by comparing the Hα and UV SFRs among our sample and against other samples in the local and high-redshift Universe. For consistency with the literature, we adopt the Kennicutt (1998) luminosity-to-SFR relation corrected for a Chabrier IMF (Chabrier 2003).

In Figure 5.2, we plot our inferred SFRs color-coded by radius. Though they trace star formation for two different stellar populations and timescales (O-stars and $\sim$ 10 Myr for Hα and B-stars and $\sim$ 100 Myr for UV), their ratios should be unity under the assumption of a constant SFH, universal IMF, self-consistent dust corrections, and case-B recombination in the case of Hα(Kennicutt 1998). This fiducial scenario is indicated by the dashed one-to-one line. Deviations from a ratio of unity imply that one of these assumptions does not hold.

As Figure 5.2 shows, for our sample of galaxies, there are clear deviations from a ratio of unity. The Hα SFRs are up to a factor 10 larger than the UV-based SFR. Moreover, at fixed $\mathrm{SFR}_{UV}<$ 10 [$\mathrm{M}_\odot$ yr^{-1}], we find a scatter in $\mathrm{SFR}_{\mathrm{H}\alpha}$ of 0.45 dec, which halves for $\mathrm{SFR}_{UV}>$ 10 [$\mathrm{M}_\odot$ yr^{-1}]. Similarly, at fixed $\mathrm{SFR}_{\mathrm{H}\alpha}<$ 10 [$\mathrm{M}_\odot$ yr^{-1}], we find a scatter in UV SFRs of 0.38 dex, which decreases to 0.02 dex for $\mathrm{SFR}_{\mathrm{H}\alpha}>$ 10 [$\mathrm{M}_\odot$ yr^{-1}]. The reduction of scatter and trend toward a one-to-one relationships as a function of increasing stellar mass and/or SFR is consistent with findings from other high-redshift studies (Erb et al. 2006a; Reddy et al. 2012a; Shivaei et al. 2015). We illustrate agreement with the literature by including the results from Shivaei et al. (2015) as red points in Figure 5.2.

Hα and UV SFR indicators have been heavily studied in the Local Volume (LV) at $z \sim 0$ providing another point of comparison (Lee et al. 2009; Meurer et al. 2009; Weisz et al. 2012). We include the LV galaxies from Lee et al. (2009) as grey points in Figure 5.2. Within the LV sample, typical $L_\star$ galaxies follow the one-to-one relationship. However, SFR ratios less than unity are well-established at low stellar masses and/or SFRs (Lee et al. 2009; Weisz et al. 2012; Emami et al. 2019). There is also evidence of similar deviations at moderate redshifts of $0.4 \leq z \leq 1$ for masses $10^{8.5} < M_* < 10^{10.5}$ (Guo et al. 2016b).

For the LV sample, the disagreement between Hα and UV SFR indicators at low SFRs and/or stellar masses has motivated spirited debate. While some contend that burstiness provides a clear explanation for the LV trends (e.g., Weisz et al. 2012; Guo et al. 2016b; Mehta et al. 2017; Emami et al. 2019), others posit it may be systematic variations in the high-mass stellar IMF (Pflamm-Altenburg et al. 2007; Hoversten & Glazebrook 2008; Pflamm-Altenburg et al. 2009; Meurer et al. 2009), stochasticity in sampling the cluster mass function (Fumagalli et al. 2011; da Silva et al. 2012; Fumagalli et al. 2014), as well as improper dust corrections (Lee et al. 2009).

In the case of our sample, the discrepancies are almost certainly due to bursty star formation. The SFRs are too large for stochastic sampling effects to matter. Similarly, systematic IMF variations either occurs at much lower ('top light') or much higher ('top heavy') SFRs (Davé 2008; Kroupa et al. 2013). Our dust corrections are both modest in amount and primarily based on the 'gold standard' Balmer decrements.

Much of the work contrasting Hα and UV derived SFRs at $z \sim 2$ has assumed a relation of unity between the two indicators and utilized this to infer color excess in nebular versus stellar continuum in $z = 2$ star forming galaxies at $M_* > 10$M$\odot$ (e.g., Förster Schreiber et al. 2009; Wuyts et al. 2011). Yet still others find that this correction results in over predicted Hα (Erb et al. 2006a; Reddy et al. 2012a). We adopt an equal $E(B-V)$ for the stellar and nebular emission with a calzetti dust law (Calzetti et al. 2000) applied to both, which has been consistently shown to yield SFR ratios of unity (Shivaei et al. 2015; Reddy et al. 2015; Shivaei et al. 2017) for large populations of higher mass $z \sim 2$ galaxies. Though we utilize this same dust formula, we find lower SFR_{UV} for most our sources at fixed Hα. We find the greatest deviation from the constant star formation assumption for lower SFRs and masses than probed in past $z \sim 2$ studies, which may help explain the discrepancy between ours and past measurements.

The most plausible explanation for the scatter in Figure 5.2 is that some galaxies in our sample have recently experienced a burst of star formation, leading to elevated Hα relative to the UV. That is, not enough time has elapsed for equilibrium in these flux ratios to be established. Such models of bursty star formation (Weisz et al. 2012; Emami et al. 2019) also predict a population of Hα deficient, but UV bright galaxies, that in the local Universe, should outnumber the bursting systems due to the relative timescales traced by Hα and UV. Higher gas accretion rates imply these systems may not comprise the majority of low mass galaxies at high redshift (Caplar & Tacchella 2019). However, the lack of $\mathrm{SFR}_{\mathrm{H}\alpha}/\mathrm{SFR}_{UV} < 1$ galaxies is likely due to our associated $L_{H\alpha}$ MOSFIRE detection limit, which is roughly $\sim 10^{42}$ erg s^{-1} cm^2 (7 M$\odot$ yr^{-1}) assuming $\mu = 1.5$, and $\sim 2 \times 10^{40}$ erg s^{-1} cm^2 (0.1 M$\odot$ yr^{-1}) for $\mu = 10$ (assuming an average equivalent width for our sample).

We are sensitive to sources with higher SFR_{UV} at a fixed $\mathrm{SFR}_{\mathrm{H}\alpha}$, the fact that our sample mostly does not fall in this region likely has an underlying physical explanation, and may have to do with the age of our galaxies. Our data also enables a comparison of SFR indicators and inferred galaxy size. In general, Figure 5.2 shows that our sources with the smallest half light radii preferentially scatter off of the constant star formation relation, we explore implications of this in the next subsection.

In Figure 5.3 plot the ratio of the two SFR indicators, $\mathrm{SFR}_{\mathrm{H}\alpha}/\mathrm{SFR}_{UV}$ as a function of stellar mass. The points are color-coded by size. Within the stellar mass range that contains the most galaxies in our sample, $8.5 \leq Log\ M_\star/M_\odot \leq 9.5$, we find a typical ratio of $\log\mathrm{SFR}_{\mathrm{H}\alpha}/\mathrm{SFR}_{UV} = 0.5$

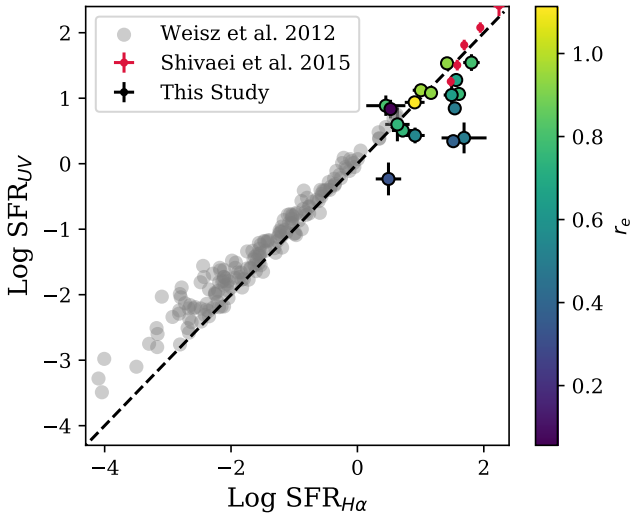

Figure 5.2: Hα and UV SFRs color-coded by r_e for our sample. We compare to the Local Volume sample (grey, Lee et al. 2009) and a higher stellar mass $z = 2$ sample (crimson, Shivaei et al. 2015). The scatter in our sample is likely due to bursty star formation.

(i.e., a factor of ~3). Some data points scatter as high as factors of ~10-20. There is no clear trend between SFR$_{H\alpha}$/SFR$_{UV}$ and stellar mass. Because of the selection effects in our sample, we caution against drawing broad population-level conclusions (e.g., a concrete duty cycle) from this sample, and only suggest that low-mass galaxies at cosmic noon are capable of moderate to large bursts of star formation.

We next compare findings to studies from different redshifts. Such comparisons illustrate the increase in scatter of SFR$_{H\alpha}$/SFR$_{UV}$ at higher stellar masses as a function cosmic time. Note that we are not trying to connect progenitors: a log M_* = 8 M$\odot$ galaxy at $z = 2$ will grow $\propto$ M$_*$ (Leja et al. 2013). This comparison is only meant to illustrate the differences in the stellar masses at which bursty star formation occurs at different cosmic epochs as well as what can gleaned if a complete sample at $z \sim 2$ becomes available.

When comparing to the LV data, we are clearly not complete for lower burstiness parameters, as the flux limit for this survey roughly corresponds to the high end of Hα flux detection in the Lee et al. (2009); Weisz et al. (2012). However, the LV sample *is complete*, for the stellar mass bins corresponding to our sample, in *higher* Hα fluxes. Therefore, even though our median L$_{H\alpha}$/L$_{UV}$ values are likely an upper limit, we can confidently conclude that the upwards scatter in the luminosity ratio has significantly increased with redshift.

The mass range of our sample was explored at $z \sim 1$ in Guo et al. (2016b), though with Hβ instead of Hα. They also found evidence for burstiness at a mass range of $8.5 \leq Log\ M_* \leq 9.5$, which in LV galaxies is consistent with constant star formation. Though the current work and the $z = 1$ sample both show an evolution towards a burstier mode of star formation, our galaxies show

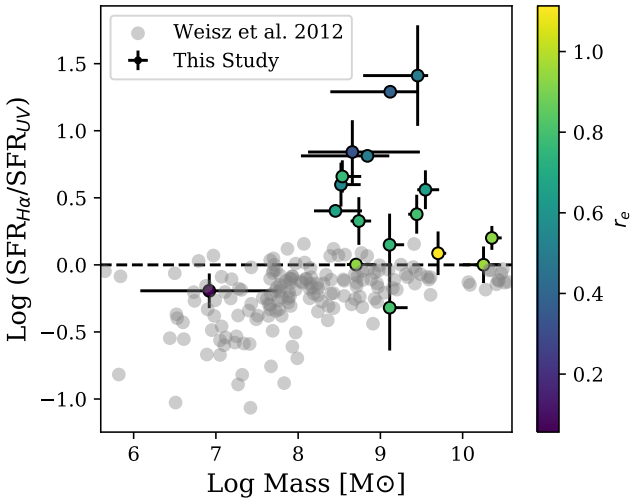

Figure 5.3: SFR$_{\mathrm{H}\alpha}$/SFR$_{UV}$as a function of stellar mass. Galaxies from our sample are color-coded by r_e and Local Volume galaxies from Weisz et al. (2012) shown in grey. The typical Hα SFR is a factor of ∼3 larger than the UV SFR, though in some cases the ration is more than an order of magnitude. We find no clear stellar mass dependence for SFR$_{\mathrm{H}\alpha}$/SFR$_{UV}$in our sample.

yet higher upwards scatter than the $z = 1$ sample, likely resulting from higher gas accretion rates (Tacconi et al. 2010; Genzel et al. 2015; Silverman et al. 2015) and subsequently more violent starbursts that were more likely att $z = 2$ (e.g., Madau & Dickinson 2014).

An evolution towards increased burstiness in high redshift galaxies is in line with theoretical predictions both from cosmological zoom-in simulations (e.g., Sparre et al. 2017) and analytic prescriptions (e.g., Faucher-Giguère 2018). Galactic dynamical times scales, and therefore the free fall time of gas into galaxies, decrease with increasing redshift. Faucher-Giguère (2018) suggest that as of $z \sim 2$, the free-fall time for gas at all masses $< 10^{10.5}$M ⊙ is shorter than the time scales on which supernovea feedback may counter this in-fall, making them inherently bursty. This picture is supported through the evolution of SFR$_{\mathrm{H}\alpha}$/SFR$_{UV}$with redshift that emerges from comparing our sample to LV and low redshift results.

If we expect burstiness due to shorter dynamical times in the early Universe to be the major driver for this evolution, we would expect even higher redshift galaxies, at comparable stellar masses, to have similar SFR$_{\mathrm{H}\alpha}$/SFR$_{UV}$ values. When we compare our sample to that of the $z \sim 4$ galaxies investigated in Faisst et al. (2019), albeit at slightly higher masses ($9 \leq \log\ M_\star/M_\odot \leq 10.5$), we find a similar median SFR$_{\mathrm{H}\alpha}$/SFR$_{UV}$. Further, if galaxies below $\log M_\star/M_\odot = 10$ are expected to be bursty at the redshifts considered in this work, we would expect SFR$_{\mathrm{H}\alpha}$/SFR$_{UV}$ not to vary as a function of mass for our sample. Therefore, the lack of correlation seen in Figure 5.3 is further confirmation of short dynamical timescale driven burstiness.

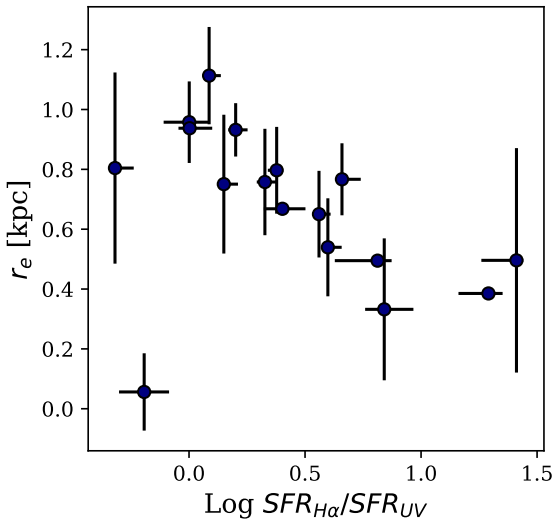

Figure 5.4: $SFR_{H\alpha}/SFR_{UV}$ as a function of r_e. This is highly correlated, indicating either that star formation is increasingly volatile for smaller systems, or alternatively that r_e is increasingly probing only the most recent star forming regions for systems where present SFRs are high.

5.3.1.2 The Effects of Recent Star Formation on Apparent Galaxy Size

Figure 5.4 shows $L_{H\alpha}/L_{UV}$ as a function of radius for galaxies in our sample. Here, there is a strong anti-correlation between the size and burstiness. A physical explanation for this trend is that bursts of star formation can affect the spatial distribution of mass in low-mass systems. For example, in the wet compaction scenario (e.g., Dekel et al. 2013), galaxies go through an intense starburst which drives overall compaction of the galaxy mass. Other theoretical work (e.g., Zolotov et al. 2015) predicts that low-mass galaxies undergo multiple phases of dissipative compaction between $2 < z < 4$ into compact star forming 'blue nugget' systems. In this scenario, one may expect an extreme burst (fueled by massive gas in-fall), to correlate with r_e. With this interpretive lens, larger galaxies are physically less bursty, dynamical effects correlating with burstiness drive galaxies to smaller and smaller radii.

However, a more probable interpretation of the trend in Figure 5.4, is that larger galaxies *appear* larger since they do not have an ongoing burst. In a Sérsic fit, r_e is the radius that is comprised of half of the total measured flux in galaxy. If most the UV light corresponds to an ongoing localized star burst, this will yield r_e measurements that are out of sync with mass-weighted radii of even recent star formation. In other words, instantaneous star formation dominates the measured half-light radii of our sample, especially in galaxies with lower rates of recent star formation. Therefore, the higher the ratio between Hα and UV SFR, the more instantaneous (and localized) light drives the r_e fit. This would suggest that what we are observing is the buildup of dense cores in low mass galaxies as observed at higher masses and lower redshifts (Barro et al. 2014; van Dokkum et al.

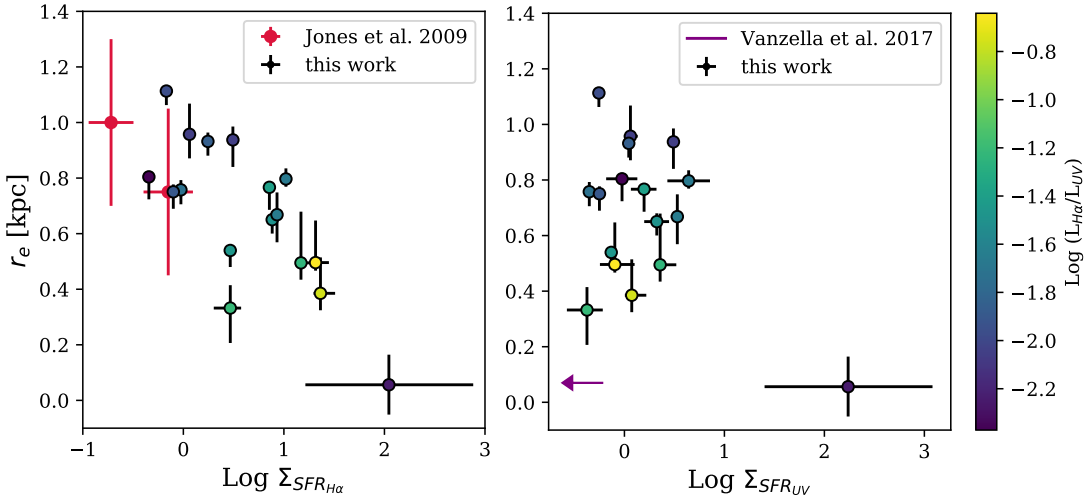

Figure 5.5: **Left:** Size (r_e) as a function of $\Sigma_{SFR,\,H\alpha}$ color-coded by $L_{H\alpha}/L_{UV}$ for sources from this work, and shown in red for sources from Jones et al. (2010). r_e strongly correlates with the density of very recent (i.e., Hα) star formation. The density of current star formation largely increases with $SFR_{H\alpha}/SFR_{UV}$. **Right:** r_e as a function of $\Sigma_{SFR,\,UV}$with our sources color coded by $L_{H\alpha}/L_{UV}$ and a $\mu \sim 20$ source described in Vanzella et al. (2016) and Vanzella et al. (2017) shown in purple. We do not find a significant trend between these two parameters, indicating that our radius is not set by time averaged star formation.

2015; Barro et al. 2017).

In Figure 5.5, we further investigate this interpretation by comparing r_e to $\Sigma_{SFR,\,UV}$ and $\Sigma_{SFR,\,H\alpha}$ for our sample, and included select literature values for comparison. (Jones et al. 2010; Vanzella et al. 2016). Though there are some high redshift studies in this mass range (Livermore et al. 2015; Stark et al. 2008), we limit our comparison to lensed galaxies with $\mu < 20$ to ensure consistency with our sample.

If the measured half-light radius is dominated by the ongoing starburst, we expect r_e to correlate more with $\Sigma_{SFR,\,H\alpha}$ (a proxy for the starburst), than $\Sigma_{SFR,\,UV}$, which corresponds to star formation in the galaxy averaged over $\sim$ 100yrs. We find that though L_{UV} correlates with r_e for our sample, this does not translate into nearly as strong of a correlation in $\Sigma_{SFR,\,UV}$as it does for $\Sigma_{SFR,\,H\alpha}$. This finding is despite the fact that there no correlation between r_e and $L_{H\alpha}$. Jones et al. (2010) likewise shows this same trend in r_e (red points in Figure 5.5).

The lack of correlation between $SFR_{H\alpha}$ and r_e, means that the mass produced during these bursts does not correlate with the sources for which we observe the most 'compaction' in light weighted radii. Though these galaxies are likely forming cores, we caution against ascertaining the mass densities in these systems from light weighted radii, as their r_e does not correspond to the mass produced in the starburst. Therefore, the light weighted size of cores, even at lower resolutions, may be a poor gauge of the mass forming in the central part of these systems.

We use a simple galfit model to test the effects of recent star formation on r_e. Specifically, we generate two mock disks, one with a 100pc radius and the other with a 1kpc radius, and set the luminosity ratio between them to represent our typical $\mathrm{SFR}_{\mathrm{H}\alpha}/\mathrm{SFR}_{UV}$. We then add standard noise and attempt to recover the size of the full source. This results in a best fit $r_e \approx 400pc$, which is remarkably close to our average r_e for our sample, given the arbitrary size choices we made.

At higher stellar masses, some studies (Mosleh et al. 2017; Suess et al. 2019) show that steep color gradients can cause an immense difference between the measured light-weighted and mass-weighted (intrinsic) sizes of galaxies at high mass, but that intrinsic and light-weighted radii tend to agree at 10^{10}M$\odot$. Shibuya et al. (2015) inferred a 20% difference in r_e measured in blue versus red bands for galaxies at $z < 2$, but posited that this would decrease towards higher redshift as the young age of the Universe would not allow the evolution of stellar populations that accounts for steep color gradients. This study motivates that rather than steep color-gradients driven by diversity of stellar populations, the volatility of star formation at masses below 10^{10}M $\odot$ makes the UV a poor measure of r_e at $z > 2$.

The short timescales of star formation variability in low-mass galaxies likely affects r_e determinations at even higher redshits than our sample. At these epochs, there is both theoretical and observational work that suggests star formation in galaxies is similarly bursty (e.g., Ma et al. 2017; Faisst et al. 2019). We speculate that the systematic outlined here may explain the over-representation of compact sources in past HFF studies across redshifts (Kawamata et al. 2015b; Kawamata et al. 2017; Bouwens et al. 2017). If sizes are primarily driven by the ratio of instantaneous to recent star formation at low masses, it may explain why even accounting for surface brightness limits by comparing high and low shear regions, still results in an excess of compact galaxies at faint luminosities (Bouwens et al. 2017a).

Given the selection effects of our sample, it is possible that the trend we find it not the entire story. Gravitational lensing conserves surface brightness, which is known to bias observations against diffuse sources (Grazian et al. 2011; Bouwens et al. 2017a; Zick et al. 2018), meaning that we may be missing a diffuse component of highly bursty galaxies due to surface brightness limits. However, given the surface brightness limit of our sample, this effect is not the primary driver the correlation between $\mathrm{SFR}_{\mathrm{H}\alpha}/\mathrm{SFR}_{UV}$and r_e. We examine the potential for bias in the $\mathrm{SFR}_{\mathrm{H}\alpha}/\mathrm{SFR}_{UV}$-$r_e$ relation itself. We find that r_e is less correlated with L_{UV} than it is with $\mathrm{SFR}_{\mathrm{H}\alpha}/\mathrm{SFR}_{UV}$. Furthermore as we find no trend between H$\alpha$and r_e, we do not expect the relation between L_{UV} and radius to significantly account for this relation.

5.3.2 Kinematics Evidence for Bursty Star Formation

Given the dynamical information provided by MOSFIRE spectroscopy, we attempt to place our sources on the Tulley-Fisher (TF) relation (Tully & Fisher 1977), which relates the stellar content of galaxies to their rotational velocity (V). However, as we measure integrated σ, which is a superposition of V and an isotropic velocity, we do not expect a tight relation, yet we can use it as a coarse stand-in following Erb et al. (2006b).

We plot this relation in the left panel of Figure 5.6 for our sample as well as the Hirtenstein et al. (2019) sample. The latter consists of Keck/OSIRIS integral field spectroscopy for lensed

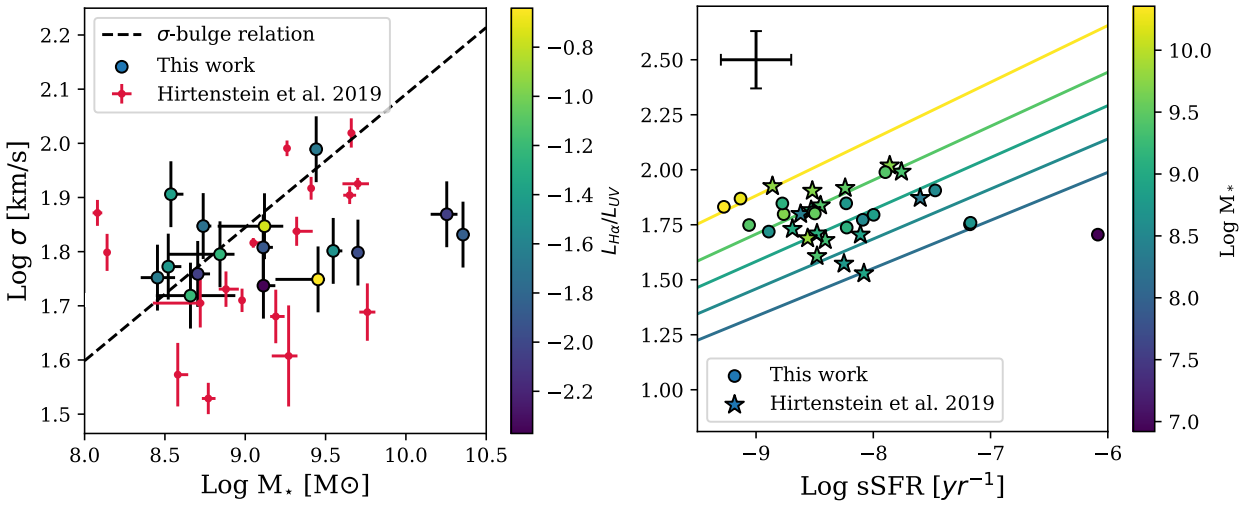

Figure 5.6: **Left:** mass as a function of velocity dispersion color coded by burst, with sources from Hirtenstein et al. (2019) shown in red. We find a weak trend in σ with increasing mass, for all but our least bursty sources. This provides qualitative support that despite slit misalignment errors, our velocity dispersion measurements are on the whole indicative of underlying system dynamics. **Right:** Log σ as a function of UV derived Log sSFR. We show our measurements and sources from Hirtenstein et al. (2019) color coded by mass as circles and stars, respectively. The colored lines correspond to predictions from the FIRE simulation for log $M_\star = 8.0, 8.5, 9.0, 9.5, 10.2 M_\odot$ (blue to yellow). We find excellent agreement between our samples and theoretical predictions at fixed mass.

galaxies at approximately the same redshift and mass range as ours. We compare to their velocity dispersions integrated over line of site (see Hirtenstein et al. 2019, for details). The left panel of Figure 5.6 shows a weak correlation with mass that breaks at higher velocity dispersions. Given that the underlying assumption for the TF relation is that mass is oriented in a disk and therefore $V >> \sigma_o$ (where σ_o is random isotropic dispersion), it is not surprising that our relationship is not tight.

Additionally, we examine our sources relative to the local σ-bulge relation, which we derive from a combination of the M_{BH}-σ relation (Tremaine et al. 2002) and the M_{Bulge}-M_{BH} relation (Marconi & Hunt 2003). Erb et al. (2006b) finds that their galaxies tend to lay on or below this local relation, a trend also seen in our data at similar stellar mass. At lower masses, we find scatter above the local σ-bulge relation for both ours and the Hirtenstein et al. (2019) sample.

In Miller et al. (2013), the authors find that the largest scatter from the TF relation occurs in galaxies that are bulgeless, and speculate that the formation of a bulge drives the maturation of disks. We therefore look for a trend with $SFR_{H\alpha}/SFR_{UV}$ in our σ-M_* relation, as constant $SFR_{H\alpha}/SFR_{UV}$ may correspond to systems that have already formed bulges and would be more likely to follow the local relation. We however do not find evidence for this in the current sample. We further use our

integrated σ measurements to look for a relation between star formation and kinematics. We do not find any correlation between our measured $SFR_{H\alpha}/SFR_{UV}$ values and σ, even at fixed masses.

The right panel of Figure 5.6 shows the relationship between between σ and specific star formation rate (sSFR) at fixed mass. Recent theoretical work has shown that feedback in dwarf galaxies can be powerful enough to alter the inner dark matter profile of the galaxy (Madau et al. 2014; Oñorbe et al. 2015b; El-Badry et al. 2016; Garrison-Kimmel et al. 2017). El-Badry et al. (2017) use the Feedback in Realistic Environments (FIRE) simulations (Hopkins et al. 2012) to show that this process should drive newly formed stars into increasingly dispersion dominated orbits and predict a correlation between (specific) SFR and the potential of a galaxy, for which σ is a proxy.

We overplot theoretical predictions from FIRE as parameterized in Hirtenstein et al. (2019) for $\log M_\star = 8.0, 8.5, 9.0, 9.5, 10.2$ $M_\odot$ along with our combined samples in the right panel of Figure 5.6. Our results adhere closely to the theoretical prediction at fixed stellar mass. For local low mass galaxies, El-Badry et al. (2017) finds a 50 Myr delay time between star formation and change in σ, due to rapid shutoff of star formation. This is due essentially instantaneous feedback-driven heating as opposed to the depletion of gas from the center of the galaxy, which takes of order a dynamical time. They therefore predict more scatter in the relation between σ and Hαderived sSFR than in UV derived sSFR.

We do not observe this lag. Instead, we find the same amount of scatter in Hα and UV sSFRs. This finding is in agreement with Hirtenstein et al. (2019), who posit the discrepancy may be due to their use of a gas based σ as opposed to a stellar based σ measurement. We consider an additional interpretation. Since dynamical timescales at $z = 2$ are shorter than stellar feedback times, we expect gas at the center of the galaxy to dissipate on timescales on the same order as gas heating due to feedback. We therefore no longer expect an observable delay between σ and sSFR that El-Badry et al. (2017) predicted for $z = 0$ galaxies.

5.3.2.1 Dynamical Masses

Leveraging our measured σ and r_e, we attempt to constrain the dynamical masses of our sample according to:

$$M_{dyn} = C\frac{\sigma^2 r_{vir}}{G} \tag{5.1}$$

where we have taken the virial radius (r_{vir}) to be the effective half light radius (r_e) as done in Maseda et al. (2013).

We show the resulting relation between M_* and M_{dyn} for our sample in Figure 5.7, where the dashed line indicates a one to one ration. As dynamical mass probes the total baryonic and dark matter mass of a galaxy, we expect all of our sources to fall above the dashed line. The majority of our systems are consistent with this scenario, when error bars are considered. All but one of our galaxies has a dynamical mass within a factor of ten of its corresponding stellar mass. The two measurements that are not consistent with the physical regime may be the result of misaligned slits in σ measurements.

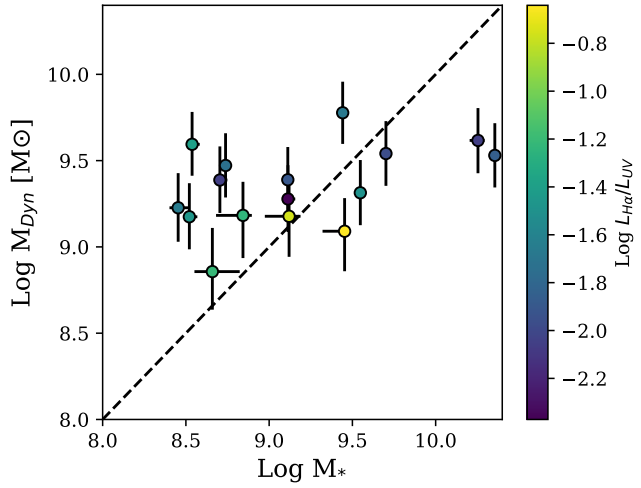

Figure 5.7: Dynamical mass as a function of stellar mass. The black dotted line shows a slope of one, corresponding to a one to one relation. We expect dynamical mass to be higher than stellar mass both due to dark matter, which enters into the dynamical mass, as well as the fact that these systems are actively star forming and therefore should have non-negligible gas masses. We color-code our sources by $L_{H\alpha}/L_{UV}$ but find no trend with M_{Dyn}.

Using the UV-based SFRs, we coarsely estimate the gas masses of our sources using the Kennicutt-Schmidt (KS) relation (Kennicutt 1998). Figure 5.8 shows a comparison bewteen the total baryonic mass and the dynamical masses of our sample. Effectively, all our sources now occupy an unphysical region of parameter space (i.e., the baryonic mass exceeds the dynamical mass). The use of Hα SFRs exacerbates the disagreement.

As discussed in the previous section, our measured r_e likely tracks individual star-forming regions rather than the half mass radius, let alone r_{vir}. We therefore consider the case where where our r_e are intrinsically low, and show dynamical mass estimates assuming a constant radius of 1 kpc, (i.e., a value that reflects the galaxy not just the compact star-forming region).

We compare points with the assumed larger sizes (indicated by a red x) to our inferred total baryonic masses from the KS relation in Figure 5.8. We find find that inflating our r_e values cannot fully explain why our total baryonic masses are larger than our dynamical masses. We therefore posit that the KS relation *overestimates* gas values for bursty, low mass, high-redshift galaxies. This is perhaps unsurprising, given that the KS relationship is established for $L_\star$ galaxies in the LV that are consistent with constant recent SFHs, whereas our galaxies are highly-bursting low-mass systems at cosmic noon. However it is interesting that none of our sources seem to have much *higher* gas masses than local galaxies as seen for extreme line emitting galaxies in (Maseda et al. 2014).

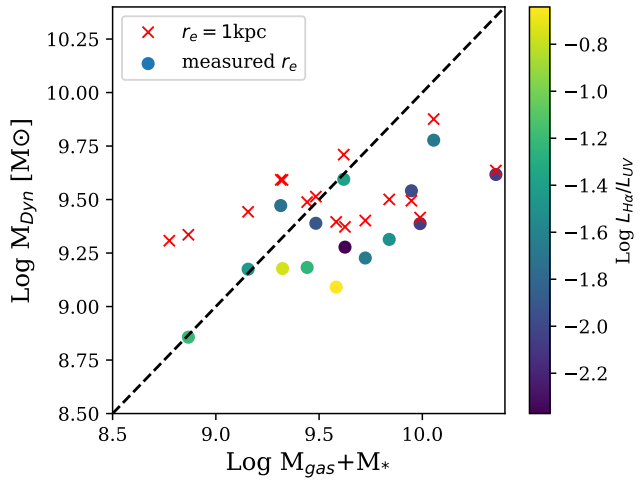

Figure 5.8: Dynamical mass as a function of combined gas and stellar mass, where the former is derived from the KS relation. The black dotted line shows a slope of one, corresponding to a one to one relation. With the KS correction for gas masses, we find that the majority of our sources lay in an unphysical region of parameter space. Though changes to the IMF with redshift could partially account for this offset, the most likely explanation for this is that the KS relation overestimates gas fractions for these sources.

5.4 Conclusions

In this study we leverage MOSFIRE/Keck spectroscopy in conjunction with deep HFF photometry to study the recent SFHs and kinematics of 33 moderately lensed low mass galaxies at cosmic high noon. The current study previews the potential of spectroscopy to connect structure and star formation history, as well as the challenges in interpreting even high spatial resolution photometry. We summarize our findings below.

- We measure $\mathrm{SFR}_{\mathrm{H}\alpha}/\mathrm{SFR}_{UV}$ for $7 < LogM_* < 10$ galaxies at $z = 2$ and find a deviation from unity analogous to that found in low mass dwarf galaxies in the local volume. We further compare our median $\mathrm{SFR}_{\mathrm{H}\alpha}/\mathrm{SFR}_{UV}$ for an $8.5 < LogM_* < 9.5$ mass bin to literature values across cosmic time and show an evolution towards burstiness at higher masses with redshift, and consistent $\mathrm{SFR}_{\mathrm{H}\alpha}/\mathrm{SFR}_{UV}$ values between our sample and a slightly higher mass $z = 4$ sample.

- We also find a tight correlation between $\mathrm{SFR}_{\mathrm{H}\alpha}/\mathrm{SFR}_{UV}$ and r_e as well as r_e and $\Sigma_{SFR,\ H\alpha}$ (the correlation with $\Sigma_{SFR,\ UV}$ is far weaker). The combination of these observations indicates that our measured r_e is dominated not by young stellar populations but by essentially *instantaneous* star formation. This effect is exacerbated for especially bursty young galaxies that can have

large offsets between their L_{UV} and $L_{H\alpha}$. It further indicates that Hα may probe star formation on small scales not indicative of even recent star formation within the galaxy.

- Integrated σ values track both UV and Hα based sSFR measurements at fixed mass according to predictions from cosmological zoom-in simulations for low mass galaxies. This agreement with theory may imply an observational evidence of stellar feedback driven fluctuations in the gravitational potential of these galaxies.

- Finally we measure dynamical masses and find that the local KS relation tends to overpredict gas masses for our galaxies even when accounting for uncertainties in galaxy sizes.

Our results underscore the importance of the far-IR in the study of rapidly fluctuating star formation in low mass galaxies at $z = 2$ as well as the potential challenges of reconciling UV and Hα based star formation probes for low mass systems. The far-IR wavelengths that can be investigated with the advent of the $JamesWebbSpaceTelescope$ (JWST) will provide a way to gauge the intrinsic morphologies of these low mass galaxies. The high resolution of IR filters in JWST/NIRCam will enable r_e measurements from redder, more stable bands more indicative of intrinsic radii. The comparisons on these filters can provide a nuanced picture of star forming regions in the context of low mass galaxy morphology. Thus, we can expect future instruments to build on the picture of star formation, feedback and morphology presented in this study.

Chapter 6

Conclusions and Future Implications

In this dissertation I outlined techniques and observations aimed at investigating typical and low mass galaxies at cosmic high noon. I combined rest-frame optical spectroscopy with HUDF and HFF photometry, as well as stellar archaeology to constrain star formation in low mass galaxies from multiple directions. Here, I summarize the results presented in this dissertation below and discuss their implications in the era of *JWST*.

I first used the medium resolution rest-frame optical MOSDEF survey to statistically infer the SFHs of over 1500 galaxies at the peak epoch of star formation. I utilize the 4000 Å break and balmer lines to directly study the stellar populations of these galaxies, which had previously only been done for the most massive quiescent galaxies. To attain the signal to noise necessary to study continuum features, I divided the sample into five galaxy types and stacked each using composite SEDs to normalize the continuum. Comparing purely continuum features with Hα equivalent width, I found that quiescent, post-starburst and green valley galaxies at $z = 2$ formed their stars rapidly ($\tau \sim 0.1 - 0.2$ Gyr) compared to average local galaxies and the star forming galaxy types at $z = 2$ ($\tau > 1$ Gyr). By comparing SFHs for transitional galaxies I hypothesized a new path to quenching involving a compact dusty phase.

I then attempt to understand whether proto-globular clusters could contribute to measurements of the faint end of the UVLF using the stellar fossil record of the Fornax dwarf spheroidal and its five GCs. I use CMD fits combined with stellar population synthesis modeling to reconstruct observations of the dwarf galaxy and its GCs across cosmic time and find that despite comprising $<\sim 5\%$ of total stellar mass at $z > 2$, forming GCs could contribute 10-100 times the UV flux of their host dwarf. Additionally, conservation of surface brightness in lensed fields, means that the HFF may be biased towards observing forming star cluster rather than dwarf galaxies at faint luminosities. This is especially problematic as misclassifying a GC as a dwarf galaxy could introduce order-of-magnitude errors in abundance matching or wash out a turnover in the UVLF.

To investigate the nature of the faint compact sources in the HFF, I follow up 39 lensed sources at $z = 1.8 - 3.2$ with deep photometry and Spitzer/IRAC coverage using Keck/MOSFIRE. I first study a Milky Way progenitor galaxy with a rest-frame UV-luminous $r_e = 40^{+70}_{-30}$pc, $M_\star \sim 10^{8.2} M_\odot$ 'clump' at a projected distance of ~100 pc from its center. I introduce a new technique combining spectroscopy and non-parametric SED fitting with varying priors to try and distinguish between an

insitu or accretion formation scenario for the 'clump'.

Finally, I further leverage the results from this survey to study the star formation, kinematics and morphologies of low mass galaxies at cosmic high noon. My sample is comprised of 38 $7 \leq \log M_\star/M_\odot \leq 10.2$ moderately gravitationally lensed ($\mu < 20$), star-forming galaxies at $1.8 \leq z \leq 3.2$. I compare dust corrected instantaneous (Hα) and time averaged (UV) star formation rates in order to constrain the extent to which the scatter in the mass-size relation at this mass range is driven by 'burstiness'. By comparing the median burstiness parameter from local galaxies through z = 1 galaxies and z = 4 galaxies, my results support models in which high redshift star formation at Log $M_\star < 10M\odot$ is as bursty as extremely low mass systems in the Local Volume due to the scaling of galactic dynamical timescales with redshift. I compare measured velocity dispersions to sSFR and find that my measuremnts are consistant with observational signatures of feedback driven gravitational potential change predicted from the FIRE simulations. Finally, I observe that size correlates with the burstiness of a galaxy, potentially supporting a wet compaction scenario for low mass galaxies at these redshifts. However, examining the instantaneous and time averaged star formation densities as a function of radius, I hypothesize that the correlation between $SFR_{H\alpha}/SFR_{UV}$ and r_e, is likely an observational bias on high-z star forming galaxies at $< 10^{10}M_\odot$.

These results represent the cutting edge of what is possible with current instruments and preview the types of measurements that will be more routine with the advent of *JWST*. Current estimates using the *JWST/NIRSPEC* exposure time calculator, show that Hα, Hβ, and [O iii] can be detected with $S/N > 5$, in under two hours for the galaxy I present in chapter 4. The higher sensitivity and spatial resolution of *JWST/NIRSPEC* compared to ground based near-IR spectrometers will enable a statistical implementation of the methods described in chapter 4 which could provide a useful tool for characterizing the assembly history of high-z galaxies. Here, the future red-arm of *Keck/KCWI* may prove to be an interesting complement. I have found that faint, low mass sources could have line widths that make them far easier to detect than their magnitudes would imply. Work on *MUSE/VLT* has shown blind spectroscopic studies to be fruitful in bluer bands (Maseda et al. 2018). The combination of the red arm of KCWI/Keck and JWST/NIRSPEC and JWST/NIRCam follow up could allow a detailed characterization of star forming clumps, and faint star forming galaxies.

My findings in chapter 5 that the size of faint low mass galaxies in the HFF are likely set by the ratio of recent to current star formation, further motivates the importance of JWST/NIRCam in characterizing galaxy morphologies at $z = 2$. Increased pixel resolution of JWST/NIRCam filters will allow F814W-like resolution for redder bands, that are less likely to dominated by this effect. My findings that even among young stellar populations, r_e can be an extremely biased tracer of the half mass radius, has further implications for yet higher redshift galaxies which will likely face the same systematics as current HST/WFC3 observations.

Finally, resolved stellar population studies with *JWST* along with future GAIA data releases (Lindegren et al. 2016b; Pancino et al. 2017) are poised to increase the precision on distances and therefore inferred ages for resolved stellar populations. JWST/NIRCam will measure photometry for the first stars past the main sequence turn-off (MSTO) outside the local group. Observations fainter than the MSTO will mitigate the age-metallicity degeneracy that currently contributes to age uncertainty in farther galaxies (Correnti et al. 2016). Precision ages for more nearby resolved stellar

populations will improve the constraining power of studies akin to the one discussed in chapter 3.

Overall, the approach of this dissertation has been to leverage the self consistency requirement for a theory of galaxy evolution, to constrain star formation models and elucidate observational limitations. Within the context of next generation instruments, this general approach is poised to become even more fruitful.

Bibliography

Abramson, L. E., & Morishita, T. 2018, ApJ, 858, 40
Alavi, A., Siana, B., Richard, J., et al. 2016, ApJ, 832, 56
Arca-Sedda, M., & Capuzzo-Dolcetta, R. 2016, MNRAS, 461, 4335
Atek, H., Siana, B., Scarlata, C., et al. 2011, ApJ, 743, 121
Atek, H., Kneib, J.-P., Pacifici, C., et al. 2014, ApJ, 789, 96
Atek, H., Richard, J., Jauzac, M., et al. 2015, ApJ, 814, 69
Azadi, M., Coil, A. L., Aird, J., et al. 2017, ApJ, 835, 27
Baldry, I. K., Balogh, M. L., Bower, R. G., et al. 2006, MNRAS, 373, 469
Balogh, M. L., Morris, S. L., Yee, H. K. C., Carlberg, R. G., & Ellingson, E. 1999, ApJ, 527, 54
Barden, M., Häußler, B., Peng, C. Y., McIntosh, D. H., & Guo, Y. 2012, MNRAS, 422, 449
Barro, G., Trump, J. R., Koo, D. C., et al. 2014, ApJ, 795, 145
Barro, G., Kriek, M., Pérez-González, P. G., et al. 2016, ApJ, 827, L32
—. 2017, ApJ, 851, L40
Bastian, N., & Lardo, C. 2017, ArXiv e-prints, arXiv:1712.01286 [astro-ph.SR]
Behroozi, P. S., Wechsler, R. H., & Conroy, C. 2013, ApJ, 770, 57
Bekki, K., & Yahagi, H. 2009, Formation of Intracluster and Intercluster Globular Clusters, ed. T. Richtler & S. Larsen, 373
Bekki, K., Yahagi, H., Nagashima, M., & Forbes, D. A. 2008, MNRAS, 387, 1131
Belli, S., Newman, A. B., & Ellis, R. S. 2015, ApJ, 799, 206
Belokurov, V., Erkal, D., Evans, N. W., Koposov, S. E., & Deason, A. J. 2018, MNRAS, 478, 611
Bezanson, R., van Dokkum, P. G., van de Sand e, J., et al. 2013, ApJ, 779, L21
de Boer, T. J. L., & Fraser, M. 2016, A&A, 590, A35
de Boer, T. J. L., Tolstoy, E., Hill, V., et al. 2012a, A&A, 544, A73
de Boer, T. J. L., Tolstoy, E., Hill, V., et al. 2012b, A&A, 544, A73
—. 2012c, A&A, 539, A103
Bonaca, A., Tanner, J. D., Basu, S., et al. 2012, ApJ, 755, L12
Bouwens, R. J., Illingworth, G. D., Oesch, P. A., et al. 2017a, ApJ, 843, 41
Bouwens, R. J., Oesch, P. A., Illingworth, G. D., Ellis, R. S., & Stefanon, M. 2017b, ApJ, 843, 129
Bouwens, R. J., van Dokkum, P. G., Illingworth, G. D., et al. 2017c, ArXiv e-prints, arXiv:1711.02090
Bouwens, R. J., van Dokkum, P. G., Illingworth, G. D., et al. 2017, eprint arXiv:1711.02090
Bouwens, R. J., Illingworth, G. D., Oesch, P. A., et al. 2015, ApJ, 803, 34

Bovy, J., Rix, H.-W., Liu, C., et al. 2012, ApJ, 753, 148
Boylan-Kolchin, M. 2017a, MNRAS, 472, 3120
—. 2017b, ArXiv e-prints, arXiv:1711.00009
Boylan-Kolchin, M., Bullock, J. S., & Garrison-Kimmel, S. 2014, MNRAS, 443, L44
Boylan-Kolchin, M., Bullock, J. S., & Kaplinghat, M. 2011, MNRAS, 415, L40
—. 2012, MNRAS, 422, 1203
Boylan-Kolchin, M., Springel, V., White, S. D. M., Jenkins, A., & Lemson, G. 2009, MNRAS, 398, 1150
Boylan-Kolchin, M., Weisz, D. R., Bullock, J. S., & Cooper, M. C. 2016, MNRAS, 462, L51
Boylan-Kolchin, M., Weisz, D. R., Johnson, B. D., et al. 2015, MNRAS, 453, 1503
Boylan-Kolchin, M., Weisz, D. R., Johnson, B. D., et al. 2015, MNRAS, 453, 1503
Bozek, B., Marsh, D. J. E., Silk, J., & Wyse, R. F. G. 2015, MNRAS, 450, 209
Bradač, M., Treu, T., Applegate, D., et al. 2009, ApJ, 706, 1201
Brammer, G. B., van Dokkum, P. G., & Coppi, P. 2008, ApJ, 686, 1503
Brammer, G. B., van Dokkum, P. G., Franx, M., et al. 2012, ApJS, 200, 13
Brinchmann, J., Charlot, S., White, S. D. M., et al. 2004, MNRAS, 351, 1151
Brodie, J. P., & Strader, J. 2006, ARA&A, 44, 193
Broussard, A., Gawiser, E., Iyer, K., et al. 2019, ApJ, 873, 74
Brown, T. M., Tumlinson, J., Geha, M., et al. 2012, ApJ, 753, L21
Bruzual, G., & Charlot, S. 2003, MNRAS, 344, 1000
Bullock, J. S., & Boylan-Kolchin, M. 2017, ARA&A, 55, 343
Cabrera-Ziri, I., Lardo, C., Davies, B., et al. 2016, MNRAS, 460, 1869
Calzetti, D., Armus, L., Bohlin, R. C., et al. 2000, ApJ, 533, 682
Caplar, N., & Tacchella, S. 2019, MNRAS, 487, 3845
Cava, A., Schaerer, D., Richard, J., et al. 2018, Nature Astronomy, 2, 76
Chaboyer, B., McArthur, B. E., O'Malley, E., et al. 2017, ApJ, 835, 152
Chabrier, G. 2003, PASP, 115, 763
Chernoff, D. F., Kochanek, C. S., & Shapiro, S. L. 1986, ApJ, 309, 183
Choi, J., Conroy, C., Ting, Y.-S., et al. 2018, ApJ, 863, 65
Choi, J., Dotter, A., Conroy, C., et al. 2016, ApJ, 823, 102
Cignoni, M., Sabbi, E., van der Marel, R. P., et al. 2015, ApJ, 811, 76
Coe, D., Bradley, L., & Zitrin, A. 2015, ApJ, 800, 84
Cole, A. A., Weisz, D. R., Skillman, E. D., et al. 2017, ApJ, 837, 54
Conroy, C., & Gunn, J. E. 2010, ApJ, 712, 833
Conroy, C., Gunn, J. E., & White, M. 2009a, ApJ, 699, 486
—. 2009b, ApJ, 699, 486
Conselice, C. J., Bluck, A. F. L., Mortlock, A., Palamara, D., & Benson, A. J. 2014, MNRAS, 444, 1125
Correnti, M., Gennaro, M., Kalirai, J. S., Brown, T. M., & Calamida, A. 2016, ApJ, 823, 18
Creevey, O. L., Thévenin, F., Berio, P., et al. 2015, A&A, 575, A26
Crnojević, D., Sand, D. J., Zaritsky, D., et al. 2016, ApJ, 824, L14
Cusano, F., Garofalo, A., Clementini, G., et al. 2016, ApJ, 829, 26

da Silva, R. L., Fumagalli, M., & Krumholz, M. 2012, ApJ, 745, 145
Daddi, E., Dickinson, M., Morrison, G., et al. 2007, ApJ, 670, 156
Davé, R. 2008, MNRAS, 385, 147
Davis, M., & Peebles, P. J. E. 1983, ApJ, 267, 465
Dekel, A., Zolotov, A., Tweed, D., et al. 2013, MNRAS, 435, 999
Dekel, A., Birnboim, Y., Engel, G., et al. 2009, Nature, 457, 451
Dessauges-Zavadsky, M., Schaerer, D., Cava, A., Mayer, L., & Tamburello, V. 2017, ApJ, 836, L22
Dolphin, A. E. 2002, MNRAS, 332, 91
Domínguez, A., Siana, B., Brooks, A. M., et al. 2015, MNRAS, 451, 839
Dotter, A., Chaboyer, B., Jevremović, D., et al. 2008, ApJS, 178, 89
Drlica-Wagner, A., Bechtol, K., Rykoff, E. S., et al. 2015, ApJ, 813, 109
D'Souza, R., & Bell, E. F. 2018, Nature Astronomy, 2, 737
El-Badry, K., Wetzel, A., Geha, M., et al. 2016, ApJ, 820, 131
El-Badry, K., Wetzel, A. R., Geha, M., et al. 2017, ApJ, 835, 193
Elmegreen, B. G., Malhotra, S., & Rhoads, J. 2012, ApJ, 757, 9
Elmegreen, D. M., & Elmegreen, B. G. 2017, ArXiv e-prints, arXiv:1712.02935
Emami, N., Siana, B., Weisz, D. R., et al. 2019, ApJ, 881, 71
Erb, D. K., Pettini, M., Shapley, A. E., et al. 2010, ApJ, 719, 1168
Erb, D. K., Steidel, C. C., Shapley, A. E., et al. 2006a, ApJ, 647, 128
—. 2006b, ApJ, 646, 107
Faisst, A. L., Capak, P. L., Emami, N., Tacchella, S., & Larson, K. L. 2019, ApJ, 884, 133
Fall, S. M., & Zhang, Q. 2001, ApJ, 561, 751
Faucher-Giguère, C.-A. 2018, MNRAS, 473, 3717
Feldmann, R., Hopkins, P. F., Quataert, E., Faucher-Giguère, C.-A., & Kereš, D. 2016, MNRAS, 458, L14
Finkelstein, S. L. 2016, PASA, 33, e037
Finlator, K., Prescott, M. K. M., Oppenheimer, B. D., et al. 2017, MNRAS, 464, 1633
Forbes, D. A., Brodie, J. P., & Grillmair, C. J. 1997, AJ, 113, 1652
Forbes, D. A., Pastorello, N., Romanowsky, A. J., et al. 2015, MNRAS, 452, 1045
Forbes, D. A., Spitler, L. R., Strader, J., et al. 2011, MNRAS, 413, 2943
Förster Schreiber, N. M., Genzel, R., Bouché, N., et al. 2009, ApJ, 706, 1364
Förster Schreiber, N. M., Shapley, A. E., Genzel, R., et al. 2011, ApJ, 739, 45
Freeman, K., & Bland-Hawthorn, J. 2002, ARA&A, 40, 487
Fumagalli, M., da Silva, R. L., & Krumholz, M. R. 2011, ApJ, 741, L26
Fumagalli, M., Labbé, I., Patel, S. G., et al. 2014, ApJ, 796, 35
Gallart, C., Zoccali, M., & Aparicio, A. 2005, ARA&A, 43, 387
Gallazzi, A., Charlot, S., Brinchmann, J., White, S. D. M., & Tremonti, C. A. 2005, MNRAS, 362, 41
Garrison-Kimmel, S., Boylan-Kolchin, M., Bullock, J. S., & Lee, K. 2014, MNRAS, 438, 2578
Garrison-Kimmel, S., Bullock, J. S., Boylan-Kolchin, M., & Bardwell, E. 2017, MNRAS, 464, 3108

Gburek, T., Siana, B., Alavi, A., et al. 2019, arXiv e-prints, arXiv:1906.11849
Genzel, R., Newman, S., Jones, T., et al. 2011, ApJ, 733, 101
Genzel, R., Tacconi, L. J., Lutz, D., et al. 2015, ApJ, 800, 20
Gnedin, N. Y. 2016, ApJ, 825, L17
Gnedin, O. Y., Lee, H. M., & Ostriker, J. P. 1999, ApJ, 522, 935
Governato, F., Zolotov, A., Pontzen, A., et al. 2012, MNRAS, 422, 1231
Gratton, R. G., Carretta, E., & Bragaglia, A. 2012, A&A Rev., 20, 50
Grazian, A., Castellano, M., Koekemoer, A. M., et al. 2011, A&A, 532, A33
Grogin, N. A., Kocevski, D. D., Faber, S. M., et al. 2011, ApJS, 197, 35
Gullberg, B., Swinbank, A. M., Smail, I., et al. 2018, ApJ, 859, 12
Guo, H., Zheng, Z., Behroozi, P. S., et al. 2016a, MNRAS, 459, 3040
Guo, Y., Giavalisco, M., Ferguson, H. C., Cassata, P., & Koekemoer, A. M. 2012, ApJ, 757, 120
Guo, Y., Rafelski, M., Faber, S. M., et al. 2016b, ApJ, 833, 37
Guo, Y., Rafelski, M., Bell, E. F., et al. 2018, ApJ, 853, 108
Harris, W. E., Blakeslee, J. P., & Harris, G. L. H. 2017, ApJ, 836, 67
Haywood, M., Di Matteo, P., Lehnert, M., et al. 2018, A&A, 618, A78
Helmi, A., Babusiaux, C., Koppelman, H. H., et al. 2018, Nature, 563, 85
Hirtenstein, J., Jones, T., Wang, X., et al. 2019, ApJ, 880, 54
Hollyhead, K., Bastian, N., Adamo, A., et al. 2015, MNRAS, 449, 1106
Hopkins, A. M., & Beacom, J. F. 2006, ApJ, 651, 142
Hopkins, P. F., Kereš, D., Murray, N., Quataert, E., & Hernquist, L. 2012, MNRAS, 427, 968
Hopkins, P. F., Kereš, D., Oñorbe, J., et al. 2014, MNRAS, 445, 581
Hoversten, E. A., & Glazebrook, K. 2008, ApJ, 675, 163
Hudson, M. J., Harris, G. L., & Harris, W. E. 2014, ApJ, 787, L5
Huxor, A. P., Ferguson, A. M. N., Veljanoski, J., Mackey, A. D., & Tanvir, N. R. 2013, MNRAS, 429, 1039
Hwang, N., Lee, M. G., Lee, J. C., et al. 2011, ApJ, 738, 58
Ishigaki, M., Kawamata, R., Ouchi, M., Oguri, M., & Shimasaku, K. 2017, ArXiv e-prints, arXiv:1702.04867
Ishigaki, M., Kawamata, R., Ouchi, M., et al. 2015, ApJ, 799, 12
Jaacks, J., Thompson, R., & Nagamine, K. 2013, ApJ, 766, 94
Jaskot, A. E., & Ravindranath, S. 2016, ApJ, 833, 136
Jauzac, M., Richard, J., Jullo, E., et al. 2015a, MNRAS, 452, 1437
Jauzac, M., Jullo, E., Eckert, D., et al. 2015b, MNRAS, 446, 4132
Johnson, B. D., Leja, J. L., Conroy, C., & Speagle, J. S. 2019, Prospector: Stellar population inference from spectra and SEDs
Johnson, K. E., Leroy, A. K., Indebetouw, R., et al. 2015, ApJ, 806, 35
Johnson, T. L., Sharon, K., Bayliss, M. B., et al. 2014, ApJ, 797, 48
Jones, T. A., Swinbank, A. M., Ellis, R. S., Richard, J., & Stark, D. P. 2010, MNRAS, 404, 1247
Jullo, E., & Kneib, J.-P. 2009, MNRAS, 395, 1319
Katz, H., & Ricotti, M. 2013, MNRAS, 432, 3250
Kauffmann, G., White, S. D. M., Heckman, T. M., et al. 2004, MNRAS, 353, 713

Kauffmann, G., Heckman, T. M., White, S. D. M., et al. 2003, MNRAS, 341, 54
Kawamata, R., Ishigaki, M., Shimasaku, K., Oguri, M., & Ouchi, M. 2015a, ApJ, 804, 103
—. 2015b, ApJ, 804, 103
Kawamata, R., Ishigaki, M., Shimasaku, K., et al. 2017, ArXiv e-prints, arXiv:1710.07301
Kawamata, R., Ishigaki, M., Shimasaku, K., et al. 2017, eprint arXiv:1710.07301
Kawamata, R., Ishigaki, M., Shimasaku, K., et al. 2018, ApJ, 855, 4
Kawamata, R., Oguri, M., Ishigaki, M., Shimasaku, K., & Ouchi, M. 2016, ApJ, 819, 114
Kennicutt, Robert C., J. 1998, ApJ, 498, 541
Khochfar, S., & Silk, J. 2006, ApJ, 648, L21
Kim, J.-h., Ma, X., Grudić, M. Y., et al. 2017, ArXiv e-prints, arXiv:1704.02988
Koekemoer, A. M., Faber, S. M., Ferguson, H. C., et al. 2011, ApJS, 197, 36
Kravtsov, A. V., & Gnedin, O. Y. 2005, ApJ, 623, 650
Kriek, M., & Conroy, C. 2013, ApJ, 775, L16
Kriek, M., van der Wel, A., van Dokkum, P. G., Franx, M., & Illingworth, G. D. 2008, ApJ, 682, 896
Kriek, M., van Dokkum, P. G., Labbé, I., et al. 2009, ApJ, 700, 221
Kriek, M., Shapley, A. E., Reddy, N. A., et al. 2015, ApJS, 218, 15
Kriek, M., Conroy, C., van Dokkum, P. G., et al. 2016, Nature, 540, 248
Kriek, M., van Dokkum, P. G., Labbé, I., et al. 2018, FAST: Fitting and Assessment of Synthetic Templates
Kroupa, P. 2001, MNRAS, 322, 231
Kroupa, P., Weidner, C., Pflamm-Altenburg, J., et al. 2013, The Stellar and Sub-Stellar Initial Mass Function of Simple and Composite Populations, ed. T. D. Oswalt & G. Gilmore, Vol. 5, 115
Krumholz, M. R. 2015, ArXiv e-prints, arXiv:1511.03457
Krumholz, M. R., McKee, C. F., & Bland -Hawthorn, J. 2019, ARA&A, 57, 227
Kuhlen, M., & Faucher-Giguère, C.-A. 2012, MNRAS, 423, 862
Kuhlen, M., Madau, P., & Silk, J. 2009, Science, 325, 970
Kurczynski, P., Gawiser, E., Acquaviva, V., et al. 2016, ApJ, 820, L1
Lada, C. J., & Lada, E. A. 2003, ARA&A, 41, 57
Lada, C. J., Lombardi, M., & Alves, J. F. 2010, ApJ, 724, 687
Laporte, N., Infante, L., Troncoso Iribarren, P., et al. 2016, ApJ, 820, 98
Larsen, S. S., Brodie, J. P., & Strader, J. 2012, A&A, 546, A53
Leaman, R., VandenBerg, D. A., & Mendel, J. T. 2013, MNRAS, 436, 122
Leaman, R., Venn, K. A., Brooks, A. M., et al. 2012, ApJ, 750, 33
Lee, J. C., Gil de Paz, A., Tremonti, C., et al. 2009, ApJ, 706, 599
Lee, S.-K., Ferguson, H. C., Somerville, R. S., Wiklind, T., & Giavalisco, M. 2010, ApJ, 725, 1644
Leja, J., Carnall, A. C., Johnson, B. D., Conroy, C., & Speagle, J. S. 2019, ApJ, 876, 3
Leja, J., Johnson, B. D., Conroy, C., van Dokkum, P. G., & Byler, N. 2017, ApJ, 837, 170
Leja, J., van Dokkum, P., & Franx, M. 2013, ApJ, 766, 33
Leroy, A. K., Bolatto, A. D., Ostriker, E. C., et al. 2018, ApJ, 869, 126
Li, H., & Gnedin, O. Y. 2014, ApJ, 796, 10
Lilly, S. J., & Carollo, C. M. 2016, ApJ, 833, 1

Lindegren, L., Lammers, U., Bastian, U., et al. 2016a, A&A, 595, A4
—. 2016b, A&A, 595, A4
Livermore, R. C., Finkelstein, S. L., & Lotz, J. M. 2017, ApJ, 835, 113
Livermore, R. C., Jones, T. A., Richard, J., et al. 2015, MNRAS, 450, 1812
Lotz, J. M., Jonsson, P., Cox, T. J., et al. 2011, ApJ, 742, 103
Lotz, J. M., Primack, J., & Madau, P. 2004, AJ, 128, 163
Lotz, J. M., Davis, M., Faber, S. M., et al. 2008, ApJ, 672, 177
Lotz, J. M., Koekemoer, A., Coe, D., et al. 2017, ApJ, 837, 97
Ma, X., Hopkins, P. F., Boylan-Kolchin, M., et al. 2017, ArXiv e-prints, arXiv:1710.00008
Madau, P., & Dickinson, M. 2014, ARA&A, 52, 415
Madau, P., Kuhlen, M., Diemand, J., et al. 2008, ApJ, 689, L41
Madau, P., Shen, S., & Governato, F. 2014, ApJ, 789, L17
Man, A. W. S., Zirm, A. W., & Toft, S. 2016, ApJ, 830, 89
Mandelker, N., Dekel, A., Ceverino, D., et al. 2017, MNRAS, 464, 635
—. 2014, MNRAS, 443, 3675
Maraston, C., Pforr, J., Renzini, A., et al. 2010, MNRAS, 407, 830
Marconi, A., & Hunt, L. K. 2003, ApJ, 589, L21
Maseda, M. V., van der Wel, A., da Cunha, E., et al. 2013, ApJ, 778, L22
Maseda, M. V., van der Wel, A., Rix, H.-W., et al. 2014, ApJ, 791, 17
Maseda, M. V., Bacon, R., Franx, M., et al. 2018, ApJ, 865, L1
McConnachie, A. W. 2012, AJ, 144, 4
McConnachie, A. W., Irwin, M. J., Ibata, R. A., et al. 2009, Nature, 461, 66
McKee, C. F., & Ostriker, E. C. 2007, ARA&A, 45, 565
Mehta, V., Scarlata, C., Rafelski, M., et al. 2017, ApJ, 838, 29
Menci, N., Merle, A., Totzauer, M., et al. 2017, ApJ, 836, 61
Mendel, J. T., Saglia, R. P., Bender, R., et al. 2015, ApJ, 804, L4
Merritt, A., van Dokkum, P., Abraham, R., & Zhang, J. 2016, ApJ, 830, 62
Meurer, G. R., Wong, O. I., Kim, J. H., et al. 2009, ApJ, 695, 765
Miller, S. H., Sullivan, M., & Ellis, R. S. 2013, ApJ, 762, L11
Momcheva, I. G., Brammer, G. B., van Dokkum, P. G., et al. 2016, ApJS, 225, 27
Monachesi, A., Bell, E. F., Radburn-Smith, D. J., et al. 2016, MNRAS, 457, 1419
Mosleh, M., Tacchella, S., Renzini, A., et al. 2017, ApJ, 837, 2
Mouhcine, M., Ferguson, H. C., Rich, R. M., Brown, T. M., & Smith, T. E. 2005, ApJ, 633, 810
Muratov, A. L., & Gnedin, O. Y. 2010, ApJ, 718, 1266
Muzzin, A., Marchesini, D., Stefanon, M., et al. 2013, ApJ, 777, 18
Navarro, J. F., Ludlow, A., Springel, V., et al. 2010, MNRAS, 402, 21
Nevin, R., Blecha, L., Comerford, J., & Greene, J. 2019, ApJ, 872, 76
Oñorbe, J., Boylan-Kolchin, M., Bullock, J. S., et al. 2015a, MNRAS, 454, 2092
—. 2015b, MNRAS, 454, 2092
Ochsendorf, B. B., Zinnecker, H., Nayak, O., et al. 2017, Nature Astronomy, 1, 784
Oesch, P. A., Bouwens, R. J., Illingworth, G. D., et al. 2015, ApJ, 808, 104
Oguri, M. 2010, PASJ, 62, 1017

Oklopčić, A., Hopkins, P. F., Feldmann, R., et al. 2017, MNRAS, 465, 952
O'Malley, E. M., Gilligan, C., & Chaboyer, B. 2017, ApJ, 838, 162
Onodera, M., Renzini, A., Carollo, M., et al. 2012, ApJ, 755, 26
O'Shea, B. W., Wise, J. H., Xu, H., & Norman, M. L. 2015, ApJ, 807, L12
Ostriker, J. P., Spitzer, Jr., L., & Chevalier, R. A. 1972, ApJ, 176, L51
Pancino, E., Bellazzini, M., Giuffrida, G., & Marinoni, S. 2017, MNRAS, 467, 412
Peebles, P. J. E. 1980, The large-scale structure of the universe
Peng, C. Y., Ho, L. C., Impey, C. D., & Rix, H.-W. 2002, AJ, 124, 266
Peng, E. W., Côté, P., Jordán, A., et al. 2006, ApJ, 639, 838
Pflamm-Altenburg, J., Weidner, C., & Kroupa, P. 2007, ApJ, 671, 1550
—. 2009, MNRAS, 395, 394
Piotto, G., Milone, A. P., Anderson, J., et al. 2012, ApJ, 760, 39
Planck Collaboration, Ade, P. A. R., Aghanim, N., et al. 2016, A&A, 594, A13
Poggianti, B. M., Aragón-Salamanca, A., Zaritsky, D., et al. 2009, ApJ, 693, 112
Power, C., Wynn, G. A., Robotham, A. S. G., Lewis, G. F., & Wilkinson, M. I. 2014, ArXiv e-prints, arXiv:1406.7097
Price, S. H., Kriek, M., Shapley, A. E., et al. 2015, Astrophysical Journal, 819
Reddy, N., Dickinson, M., Elbaz, D., et al. 2012a, ApJ, 744, 154
Reddy, N. A., Pettini, M., Steidel, C. C., et al. 2012b, ApJ, 754, 25
Reddy, N. A., Kriek, M., Shapley, A. E., et al. 2015, ApJ, 806, 259
Renzini, A. 2017, MNRAS, 469, L63
Renzini, A., D'Antona, F., Cassisi, S., et al. 2015, MNRAS, 454, 4197
Ribeiro, B., Le Fèvre, O., Cassata, P., et al. 2017, A&A, 608, A16
Richard, J., Jauzac, M., Limousin, M., et al. 2014, MNRAS, 444, 268
Ricotti, M. 2002, MNRAS, 336, L33
Ricotti, M., Gnedin, N. Y., & Shull, J. M. 2008, ApJ, 685, 21
Robertson, B. E., Ellis, R. S., Furlanetto, S. R., & Dunlop, J. S. 2015, ApJ, 802, L19
Robertson, B. E., Furlanetto, S. R., Schneider, E., et al. 2013, ApJ, 768, 71
Rodighiero, G., Daddi, E., Baronchelli, I., et al. 2011, ApJ, 739, L40
Rujopakarn, W., Daddi, E., Rieke, G. H., et al. 2019, arXiv e-prints, arXiv:1904.04507
Sanders, R. L., Shapley, A. E., Kriek, M., et al. 2016, ApJ, 816, 23
Sanders, R. L., Shapley, A. E., Reddy, N. A., et al. 2020, MNRAS, 491, 1427
Schaerer, D., & Charbonnel, C. 2011, MNRAS, 413, 2297
Schaye, J., Crain, R. A., Bower, R. G., et al. 2015, MNRAS, 446, 521
Schultz, C., Oñorbe, J., Abazajian, K. N., & Bullock, J. S. 2014, MNRAS, 442, 1597
Searle, L., & Zinn, R. 1978, ApJ, 225, 357
Sheth, R. K., Mo, H. J., & Tormen, G. 2001, MNRAS, 323, 1
Shibuya, T., Ouchi, M., & Harikane, Y. 2015, ApJS, 219, 15
Shibuya, T., Ouchi, M., Kubo, M., & Harikane, Y. 2016, ApJ, 821, 72
Shipley, H. V., Lange-Vagle, D., Marchesini, D., et al. 2018, ApJS, 235, 14
Shivaei, I., Reddy, N. A., Shapley, A. E., et al. 2015, ApJ, 815, 98
Shivaei, I., Reddy, N., Shapley, A., et al. 2017, Astrophysical Journal, 837

Silverman, J. D., Daddi, E., Rodighiero, G., et al. 2015, ApJ, 812, L23
Skelton, R. E., Whitaker, K. E., Momcheva, I. G., et al. 2014, ApJS, 214, 24
Smit, R., Bouwens, R. J., Labbé, I., et al. 2016, ApJ, 833, 254
Soderblom, D. R. 2010, ARA&A, 48, 581
Sparre, M., Hayward, C. C., Feldmann, R., et al. 2017, MNRAS, 466, 88
Speagle, J. S. 2019, arXiv e-prints, arXiv:1904.02180
Speagle, J. S., Steinhardt, C. L., Capak, P. L., & Silverman, J. D. 2014, ApJS, 214, 15
Spitler, L. R., Straatman, C. M. S., Labbé, I., et al. 2014, ApJ, 787, L36
Springel, V., White, S. D. M., Jenkins, A., et al. 2005, Nature, 435, 629
Stark, D. P. 2016a, ARA&A, 54, 761
—. 2016b, ARA&A, 54, 761
Stark, D. P., Swinbank, A. M., Ellis, R. S., et al. 2008, Nature, 455, 775
Stark, D. P., Richard, J., Siana, B., et al. 2014, MNRAS, 445, 3200
Stinson, G. S., Dalcanton, J. J., Quinn, T., Kaufmann, T., & Wadsley, J. 2007, ApJ, 667, 170
Stott, J. P., Swinbank, A. M., Johnson, H. L., et al. 2016, MNRAS, 457, 1888
Suess, K. A., Kriek, M., Price, S. H., & Barro, G. 2019, ApJ, 877, 103
Swinbank, A. M., Dye, S., Nightingale, J. W., et al. 2015, ApJ, 806, L17
Tacchella, S., Dekel, A., Carollo, C. M., et al. 2016, MNRAS, 458, 242
Tacchella, S., Diemer, B., Hernquist, L., et al. 2019, MNRAS, 487, 5416
Tacconi, L. J., Genzel, R., Neri, R., et al. 2010, Nature, 463, 781
Tamburello, V., Mayer, L., Shen, S., & Wadsley, J. 2015, MNRAS, 453, 2490
Tamburello, V., Rahmati, A., Mayer, L., et al. 2017, MNRAS, 468, 4792
Tanner, J. D., Basu, S., & Demarque, P. 2014, ApJ, 785, L13
Tayar, J., Somers, G., Pinsonneault, M. H., et al. 2017, ApJ, 840, 17
Thompson, R., Davé, R., Huang, S., & Katz, N. 2015, arXiv e-prints, arXiv:1508.01851
Tomczak, A. R., Quadri, R. F., Tran, K.-V. H., et al. 2014, ApJ, 783, 85
Tonini, C. 2013, ApJ, 762, 39
Tremaine, S., Gebhardt, K., Bender, R., et al. 2002, ApJ, 574, 740
Treu, T., Schmidt, K. B., Brammer, G. B., et al. 2015, ApJ, 812, 114
Tully, R. B., & Fisher, J. R. 1977, A&A, 500, 105
van de Sande, J., Kriek, M., Franx, M., et al. 2013, ApJ, 771, 85
van der Wel, A., Bell, E. F., Häussler, B., et al. 2012, ApJS, 203, 24
van der Wel, A., Franx, M., van Dokkum, P. G., et al. 2014, ApJ, 788, 28
van Dokkum, P. G., Brammer, G., Fumagalli, M., et al. 2011, ApJ, 743, L15
van Dokkum, P. G., Leja, J., Nelson, E. J., et al. 2013, ApJ, 771, L35
van Dokkum, P. G., Nelson, E. J., Franx, M., et al. 2015, ApJ, 813, 23
VandenBerg, D. A., Brogaard, K., Leaman, R., & Casagrande, L. 2013, ApJ, 775, 134
Vanzella, E., De Barros, S., Cupani, G., et al. 2016, ApJ, 821
Vanzella, E., Calura, F., Meneghetti, M., et al. 2017, MNRAS, 467, 4304
—. 2019, MNRAS, 483, 3618
Villanova, S., Geisler, D., Piotto, G., & Gratton, R. G. 2012, ApJ, 748, 62
Vogelsberger, M., Genel, S., Springel, V., et al. 2014, MNRAS, 444, 1518

Walker, M. G., & Peñarrubia, J. 2011, ApJ, 742, 20
Weisz, D. R., & Boylan-Kolchin, M. 2017, MNRAS, 469, L83
Weisz, D. R., Dolphin, A. E., Skillman, E. D., et al. 2013, MNRAS, 431, 364
Weisz, D. R., Johnson, B. D., & Conroy, C. 2014, ApJ, 794, L3
Weisz, D. R., Johnson, B. D., Johnson, L. C., et al. 2012, ApJ, 744, 44
West, M. J., Côté, P., Marzke, R. O., & Jordán, A. 2004, Nature, 427, 31
Wetzel, A. R., Hopkins, P. F., Kim, J.-h., et al. 2016, ApJ, 827, L23
Whitaker, K. E., Kriek, M., van Dokkum, P. G., et al. 2012, ApJ, 745, 179
Whitaker, K. E., Labbé, I., van Dokkum, P. G., et al. 2011, ApJ, 735, 86
Whitaker, K. E., van Dokkum, P. G., Brammer, G., et al. 2013, ApJ, 770, L39
Wild, V., Almaini, O., Dunlop, J., et al. 2016, MNRAS, 463, 832
Williams, R. J., Quadri, R. F., Franx, M., van Dokkum, P., & Labbé, I. 2009, ApJ, 691, 1879
Wisnioski, E., Förster Schreiber, N. M., Wuyts, S., et al. 2015, ApJ, 799, 209
Wong, K. C., Ammons, S. M., Keeton, C. R., & Zabludoff, A. I. 2012, ApJ, 752, 104
Worthey, G., & Ottaviani, D. L. 1997, ApJS, 111, 377
Wu, P.-F., van der Wel, A., Gallazzi, A., et al. 2018, ApJ, 855, 85
Wuyts, E., Wisnioski, E., Fossati, M., et al. 2016, ApJ, 827, 74
Wuyts, S., Franx, M., Cox, T. J., et al. 2009, ApJ, 696, 348
Wuyts, S., Förster Schreiber, N. M., Lutz, D., et al. 2011, ApJ, 738, 106
Wuyts, S., Förster Schreiber, N. M., Genzel, R., et al. 2012, ApJ, 753, 114
Yano, M., Kriek, M., van der Wel, A., & Whitaker, K. E. 2016, ApJ, 817, L21
Zanella, A., Daddi, E., Le Floc'h, E., et al. 2015, Nature, 521, 54
Zanella, A., Le Floc'h, E., Harrison, C. M., et al. 2019, MNRAS, 489, 2792
Zaritsky, D., Colucci, J. E., Pessev, P. M., Bernstein, R. A., & Chandar, R. 2012, ApJ, 761, 93
Zick, T. O., Weisz, D. R., & Boylan-Kolchin, M. 2018, MNRAS, 477, 480
Zick, T. O., Weisz, D. R., Ribeiro, B., et al. 2020, MNRAS, 493, 5653
Zinnecker, H., Keable, C. J., Dunlop, J. S., Cannon, R. D., & Griffiths, W. K. 1988, Symposium - International Astronomical Union, 126, 603
Zolotov, A., Dekel, A., Mandelker, N., et al. 2015, MNRAS, 450, 2327